WASHINGTON UNIVERSITY

School of Engineering and Applied Science
Department of Energy, Environmental and Chemical Engineering

Dissertation Examination Committee:
Milorad Dudukovic, Chair
Muthanna Al-Dahhan
Da-Ren Chen
Mark Conradi
John Gleaves
Palghat Ramachandran
Hugh Stitt

HYDRODYNAMICS OF TRICKLE BED REACTORS: MEASUREMENTS AND MODELING

by

Zeljko Kuzeljevic

A dissertation presented to the
Graduate School of Arts and Sciences
of Washington University in
partial fulfillment of the
requirements for the degree
of Doctor of Philosophy

May 2010

Saint Louis, Missouri

ABSTRACT OF THE DISSERTATION

Hydrodynamics of Trickle Bed Reactors: Measurements and Modeling

by

Zeljko Kuzeljevic

Doctor of Philosophy in Chemical Engineering

Washington University in St. Louis, 2010

Professor Milorad Dudukovic, Chairman

In this study we develop the computational and experimental tools to assist us in performance evaluation of trickle bed reactors (TBRs). The study focuses on experimental characterization of the flow distribution, and development of computational fluid dynamics (CFD) model of trickle flow.

The experimental study has been performed to examine the quality of liquid phase distribution in a high pressure system. The results were provided in terms of distribution of the effluent liquid fluxes and cross-sectional liquid holdups. Their individual trends, but also their relation with respect to operating conditions was examined.

Characterization of bed porosity distribution has been performed and used as the input to the computational model.

The experimental study of the dependence of the extent of hysteresis on operating parameters in a high pressure TBR was performed. The extent of hysteresis was found uniquely determined by the pressure drop in the Levec prewetting mode. This fact and developed CFD model were then used to deduce conditions leading to hysteresis free operation.

Three-dimensional Eulerian CFD model is developed. Phase interaction closures are based on the film flow model, principles of statistical hydrodynamics and relative permeability concept. Model has been assessed against experimental data for liquid holdup, wetting efficiency and pressure drop hysteresis. Hydrodynamic Eulerian CFD model is then used together with species balance to examine the TBR performance for gas and liquid reactant limited systems. For each case a closed form approach of coupling bed and particle scale solution within CFD framework was presented.

Table of Contents

List of Tables

List of Figures

Nomenclature

a,b	parameters of Mueller, 1991 correlation, -
D_c	column diameter, m
$D_{i,m}$	molecular diffusivity of species i, m^2/s
d_p	packing particle diameter, m
E_1	parameter of Ergun equation, -
E_2	parameter of Ergun equation, -
$F_{f,\alpha}$	F-function parameter for phase α, -
f_H	hysteresis factor, -
$FLUX$	average liquid flux, kg/m^2s
$FLUX_i$	liquid flux in compartment i (i = 1,…15), kg/m^2s
F_α	drag exerted on phase α per unit volume of bed, N/m^3
g	gravity acceleration, m/s^2
H	curvature, m
I	Modified Bessel function
J_0	zeroth order Bessel function
k_{LS}	liquid-solid mass transfer coefficient, m/s
k_α	permeability of phase α, m^2
K_α	relative (viscous) permeability of phase α, -
$K_{\alpha,i}$	relative (inertial) permeability of phase α, -

$K_{\beta\alpha}$	momentum exchange coefficient, kg/m^{3}s
L	liquid phase mass flux, kg/m^{2}s
M	molecular weight, kg/kmol
M_f	maldistribution factor, equation (3-1)
N	number of compartments in a collecting tray
P	pressure, Pa
P_c	capillary pressure, Pa
$Pc^{dynamic}$	dynamic capillary pressure, Pa
r	radial coordinate, m
r^*	dimensionless radial coordinate (=r/d_p)
R_{col}	column radius, m
$R_{i,r}$	disappearance of species i in reaction r, $kg_i/m^3{}_\alpha s$
r_i^{begin}	radial coordinate designating the beginning of section *i*, m
r_i^{end}	radial coordinate designating the end of section *i*, m
S_G	gas phase saturation, m^{3}gas/m^{3}voids
S_L	liquid phase saturation, m^{3}gas/m^{3}voids
t	time, s
T	temperature, K
u	dimensionless intraparticle concentration
U_α	α phase superficial velocity, m/s
u_α	interstitial (physical) velocity of phase α, m/s

u_α' fluctuating component of velocity for phase α, m/s

V molar volume, cm^3/mol

w_{slit} parameter of slit model

$Y_{i,\alpha}$ mass fraction of species i, kg_i/kg_α

z axial coordinate, m *or* scaling factor used in AM algorithm, -

$\Delta P/L$ pressure drop gradient, kPa/m

d measured number of photons (at detector)

l length, cm

J_j set of projections to which pixel j contributes

n iteration number

$\boldsymbol{q}$ photon transmission model vector of AM algorithm

$\boldsymbol{F_\mu}$ Fisher information matrix

T transpose operation

p probability density function of measured (incomplete) data set

$\boldsymbol{Y}$ random vector of measured (incomplete) data

f probability density function of complete data set

$E\{.\}$ expectation operator

i projection index

j pixel index

I_i set of pixels contributing to projection i

S	score
C_{μ}	Cramer-Rao bound
tr	trace operator
$Error$	mean absolute percentage error

Greek letters:

$<\varepsilon_{B,i}>$	average porosity in section *i* of the computational grid, -
β_{dyn}	dynamic liquid holdup, m^3/m^3_{bed}
δ_L	reduced liquid phase saturation, - $(=\frac{\varepsilon_L - \varepsilon_L^0}{\varepsilon_B - \varepsilon_L^0})$
δ_{slit}	parameter of slit model
ε_B	bed porosity, m^3voids/m^3bed
$\varepsilon_L{}^0$	static liquid holdup, -
ε_α	α phase total holdup (volume fraction), m^3/m^3bed
η	catalyst effectiveness factor, -
η_{CE}	catalyst wetting efficiency,-
η_α	passability of phase α, m^2
θ	contact angle, rad *or* Wijffels, 1974 model parameter
θ_{slit}	parameter of slit model, slit inclination, rad
κ	dimensionless particle scale azimuthal coordinate
μ_α	α phase viscosity, Pa.s

ξ	dimensionless particle scale radial coordinate
ρ_α	α phase density, kg/m^3
σ	surface tension, N/m
τ_1^{Pc}	parameter of Mirzaei and Das, 2007 capillary model
τ_2^{Pc}	parameter of Mirzaei and Das, 2007 capillary model
τ_{LG}	shear stress exerted by liquid on gas phase, Pa
τ_w	shear stress exerted by wall on liquid phase, Pa
τ_α	stress tensor of phase α, Pa
$\tau_\alpha^{(t)}$	Reynolds stress tensor of phase α, Pa
χ	parameter of relative permeability model, -
ψ	dimensionless pressure gradient
μ	attenuation coefficient, cm^{-1}
μ_i^{theor}	theoretical value of attenuation coefficient, cm^{-1}
ξ	pixel size in the reconstructed image, mm
δ	total number of scan lines considered in the process of reconstruction, % of full scan (full scan has 17,500 scan lines)
τ	number of projections per view, -
$\boldsymbol{\mu}$	set of parameters to be estimated via EM or AM algorithm
λ	mean number of photons emitted by gamma-ray source

Dimensionless numbers:

Bo Bond number $(= \frac{d_p^2(\rho_L - \rho_G)g}{\sigma})$

Ca Capillary number $(= \frac{\mu_L U_L}{\sigma})$

Ga Galileo number $(= \frac{d_p{}^3 \rho^2 g \varepsilon_B{}^3}{\mu^2 (1-\varepsilon_B)^3})$

Re Reynolds number $(= \frac{\rho d_p U}{\mu})$

Re_{max} Local Reynolds number at which local flooding occurs, eq. (5-13)

Re_{min} Minimum Reynolds number assuring catalyst wetting, eq. (5-11)

Sc Schmidt number $(= \frac{\mu}{\rho D_{i,m}})$

Subscripts:

A solute

B solvent

d dry pellet

G gas

hw half-wetted pellet

L liquid

S solid

w fully-wetted pellet

Abbreviations:

AM alternating-minimization

BC boundary condition

CFD computational fluid dynamics

CT computed tomography

ECT electrical capacitance tomography

EM expectation-maximization

HP TBR high pressure trickle bed reactor

IC initial condition

LHSV liquid hourly space velocity

MRI magnetic resonance imaging

NMR nuclear magnetic resonance

RTD residence time distribution

TBR trickle bed reactor

VOF volume of fluid

Chapter 1
Introduction

Trickle Bed Reactors (TBRs) are packed beds in which gas and liquid reactants flow co-currently down. These reactors were fist used in the mid-nineteen century ("trickling filters") in water treatment. Today, they are used in petroleum and refinery processes such as hydrodesulphurization and hydrogenation, but also find application in oxidation of organics in wastewater effluents, abatement of volatile organic compounds in air pollution control, and enzymatic reactions (Dudukovic et al., 1999).

These reactors are very flexible with respect to varying throughput demands and exhibit a flow pattern that is close to plug flow. The ratio of liquid to solid is small, which is advantageous in preventing homogeneous side reactions. Nevertheless, trickle beds can suffer serious drawbacks, such as liquid mal-distribution, which reduces the expected conversion and can lead to hot spots (Sie and Krishna, 1998). The solution to these problems depends on the further improvement of our understanding of the phenomena that affect TBR hydrodynamics.

1.1 Research Motivation

Although TBRs find many applications and have been subject to extensive investigation, the current understanding of these reactors is still not satisfactory. The

basic problem lies in the difficulties in measuring and describing both the very complex gas-liquid, gas-solid, and liquid-solid phase interactions and the geometry that arises due to the size, shape and method of packing of the particles that constitute the bed. Naturally, in the effort to provide fundamentally based quantitative information on the hydrodynamics in these beds, simplifications in the description and modeling of both geometry and phase interactions are assumed. Many of the proposed phenomenological models (Saez and Carbonell, 1985; Levec et al., 1985; Holub et al., 1992a; Al-Dahhan et al., 1998; Attou et al., 1999; Iliuta and Larachi, 2005; see also the comparative analysis of models given by Carbonell, 2000) have the potential to predict global hydrodynamic parameters, such as overall liquid holdup and pressure drop, based on idealization of the pore space. However, this idealization of the pore space is what prevents the proper prediction of some experimentally observed phenomena (liquid maldistribution or hot spot formation) which are due to inhomogeneity of the pore space. Currently, Eulerian computational fluid dynamics (CFD) is employed in an attempt to describe and capture these phenomena. The underlying equations, obtained by volume averaging of momentum and mass conservation equations, treat the phases as interpenetrating continua and have a very attractive form which does not require detailed geometry of the system as an input (Ishii, 1975). However, the system of equations needs to be closed with descriptions of interphase momentum exchanges and local force field effects, i.e., the closure equations. Usually, these are grouped into phase interaction closures (i.e., gas-liquid, gas-solid and liquid-solid interactions) and capillary pressure closure. The first group gives an estimate of momentum transfer from/to each phase due to drag exerted at

the interfacial areas. The second gives the pressure difference between the non-wetting (i.e., gas) and wetting (i.e., liquid) phase, which arises due to the non-zero value of curvature of the interfacial area between the two phases (Young, 1805, and Dullien, 1992). Since the basic set of averaged equations is, in principle, applicable to any multiphase system, it is evident that a physical picture of the system introduced through closures is crucial for proper modeling. Also, it is recognized that in multiphase systems events observed on the meso-scale (e.g., a cell size of tens of packing particles) are a result of instabilities present in the micro-scale (i.e., the scale of one packing particle). Thus, the success of CFD modeling depends on the availability of mechanistic models that capture the physical essence of the system and model micro-scale phenomena in the meso-scale framework, i.e., without the need to introduce detailed geometry into the computational domain.

At this moment, Eulerian CFD simulation (Jiang et al., 2002a; Gunjal et al., 2005a; Boyer et al., 2005; Gunjal and Ranade, 2007, and Atta et al., 2007a) introduces closures that are based on the phenomenological models mentioned above and on the spatial dependence of porosity. These models, however, can be improved for the purpose of CFD modeling by relating the model more closely to the actual physical picture of the bed voidage spaces and the flow in it. For example, currently used closures assume film flow and complete wetting of the external catalyst area. Experimental studies (Crine et al., 1980; Sicardi et al., 1981; Zimmerman and Ng, 1986; Lutran et al., 1991; Ravindra et al., 1997; Marcandelli et al., 2000; Mantle et al., 2001, and van Houwelingen et al., 2006)

show that this type of flow is not always present on the meso and micro scale, especially at conditions of lower liquid velocity. Accounting for the other flow patterns, such as filament flow, provides potential for better predictions.

In studies performed by Ellman et al., 1988; Larachi et al., 1991; Al-Dahhan and Dudukovic, 1994, and Nemec and Levec, 2005, it was shown that increased operating pressure alters the wetting efficiency (fraction of external catalyst area covered by actively flowing liquid) and flow distribution. These quantities however may not be uniquely determined at a given set of conditions due to a hysteresis phenomenon - the observed dependence of the operating parameters (such as pressure drop and liquid holdup) on the flow history. Hysteresis was a subject of thorough experimental investigation (Kan and Greenfield, 1978; Christensen et al., 1986; Levec et al., 1988; Loudon et al., 2006, and Maiti et al., 2006) at low (atmospheric) pressure operation. However, at this moment, there is no systematic study of the effect of elevated pressure on the extent of hysteresis. It is expected that change in phase distribution and wetting efficiency due to elevated pressure will have impact on the extent of hysteresis. Also, a method for prediction of the extent of hysteresis is needed. Such method could be applied to the actual industrial reactors to determine the envelope of operating conditions within which TBR performance is affected by the start-up mode used.

1.2 Research Objectives

The overall objectives of this study are three-fold: (i) to review and present the current state-of-the-art in TBR's theoretical and experimental investigation, (ii) to examine experimentally the flow distribution and related phenomena (hysteresis), and (iii) to develop the reactive flow CFD model applicable to TBR. In order to achieve these overall goals, the following steps have been taken:

1. Experimental work - the design and assembly of a high pressure trickle bed reactor (HP TBR) to perform an experimental study of the hydrodynamics in order to determine:
    - Two phase flow pressure drop and liquid holdup
    - Voidage and the gas and liquid cross-sectional distributions (using gamma-ray computed tomography (CT)) along the bed height
    - Liquid effluent fluxes
    - The effect of operating conditions on the extent of hysteresis in pressure drop

Thus, the experimental part of the study investigates the influence of the operating conditions on the resulting flow distribution and basic hydrodynamics parameters.

2. Theoretical work consists of setting up a three-dimensional Eulerian CFD model for prediction of flow distribution, and overall holdup and pressure drop assessment. Specific goals focused on:

- Devising the methodology for implementation of experimental porosity distribution into the 3D CFD grid
- Assessing model prediction capabilities
- Examining the extensions of closures by relaxing the assumption of film flow currently used in the model
- Use of hydrodynamic Eulerian CFD model together with species balance to examine the TBR performance for gas and liquid limited systems and develop a closed form approach for coupling bed and particle scale solutions within CFD framework.

1.3 Thesis outline

The thesis has been structured in the following manner. Chapter 2 provides a background on TBR literature. Experimental studies of flow distribution and hysteresis are given in Chapter 3 and Chapter 4, respectively. CFD modeling and results are described in Chapter 5. Thesis accomplishments and recommendations for the future work are given in Chapter 6.

Chapter 2
Background

2.1 Introduction

As already stated, trickle bed reactors (TBRs) are multiphase reactors in which gas and liquid phases are introduced at the top of the column and flow co-currently down a packed bed of catalyst. They are used in petroleum and refinery processes such as hydrodesulphurization and hydrogenation, but also find application in oxidation of organics in wastewater effluents, volatile organic compound abatement in air pollution control, and enzymatic reactions. The use of TBRs offers many advantages: they operate at conditions that are close to plug flow, have high catalyst to liquid ratio which is useful in abating the homogenous side reactions, high throughput range, and there is no danger of flooding. On the other hand, TBRs also have serious drawbacks. They are prone to liquid mal-distribution and incomplete catalyst wetting. This reduces the extent of catalyst utilization and, for the case of highly exothermic reactions, can lead to hot spots and reactor runaway (Jaffe, 1976, and Hanika, 1999). Also, to reduce the pressure drop, catalyst particle diameters are usually in the range of couple of millimeters. Thus, in TBRs intraparticle diffusion effects can play a significant role (Sie and Krishna, 1998).

Due to the frequent use of trickle beds they have been subject to extensive investigation. Various aspects of TBR investigation have been reviewed in Herskowitz and Smith,

1983; Gianetto and Silveston, 1986; Ramachandran et al., 1987; Zhukova et al., 1990; Gianetto and Specchia, 1992; Sundaresan, 1994; Saroha and Nigam, 1996; Al-Dahhan et al., 1997; Sie and Krishna, 1998; Dudukovic et al., 1999; Iliuta et al., 1999; Carbonell, 2000; Dudukovic et al., 2002; Kundu et al., 2003a; Maiti et al., 2004; van Herk et al., 2005; Maiti et al., 2006, and Maiti and Nigam, 2007.

TBRs' prominent role in oil processing and increasingly stringent regulations on the sulfur content of petroleum products lead to a continuous need for reassessment of their performance and further development. Latest examples from industrial practice of oil refining include the improvement of catalyst used in hydrodesulphurization (BP, 2004). Ways to use the established practices and modify installations of TBRs for the hydrogenation of vegetable oil in the production of renewable biodiesel are being examined (ConocoPhillips, 2008). There is ongoing research to achieve process intensification in TBRs by using non-conventional modes of operation. Unsteady state operation has been suggested and analyzed (see for example Khadilkar et al., 2005, and Nigam and Larachi, 2005 and references therein), and the use of magnetic field gradient as an additional body force to control the value of liquid holdup in the reactor (Iliuta and Larachi, 2003).

Figure 2.1 schematically illustrates the key phenomena affecting TBR performance and lists the major research areas. As shown, the field of research of TBRs is broad. In this

text we will start with the brief description of flow in TBRs and then focus on the current status of describing the flow distribution. Then we will review the developments in phenomenological and CFD modeling of the two phase flows in these systems.

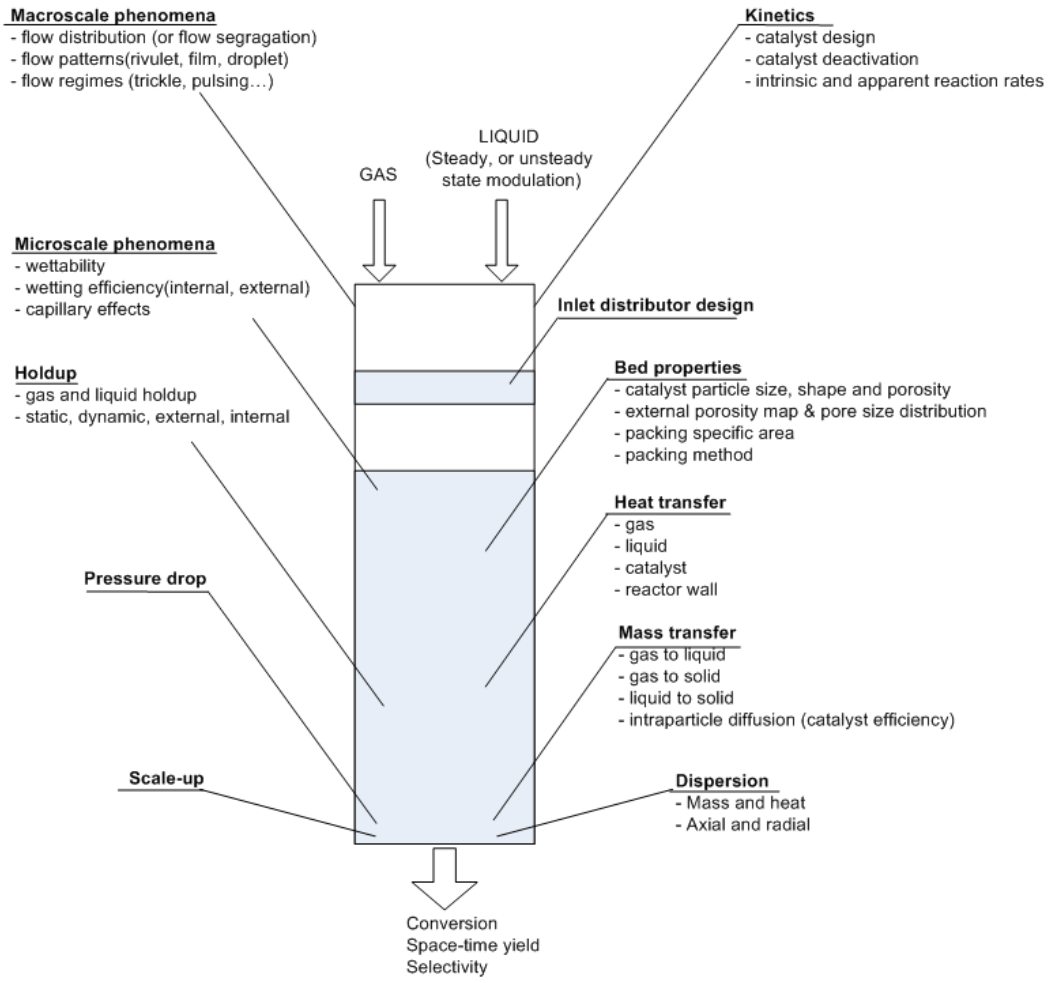

Figure 2.1 Overview of the research areas and factors affecting TBR performance (Adapted from Nigam and Larachi, 2005)

2.2 Description of two phase flow

Once introduced into the bed at the top of the packing, the two flowing phases compete for the available interstitial space. The geometry of the interstitial space is determined by the shape and size of the particles in the bed and by the packing methodology. For different packing procedures and the way they influence the reproducibility of the hydrodynamic parameters see Al-Dahhan et al., 1995. The geometrical description of the (external) pore space is difficult since the analytical expression characterizing the surface that bounds the void space is not easily attainable. Instead, the meso or macro scale parameters are employed, such as porosity (the volume fraction of voids in the bed), specific external area of the particles, tortuosity (the ratio of the average length of interstitial flow paths over the height of the reactor), and pore size distribution. As discussed below, an ongoing effort continues to provide the experimental data and theoretical (or empirical) expressions for these quantities. Further information is also available in Bear, 1972, and Dullien, 1992.

The flow of the two phases in the void space and the flow of liquid across the surface of the particles in the bed are governed by the gravitational, inertial, viscous and capillary forces. For the conditions typically present in TBRs all of these forces are comparable in magnitude and all of them need to be included in the theoretical analysis (Table 2.1).

Table 2.1 Range of force ratios in two phase flow (adapted from Melli et al., 1990)

Solid support	Characteristic length, m	Force ratios		
		inertial/viscous, Re*	viscous/capillary, Ca	capillary/gravitational, 1/Bo
Fine porous media (oil recovery)	$10^{-7} – 10^{-4}$	$10^{-9} – 10^{-2}$	$10^{-7} – 10^{-3}$	$10^{2} – 10^{9}$
Coarse porous media (packed beds)	$10^{-3} – 10^{-2}$	$10^{-2} – 10^{-3}$	$10^{-1} – 10$	$10^{-1} – 10$
Piping (nuclear technology)	10^{-2}	$10 – 10^{5}$	$10 – 10^{2}$	$10^{-3} – 10^{1}$

* All dimensionless numbers are defined in the notation

Depending on the operating conditions, with gas and liquid flow rates being the most influential, the overall hydrodynamic behavior of a TBR can be placed within the boundaries of one of the four *flow regimes*, namely trickle, pulsing, spray and bubbly flow regime (Charpentier and Favier, 1975). In this study we are interested in the trickle flow regime which is characteristic for the lower gas and liquid velocities and hence also termed low interaction regime. In this regime, both gas and liquid phases are continuous. In contrast, for example, in the spray flow regime liquid phase is dispersed in form of droplets and bounded by the continuous gas phase. The conditions that lead to transition between flow regimes have been discussed in the studies of Charpentier and Favier, 1975; Talmor, 1977; Fukushima and Kusaka, 1977; Grosser et al., 1988; Wammes et al., 1991; Holub et al., 1992a; Attou and Ferschneider, 1999; Iliuta et al., 2005, and Anadon et al., 2005. No single agreed upon criterion that is based on fundamentals is available for any of the flow regime transitions. Flow regime maps remain to a great extent empirical.

The meso (couple of particles) scale of the trickle flow is characterized by the occurrence of the various *flow patterns*. Flow pattern, to a certain extent, indicates the quality of flow distribution or the undesirable occurrence of flow segregation. Rivulet, filament and film flow patterns are the most typical ones encountered in the trickle flow regime (Figure 2.2). Their incidence is predominantly determined by the value of liquid superficial velocity. Rivulet and filament flow are more likely to occur at lower liquid superficial velocity while film flow develops for the higher values of liquid velocity. Film flow is an indication of higher liquid holdup and more uniform liquid flow, and leads to the highest gas-liquid interfacial areas. Both of these conditions are penalized by higher pressure drop due to higher gas-liquid interactions. Rivulet and filament flow are more or less segregated type of flow with poor liquid spreading and lessened gas-liquid interactions. Thus, film flow is the most desirable type of flow for typical industrial TBR operation. The study of Charpentier et al., 1968, for example, presented the quantitative assessment (obtained by electrical conductivity measurements) of the fraction of holdup associated with these types of flow patterns. For the conditions of their experimental study, approximately 40% of total liquid holdup was in film flow, 30% was in rivulet flow and the rest was in isolated (stagnant) conditions (not identically equal, but closely related to static liquid holdup).

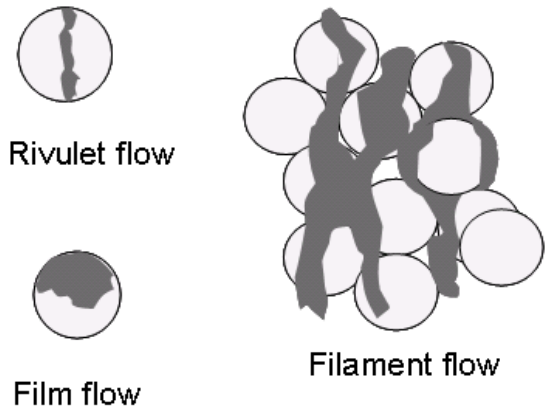

Figure 2.2 Flow patterns

More recent studies of Lutran et al., 1991, and Basavaraj et al., 2005 have provided the proof (via X-ray computed tomography) for the change in flow patterns with the change in liquid velocity. van Houwelingen et al., 2006 (and in a similar study Baussaron et al., 2007) have experimentally obtained the particle wetting distribution in trickle flow. (Their method was colorimetric: the colorant was introduced into liquid phase and flown for a sufficient time to allow coloring of the contacted packing particles. The particles were then removed from the bed, photographed and the fraction of packing particles surface area covered with colorant was obtained using image processing software. The fraction of packing particles surface area covered with colorant was assumed to be actively wetted and equal to wetting efficiency.) Some of their results indicate bimodal distribution of wetting efficiencies in the reactor that appear to be a sign of the presence of two types of flow (rivulet and film flow) the extent of each seemingly dependent on the prewetting procedure and the operating flow rates.

2.3 Flow distribution studies

Before going into more details about the studies on flow distribution, we want to point out two major trends that are evident when examining last two decades of TBR literature. First, the experimental investigation of the flow distribution in TBRs has been greatly influenced by the advance in the application of the non-invasive imaging techniques that represent valuable addition to the more traditional ones, such as residence time distribution (RTD) studies and collection of effluent liquid fluxes. At this moment it is possible to (non-invasively) obtain a porosity map, local holdups, local wetting efficiencies, velocity fields (only in small tubes using MRI) and even track the progression of conversion down a trickle bed reactor (again in small tubes by NMR) . The progress in the use of gamma and X-ray tomography, magnetic resonance imaging (MRI), radioactive particle tracking, electrical capacitance tomography (ECT) and positron emission tomography for the investigation of multiphase systems is reviewed in Moslemian et al., 1992; Gladden and Alexander, 1996; Chaouki et al., 1997a; Chaouki et al., 1997b; Godfroy et al., 1997; Reinecke et al., 1998; Larachi and Chaouki, 2000; Dudukovic, 2000; Tayebi et al., 2001; Boyer et al., 2002; Gotz et al., 2002; Chen et al., 2002; Barigou, 2004; Stapf and Han, 2005; Ismail et al., 2005; Tibirna et al., 2006; Gladden, 2006; Elkins and Alley, 2007, and Llamas et al., 2008b. However, one should keep in mind that each of these techniques has its own spatial and temporal resolutions limitations with respect to the size of the reactor and operating pressure to which it can be applied.

Second, in the last two decades big effort was made in studying high pressure trickle bed reactors since elevated pressure directly affects the level of interaction between flowing phases and is industrially more relevant than the low pressure operation (Al-Dahhan et al., 1997). For example, favorable effects of the elevated pressure were noticed in terms of improved wetting efficiency and liquid distribution but coupled with the increased pressure drop (Ellman et al., 1988; Ellman et al., 1990; Wammes et al., 1991; Larachi et al., 1991; Ring and Missen, 1991; Larachi et al., 1992; Al-Dahhan and Dudukovic, 1994; Al-Dahhan and Dudukovic, 1995; Al-Dahhan et al., 1998; Harter et al., 2001; Kundu et al., 2002; Kundu et al., 2003b; Iliuta et al., 2005; Boyer et al., 2007, and Aydin and Larachi, 2008).

Flow distribution in TBRs is influenced by liquid and gas phases' properties and flow rates, operating pressure, size, shape and orientation of the particles in the bed, packing methodology, inlet distributor design, reactor length, column to particle diameter ratio, and liquid-solid wettability.

Macroscopically, the flow of both phases in large scale TBR with no gross maldistribution is generally close to plug flow and this represents one of the advantages of using this type of contactors (Sie and Krishna, 1998). Laboratory scale TBRs have values of liquid phase Peclet number of about 10 (van Klinken and van Dongen, 1980;

Alicilar et al., 1994, and Saroha et al., 1998a), unless bed dilution[1] is employed which then raises the values to about 70 (van Klinken and van Dongen, 1980). Some of the studies performed on the commercial scale TBRs (see for example Kennedy and Jaffe, 1986) have shown that at low liquid velocities the liquid flow distribution can show serious deviations from plug flow. A double peaked RTD was observed and attributed to channeling (rivulet flow). Unfortunately, the bed and packing geometry, as well as operating flow rates are not reported in the studies of the commercial reactors, limiting our proper insight into these results.

Proper design of the inlet distributor is crucial in order to achieve uniform liquid distribution in TBRs. Ideally, inlet distributor should dispense the liquid phase uniformly at the top of the column thus facilitating the uniformity of liquid distribution in the remainder of the bed. (Various distributor designs used in the industrial TBRs are thoroughly reviewed in Maiti and Nigam, 2007.) Studies reveal that if liquid is introduced non-uniformly at the top of the bed, the flow distribution is not likely to improve down the bed even for the conditions of the high gas velocity (Maiti and Nigam, 2007, and Llamas et al., 2008a). The flow distribution is distinctly different for the different types of inlet distributor and improves when going from the point, line, multi-

[1] Bed dilution is the introduction of fine inert particles (with size in the range of a fraction of a millimeter) in the lab TBR to improve liquid distribution. This is recommended procedure when obtaining conversion data in TBR under low velocity conditions. These conditions lead to poor liquid distribution which in turn reduces achieved conversion. Thus, bed dilution is a process for decoupling hydrodynamics from reaction kinetics in lab scale TBR (see Wu, Y., Khadilkar, M. R., Al-Dahhan, M. H. and Dudukovic, M. P. (1996). "Comparison of upflow and downflow two-phase flow packed-bed reactors with and without fines: experimental observations." Industrial & Engineering Chemistry Research 35(2): 397-405.)

point, to uniform distributor (Ravindra et al., 1997, and Marcandelli et al., 2000). Experimental studies of the flow distribution in TBRs equipped with the non-uniform distributors (i.e., point or line distributor) seem unwarranted as they, for the obvious reasons, are not used in practice. However, such studies provide good insight into the prediction capabilities of the hydrodynamic models (see for example Boyer et al., 2005) and help examine the effect of various operating parameters (as discussed in the remained of this chapter) on the resulting flow distribution.

The value of liquid flux (or equivalently liquid velocity) is the most predominant factor influencing the quality of the flow distribution. Flow distribution improves with the increase in liquid velocity. For the lower values of liquid velocity (Herskowitz and Smith, 1983 proposed $L<4$ kg/m^{2}s) the liquid channeling is present leading to small gas-liquid interfacial area and poor catalyst utilization. The flow of the phases is segregated and usually anticipated as the rivulet or filament flow (see Figure 2.2). With the increase in liquid velocity, the flow becomes more uniform and starts approaching the desirable film flow pattern. Numerous studies, either via the non-invasive flow visualization or the collection of effluent liquid fluxes, have verified this trend (Lutran et al., 1991; Ravindra et al., 1997; Saroha et al., 1998b; Toye et al., 1999; Marchot et al., 1999; Marcandelli et al., 2000, and Kundu et al., 2001). For the fixed value of liquid velocity, the increase in gas-liquid interactions improves the liquid distribution. Hence, the increase in gas velocity and operating pressure will both lead to a more uniform liquid distribution (see the list of references related to the high pressure studies given above).

The effect of liquid density on the flow distribution is tied to the role of the gravitational force in TBR hydrodynamics. Gravity tends to take the liquid down the path of the least resistance. Hence, reducing the liquid density is expected to improve liquid phase distribution since the gravitational effects are directly proportional to the phase density. This has been verified in the experimental studies by Saroha et al., 1998b, and Kundu et al., 2001.

Surface tension is the stabilizing force in the trickle flow regime. First experimental indication was given by Chou et al., 1977 who examined trickle-to-pulse transition for the conditions of the reduced surface tension of the liquid phase. The transition shifts towards the lower liquid velocities once the liquid phase surface tension is reduced. Also, most of the models developed for the trickle to pulsing flow regime transition (Grosser et al., 1988; Holub et al., 1992b, and Attou and Ferschneider, 1999) do indicate the need to include surface tension in the analysis since in the resulting equations inertia acts as the destabilizing force while surface tension is the stabilizing force. Thus, one can expect improved liquid distribution if the surface tension of the liquid phase is reduced and this has been verified in the experiments performed by Kundu et al., 2001.

As the particle size increases the void volume available for flow increases while solid surface area decreases. Thus, with increasing particle size the packing represents less of a flow resistance; flow is gravity dominated which leads to a poor (non-uniform) liquid distribution and rivulet flow. (For the interplay of forces governing flow distribution see

also the phenomenological analysis of Al-Dahhan and Dudukovic, 1994, and the criteria for the complete wetting proposed by Gierman, 1988). Such effect of particle size on the resulting flow distribution has been verified in the studies of Ravindra et al., 1997. Packing particles' shape and orientation determine the geometry of voids and the shape of the surface across which the liquid flows. Trivizadakis et al., 2006 have shown that extrudates (cylindrically shaped particles) provide better liquid distribution and higher liquid holdup when compared with the spherical particles. Tukac and Hanika, 1992 used different packing methodologies to achieve two different extrudate particles orientations: random and ordered (horizontal). Their experimental studies reveal better flow distribution, less of the axial dispersion effects and higher liquid holdup for the case of a bed with predominantly horizontally oriented extrudates. The authors recommended the use of dense packing method to achieve such conditions. Internally porous particles show different behavior than the non-porous particles. Studies of a liquid spreading from a point distributor show that porous particles, for all the other conditions being identical, tend to lead to a better liquid distribution than their non-porous counterparts (Ravindra et al., 1997, and Schubert et al., 2008).

The studies of flow distribution are closely related to the studies of hysteresis in TBRs. The hydrodynamic parameters such as pressure drop and liquid holdup are not only determined by the operating conditions but also show dependence on the flow history of the bed. Flow history, for example, is simply the range of phase velocities the bed experienced before the current operating conditions were set. Hysteresis is attributed to

the change in flow distribution and related flow patterns with the flow history (Christensen et al., 1986). Hence, the trends as to how various variables affect the extent of hysteresis (the magnitude of the difference between the pressure drops in two states at identical operating conditions achieved through different flow history) should identically follow the trends in the effect of these variables on liquid flow distribution. In other words, all the factors improving the flow distribution should be reducing the extent of hysteresis. Indeed, it has been shown that reducing the liquid surface tension reduces the extent of hysteresis (Kan and Greenfield, 1978; Christensen et al., 1986; Levec et al., 1988, and Wang et al., 1995). If different flow history is achieved by the variation of liquid phase velocity the resulting extent of hysteresis is larger than if the same is done by varying gas phase velocity (Christensen et al., 1986; Wang et al., 1995, and Lazzaroni et al., 1989). Increasing gas velocity and operating pressure reduces the extent of hysteresis (Kuzeljevic et al., 2008). When starting from a dry bed, porous particles tend to exhibit a lower extent of hysteresis than non-porous particles (Maiti et al., 2005). Larger packing particles exhibit less pronounced hysteresis (Kan and Greenfield, 1978, and Levec et al., 1988). Note that the last statement does not negate the direct relationship between the flow distribution and hysteresis. For larger particles, the flow history does not play a significant role since the flow never reaches the limit of film flow. Thus, there is no significant change in flow patterns and flow distribution and hence there is no pronounced hysteresis. The comprehensive review of hysteresis studies is given in Maiti et al., 2006.

2.4 Phenomenological modeling

Two basic approaches to modeling the flow in TBRs are the empirical correlations and phenomenological (semi-empirical, mechanistic) models. Most of the recent developments in the empirical correlations are for the prediction of pressure drop, liquid holdup and wetting efficiency in a high pressure trickle bed reactor (Ellman et al., 1988; Ellman et al., 1990; Wammes et al., 1991; Larachi et al., 1991; Lange et al., 2005, see also Al-Dahhan et al., 1997 and references therein). Recently, the neural network correlations that are based on the extensive experimental database have been developed (Larachi and Grandjean, 2003, and Larachi et al., 1999). Detailed discussion of empirical correlations is beyond the scope of this review.

In order to discuss the phenomenological models in more systematic way, we present first the theoretical foundations of the proposed models. Then, we take a look at how these foundations are shaped into specific models. Interested reader can find more details on the general theory of the flow through porous media in Scheidegger, 1957; Bear, 1972; Ewing, 1991; Dullien, 1992; Lage, 1998, and Dullien, 1998.

2.4.1 Basic principles

Darcy, 1856 proposed a linear relation between pressure gradient and the resulting superficial velocity in a saturated (one phase) flow through porous media. To account for the experimentally observed deviation from linearity in the pressure gradient – superficial

velocity dependence, Forchheimer, 1914 proposed the modification by using two parameters, namely *permeability* (k_α) and *passability* (η_α), to quantify the viscous and inertial contributions to pressure losses, respectively, as given in equation (2-1).

$$-\frac{dP}{dz} = \frac{\mu_\alpha U_\alpha}{k_\alpha} + \frac{\rho_\alpha U_\alpha^{\,2}}{\eta_\alpha} \tag{2-1}$$

The theoretical development of the proper representation of permeability and passability was initiated by Kozeny, 1927 and an ongoing research effort continues to the present time (see the discussion in Dullien, 1992). The most commonly used semi-empirical approach for estimation of pressure drop in one phase flow through packed beds is due to Ergun, 1952, who, based on extensive experimental investigation, defined the parameters of equation (2-1) as

$$k_\alpha = \frac{\varepsilon_B^3 d_p^{\,2}}{E_1(1-\varepsilon_B)^2}$$

$$\eta_\alpha = \frac{\varepsilon_B^3 d_p}{E_2(1-\varepsilon_B)}. \tag{2-2}$$

This equation provides very good estimates of pressure drop provided that the parameters E_1 and E_2 are fitted to the one phase flow pressure drop data obtained in the system of interest (McDonald et al., 1979).

Muskat and Meres, 1936 proposed the extension of the Forchheimer-Darcy's equation to two phase flow by defining the *relative permeability* that accounts for the presence of the other flowing phase. Here, we reformulate their original expression by formally

introducing separate relative permeabilities for viscous and inertial contribution as given in equation (2-3).

$$-\frac{dP_\alpha}{dz} = \frac{\mu_\alpha U_\alpha}{K_\alpha k_\alpha} + \frac{\rho_\alpha U_\alpha{}^2}{K_{i,\alpha}\eta_\alpha}$$

$$\lim\{K_\alpha \mid \varepsilon_\alpha \to 1\} \to 1 \qquad (2\text{-}3)$$

$$\lim\{K_{i,\alpha} \mid \varepsilon_\alpha \to 1\} \to 1$$

Note that Darcy's law for one phase flow is valid once permeability is specified (theoretically or experimentally) for the system of interest. Also, over fifty years of research have proven that Ergun's permeability and passability expressions are exclusively characterized by the packed bed structure and are not dependent on the fluids used or the operating conditions employed. On the other hand, equation (2-3) is simply the heuristic extension (Hassanizadeh and Gray, 1993) of the original postulate. Thus, estimating the relative permeability for a system at a given conditions does not guarantee that the same value (or functional dependence) can be generalized across different gas and liquid phase properties or operating conditions (Bear, 1972).

The second basic approach involves the use of the Navier-Stokes equation that is set for the prescribed model geometry. For completeness sake, the Navier-Stokes expression is included here as equation (2-4), (Bird et al., 2001).

$$\rho\frac{D\vec{u}}{Dt} = \rho\vec{g} - \nabla P + \mu\nabla^2\vec{u} \qquad (2\text{-}4)$$

The volume averaged momentum equation is also commonly employed in the phenomenological description of TBRs. For the case of incompressible laminar flow, it is given by equation (2-5). The basic advantage of this approach is that specific geometry of the packing structure is not necessary for model derivation. However, in the averaged equations the phase interactions are not a part of the solution outcome, rather, they need to be specified as the input to the model (Drew, 1983).

$$\frac{\partial}{\partial t}\left(\varepsilon_\alpha \rho_\alpha \vec{u}_\alpha\right) + \nabla \cdot \left(\varepsilon_\alpha \rho_\alpha \vec{u}_\alpha \vec{u}_\alpha\right) = -\varepsilon_\alpha \nabla P_\alpha + \varepsilon_\alpha \rho_\alpha \vec{g} - \vec{F}_\alpha + \mu_\alpha \nabla^2 \vec{u}_\alpha \tag{2-5}$$

2.4.2 Capillary effects

Capillary effects lead to the difference in the pressure across the interfacial surface separating two immiscible phases. They are important in TBRs due to the small length scale of the interstitial voids bounded by the packing particles' surface. Young-Laplace equation (2-6) provides the exact value of the capillary pressure, i.e., the pressure difference between non-wetting and wetting fluid side of the interface (see Figure 2.3 for definition of wetting and non-wetting phase).

$$P_c = \frac{2\sigma}{H}\cos\theta \tag{2-6}$$

The Young-Laplace equation requires not easily attainable values of the contact angle and mean curvature of the interface. Instead, as proposed by Leverett, 1941, capillary pressure can be correlated to the wetting phase saturation (see Figure 2.4). Even though

this relation can be questioned[2] since it, indirectly, postulates the dependence of contact angle and radii of curvature on the saturation (Hassanizadeh and Gray, 1993), it still provides the best means for capillary pressure estimates. Figure 2.4 has a couple of interesting features. Curves indicate the existence of hysteresis which can be explained by the non-uniform size of the voids or by the difference in the values of advancing and receding contact angle (see Dullien, 1992).

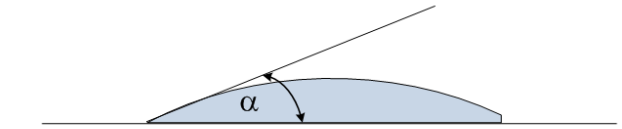

(a)

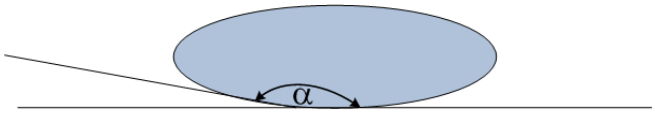

(b)

Figure 2.3. Liquid phase (a) wetting ($\alpha<90^0$), and (b) not wetting ($\alpha>90^0$) the solid phase (by extension, gas phase is considered in cases (a) and (b) as non-wetting and wetting, respectively. The value of the contact angle (α) is determined by the values of liquid-gas, liquid-solid and solid-gas surface energies.

[2] Contact angle and radii of curvature are determined by the values of liquid-gas, liquid-solid and solid-gas surface energies.

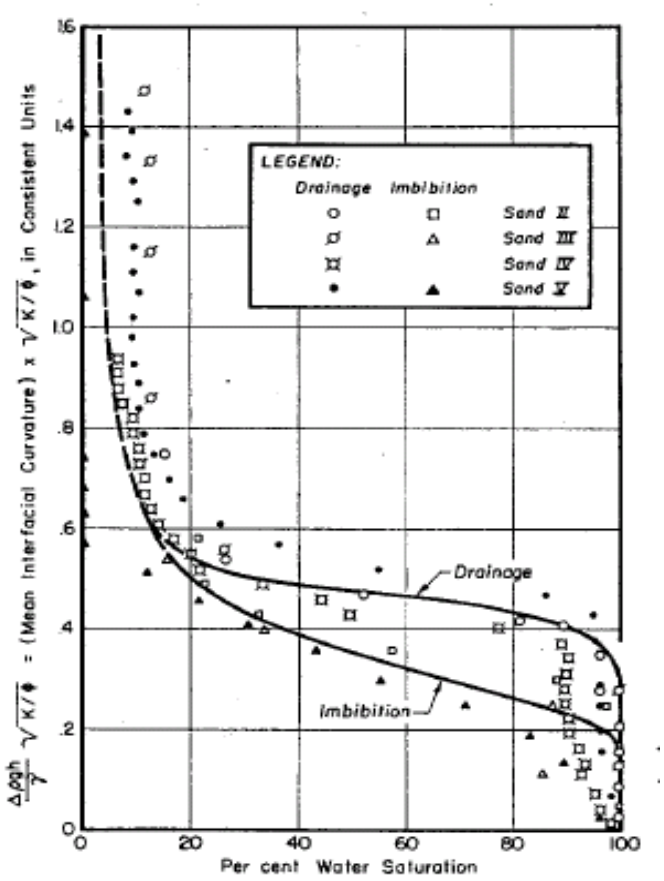

Figure 2.4 Capillary pressure dependence on wetting phase saturation (from Leverett, 1941)

Capillary pressure decreases as the wetting phase saturation increases, the reason being that non-wetting fluid, during drainage, first forces the wetting fluid from the biggest pores (less pronounced capillary effect) and then from smaller pores (more pronounced capillary effect). Irrespective of the pressure applied some portion of the wetting phase always remains in the porous media. (Recall the static liquid holdup which is a consequence of the loss of continuity in liquid phase during drainage and is held by capillary forces at the contact points of the packing particles.)

Capillary pressure naturally enters the modeling equations presented above as, for example, the pressure used in volume averaged equations for the two phases will differ by its value.

2.4.3 Relative permeability model

The concept of relative permeability was first introduced into the TBR modeling by Saez and Carbonell, 1985. Their approach utilizes one dimensional, steady state volume averaged momentum equation (given here as equation (2-5)) with the inertial and viscous contribution neglected. This effectively leads to the equality of the pressure drop gradient in each phase to the drag exerted on it. Two phase flow drag for each of the phases is obtained by dividing the viscous and inertial terms of the Ergun equation (2-2) by the viscous and inertial relative permeabilities, respectively, thus leading to a four parameter model of trickle flow. Hence, Saez and Carbonell, 1985, model equations are obtained by inserting Ergun's definition of permeability and passability (equation (2-2)) into the Muskat and Meres, 1936 expression yielding equation (2-7).

$$-\frac{dP_\alpha}{dz} = E_1 \frac{\mu_\alpha U_\alpha (1-\varepsilon_B)^2}{K_\alpha \varepsilon_B^3 d_p^{\ 2}} + E_2 \frac{\rho_\alpha U_\alpha^{\ 2} (1-\varepsilon_B)}{K_{i,\alpha} \varepsilon_B^3 d_p} \tag{2-7}$$

Capillary effects were neglected in their analysis. Four parameters of the model are fitted against the experimental data to provide their functional dependence on phase saturations (given in Table 2.2). As the outcome of the fitting process, the four parameter model was reduced to two parameter model, since the inertial and viscous relative permeabilities were found equal. The approach of Saez and Carbonell, 1985 was

extended by Lakota et al., 2002, and Nemec and Levec, 2005. Based on their own set of experimental data, these authors proposed different expressions for the relative permeabilities (Table 2.2). Lakota et al., 2002 found the gas phase relative permeability dependent on the shape of packing particle (parameter χ) and on Reynolds number. Nemec and Levec, 2005 proposed separate expressions for film and rivulet flow that were based on the experimental results of the upper and lower branch of the hysteresis loop

Table 2.2 Dependence of relative permeabilities on phase saturations*

Reference	Gas phase relative permeability	Liquid phase relative permeability
Saez and Carbonell, 1985	$S_G^{4,8}$	$\delta_L^{2.43}$
Lakota et al., 2002	$S_G^{\chi+0.0478\mathrm{Re}_G^{0.774}}$	$\delta_L^{2.49}$, for $\delta_L \geq 0.3$ $0.40\delta_L^{2.1}$, for $\delta_L < 0.3$
Nemec and Levec, 2005	$0.40S_G^{3.6}$, for $S_G < 0.64$ $0.40S_G^{5.5}$, for $S_G \geq 0.64$	$\delta_L^{2.9}$, for film flow δ_L^{2}, for rivulet flow

* For symbols see notation

(see also Maiti et al., 2006). Also, they found two separate expressions for the liquid phase relative permeability depending on the value of the reduced liquid saturation (δ_L).

2.4.4 F-function model

F-function model (Fourar et al., 2001, and Radilla et al., 2005) is based on the Forchheimer-Darcy's law, equation (2-1), and extended to two phase flow conditions by introducing the "accommodation" F-function to account for the hindrance exerted by the

other flowing phase. The derivation and the assumptions used are very similar to the Saez and Carbonell, 1985 model. However, in this case, the fitting parameters are formulated in a different way and in the model equation they appear as multipliers of the phase superficial velocity as given in equation (2-8):

$$-\frac{dP_\alpha}{dz} = E_1 \frac{\mu_\alpha (1-\varepsilon_B)^2}{\varepsilon_B^3 d_p^{\ 2}} (F_{f,\alpha} U_\alpha) + E_2 \frac{\rho_\alpha U_\alpha^{\ 2} (1-\varepsilon_B)}{\varepsilon_B^3 d_p} (F_{f,\alpha} U_\alpha)^2 \tag{2-8}$$

2.4.5 Slit models

Holub et al., 1992a, and Holub et al., 1992b (see also Sweeney, 1967), modeled the flow in TBR by using the local momentum conservation (Navier-Stokes) equation. Such local momentum equations were derived for a steady, fully-developed two phase flow on an inclined slit as shown in equation (2-9):

$$\begin{aligned} -\frac{dP_G}{dz} + \rho_G \cos\theta_{slit} &= \frac{\tau_{LG}}{w_{slit} - \delta_{slit}} \\ -\frac{dP_L}{dz} + \rho_L \cos\theta_{slit} &= \frac{\tau_W}{\delta_{slit}} \end{aligned} \tag{2-9}$$

The geometry of the model is obtained by mapping the overall bed properties (void to solid and liquid to solid volumetric ratios) to the slit parameters. Slit inclination angle is related to the bed tortuosity. The model assumes uniform liquid distribution, film flow, complete wetting of catalyst particle, and neglects the change in pressure across the gas-liquid interface (no capillary effects). Shear stresses in equation (2-9) are assumed to have Ergun like dependence on phase velocities and properties. Even though the model

represents an oversimplification of the actual trickle flow it did show reasonably good agreement with experimental data in the trickle flow regime.

Holub et al., 1992a, and Saez and Carbonell, 1985 models are derived from a different starting point, i.e., local momentum equation for prescribed geometry, and averaged momentum equation and no geometry assumed, respectively. However, due to the use of Ergun style expressions for interphase drag in both models, and mapping of slit geometry to overall bed properties in the Holub et al., 1992b model, the resulting expressions for pressure drop are very similar. For example, in the expression for liquid phase pressure gradient there is a cubic dependence on the liquid holdup in the slit model and the power dependence with exponent 2.43 in the relative permeability model.

The slit model has been extended by Al-Dahhan et al., 1998 for a high pressure operation. As discussed above, high pressure operation increases gas-liquid interactions and thus increases the error in the slit model predictions. The authors proposed to model the degree of gas-liquid interaction through the use of velocity and shear stress slip factors defined for the gas-liquid interface. These factors are used to relate the velocities and shear stresses on either side of the interface. Unfortunately, due to very limited data base used for fitting the slip coefficients, their values show very weak dependence on the gas and liquid phase Reynolds numbers. Also, the values of both factors violate the requirement for velocity and shear stresses continuity across the interface. As the expression for the velocity slip factor gives invariably negative values, the model then

implies that gas and liquid velocity vectors have the opposite direction. However, it should be noted that this is not a model postulate, but rather the result of fitting. The authors showed that the extended model matched pressure drop data better for the elevated pressure conditions in the trickle flow regime.

In a series of papers, Larachi and collaborators have proposed multiple extensions of the slit model (see the comprehensive review in Iliuta and Larachi, 2005). The authors incorporated the partial wetting into the model by assuming flow through two slits. One slit is assumed to be completely dry and the other completely wetted. The specific areas associated with each type of slit are estimated based on the liquid-solid wetting efficiency. The authors proposed the use of gas-liquid interaction factor as the parameter that describes the degree of interaction between gas and liquid phase instead of velocity and shear stress factors. They reformulated Al-Dahhan et al., 1998 derivation in order to satisfy the continuity of shear stresses and velocities at the interface. Newly proposed interaction factor is correlated to operating conditions via neural network correlation based on the extensive experimental database (Iliuta et al., 2002). The model showed improved predictions (see Larachi et al., 2000).

2.4.6 Two fluid model

The two fluid model (Attou et al., 1999) is based on the one dimensional, steady state volume averaged momentum equations for gas and liquid phases in which viscous terms are neglected. The capillary effects have been neglected for the modeling of pressure

drop and liquid holdup, even though in a separate study of flow regime transition (Attou and Ferschneider, 1999) these effects have been considered. Note that contrary to models discussed so far, this model does not neglect the gradient of velocity in the momentum equations. In other words, model accounts for the inertial effects. The authors have also provided gas-liquid, gas-solid and liquid-solid interaction terms to close the model. For this purpose, they assumed film flow with the complete wetting of catalyst surface. The derivation is based on the Ergun equation, and accounts for the change in the diameter, tortuosity and porosity that each phase experiences due to the presence of the other flowing phase. For the calculation of the *liquid-solid drag*, tortuosity was assumed as inversely proportional to liquid phase saturation. Effective porosity was set to the value of liquid holdup. For the *gas-liquid interaction* the single phase gas velocity (as used in the Ergun equation) was replaced with the relative (slip) gas-liquid velocity. Effective porosity was set to values of gas holdup. The argument is made that in two phase flow the gas phase flows across the particles having an effective diameter larger than the actual particles diameter due to the presence of a liquid film covering the particles. Thus, the effective diameter was estimated by geometrical considerations and expressed as a function of liquid holdup. The *gas-solid interaction* was modeled with the same expression as the gas-liquid interaction, but using gas phase velocity instead of slip velocity since for the case of complete wetting the gas interacts with solids only across the liquid films.

Boyer et al., 2007 examined the Attou et al., 1999 model predictions for systems with the non-aqueous liquid phase. They found that the tortuosity factor used in liquid-solid drag has to be separately specified for organic liquid phase (~ $S_L^{-0.02}$) and aqueous liquid phase (~$S_L^{-0.54}$). The authors explained the need for two expressions by the difference between the surface tension of the aqueous (about 0.07 N/m) and organic liquids (0.01 – 0.02 N/m). The higher surface tension leads to the greater curvature of the gas-liquid interface increasing the tortuosity of the flow path (Boyer et al., 2007).

The other modeling approaches used in hydrodynamic investigation of TBRs are not discussed in detail here. For completeness, we just mention a couple of them. Crine et al., 1979, and Crine and Marchot, 1984 have modeled flow distribution in TBR using percolation theory. This model was later extended by Fox, 1987. Melli et al., 1990 set the model by considering the events happening in the voids and in the passages leading to the voids. Zimmerman and Ng, 1986, and Zimmerman et al., 1987 performed their simulations on the computer generated packing of spheres by considering events on the particle scale. Rao et al., 1983 have set the model with the Ergun type expressions that are extended to the two phase flow conditions.

Comparative review and general discussion of the modeling of flows in TBRs can be found in Kuipers and Van Swaaij, 1997; Larachi et al., 2000 (includes comparison of various models' predictions with the extensive experimental database); Carbonell, 2000; Sundaresan, 2000, and Tayebi et al., 2001.

2.5 CFD modeling

In this text, we focus on the Eulerian CFD model of TBRs. For the other approaches, such as volume of fluid (VOF), see Raynal and Harter, 2001; Gunjal et al., 2005b; Lopes and Quinta-Ferreira, 2008a, and Augier et al., 2008.

2.5.1 Governing equations

Governing equations for the Eulerian CFD model are the volume averaged mass and momentum conservation equations (Anderson and Jackson, 1967, Ishii, 1975, Drew, 1983, and Bird et al., 2001):

$$\frac{\partial}{\partial t}\left(\varepsilon_\alpha \rho_\alpha\right)+\nabla\cdot\left(\varepsilon_\alpha \rho_\alpha \vec{u}_\alpha\right)=0 \tag{2-10}$$

$$\frac{\partial}{\partial t}\left(\varepsilon_\alpha \rho_\alpha \vec{u}_\alpha\right)+\nabla\cdot\left(\varepsilon_\alpha \rho_\alpha \vec{u}_\alpha \vec{u}_\alpha\right)=-\varepsilon_\alpha \nabla P_\alpha+\varepsilon_\alpha \rho_\alpha \vec{g}+ \nabla\cdot[\bar{\bar{\tau}}_\alpha+\bar{\bar{\tau}}_\alpha^{(t)}]+\vec{F}_\alpha \tag{2-11}$$

$$\vec{F_\alpha}=\sum_{\beta=1}^{n} K_{\beta\alpha}\left(\vec{u}_\beta-\vec{u}_\alpha\right) \tag{2-12}$$

$$\bar{\bar{\tau}}_\alpha=\varepsilon_\alpha \mu_\alpha\left(\nabla\vec{u}_\alpha+\left(\nabla\vec{u}_\alpha\right)^T\right) \tag{2-13}$$

$$\bar{\bar{\tau}}_\alpha^{(t)}=-\varepsilon_\alpha \rho_\alpha \overline{u_\alpha' u_\alpha'} \tag{2-14}$$

Equations (2-10) through (2-14) are valid for the Newtonian (constant viscosity) fluid with constant density and no mass transfer between the phases. In this approach, phases are assumed to coexist in each computational cell, and occupy certain volume in it given

through volume fractions (ε_α). Phases interact one with another to the degree specified by the phase interaction term, equation (2-12). Note that, as discussed earlier, the particle scale geometry does not appear in the model directly, but through the interaction closures.

Large scale turbulence has not been detected in TBRs due to the dissipating effect of the packing (Lage, 1998, and Grosser et al., 1988). Hence, typically, Reynolds's stresses, equation (2-14), are neglected in the analysis of trickle flow (Propp et al., 2000; Jiang et al., 2002a; Gunjal et al., 2005a, and Boyer et al., 2005), but some authors have used *k*-ε model to include turbulence effects (Lopes and Quinta-Ferreira, 2008b).

Choudhary et al., 1976, based on their computational study, have proposed to neglect inertial effects in the analysis of flow through packed beds. As shown earlier, this notion has been widely adopted in the phenomenological modeling of TBRs. In the CFD approach, some authors have also neglected the gradient in the phase velocities (Alopaeus et al., 2006), but most of the studies do include this term. In general, this term should be included if the porosity variation is specified on the computational domain (more on this below), especially if the sharp increase of porosity in the near wall region is considered in the simulation. Also, if any structural obstacles are present on the domain, inertial effects should not be neglected (Jiang et al., 2000).

Equations (2-10) through (2-14) indicate that to complete the model, porosity and phase interactions need to be specified. Also, as discussed earlier, capillary effects lead to the different pressures in the phases; the expression characterizing this difference (capillary closure) is also needed to close the model.

2.5.2 Porosity studies and implementation in the model

Studies of Roblee et al., 1958; Benenati and Brosilow, 1962; Stephenson and Stewart, 1986, and Mueller, 1991, have presented the longitudinally averaged variation of porosity in the radial direction. Near wall region (about five to ten packing particles from the wall) exhibits large oscillations in the values of porosity that are dampened at larger distances from the wall. In the interior of the bed, the value of porosity shows much less variation and reaches the value of the average bed porosity. This trend has also been observed in the recent MRI studies by Mantle et al., 2001. Further insight into porosity distribution was mainly gained using MRI. Baldwin et al., 1996 showed that the porosity distribution follows a pseudo Gaussian distribution. Pore sizes range from about 1 mm to the diameter of the packing particle, with the mean at about the half size of the packing particle size.

Jiang et al., 2002a proposed a way to incorporate porosity description in the Eulerian model. Using Mueller, 1991 correlation given in equation (2-15) radial porosity profile is calculated. On the computational grid, a number of sections are identified in the radial

direction. By integrating the radial profile, as shown in equation (2-16), an average value of porosity is assigned to each section. Each radial section is then assumed to exhibit a Gaussian distribution of porosity around the calculated mean for that radial position.

$$\begin{aligned} &\varepsilon_B(r) = \varepsilon_B + (1-\varepsilon_B) J_0(ar^*) \exp(-br^*) \\ &(a,b) = f(D_c, d_p),\ r^* = r/d_p \end{aligned} \tag{2-15}$$

$$\left\langle \varepsilon_{B_i} \right\rangle = \frac{1}{r_i^{end} - r_i^{init}} \int_{r_i^{init}}^{r_i^{end}} \varepsilon_B(r) dr \tag{2-16}$$

2.5.3 Phase interaction closures

Phenomenological models (section 2.4) represent the basis for the phase interaction closures used in CFD modeling. The resulting expressions are summarized in Table 2.3 and given in terms of the momentum exchange coefficient $K_{\beta\alpha}$, equation (2-12). Note that the closures for the double slit model are not shown here. Due to the use of neural network correlations, the resulting expressions are quite cumbersome. This model offers gas-liquid, gas-solid and liquid-solid interactions closures which can be found in Iliuta et al., 2002 and Iliuta and Larachi, 2005.

2.5.4 Capillary closure

As shown in Section 2.4.2, the pressure difference between the non-wetting and wetting fluid can be estimated using equation (2-6) if the values of radii of curvature and the contact angle are known, , or it can be correlated to the saturation of the wetting fluid (Figure 2.4). Both of these approaches are utilized in TBR modeling. Grosser et al., 1988

have fitted the Leverett, 1941 drainage curve (see Figure 2.4) as given in equation (2-17) and proposed to use the resulting expression to estimate capillary pressure in TBR. On the other hand, Attou and Ferschneider, 1999, based on the

$$P_c = \frac{\sigma \varepsilon_S E_1^{\,0.5}}{\varepsilon_B d_p}\left[0.48 + 0.036 \ln\left(\frac{\varepsilon_B - \varepsilon_L}{\varepsilon_L}\right)\right] \tag{2-17}$$

Table 2.3 Exchange momentum coefficients

Authors	Exchange momentum coefficients, kg/m^{3}s	
Attou et al., 1999	$K_{GL} = \frac{E_1(1-\varepsilon_G)^2}{\varepsilon_G d_p^2}\left(\frac{1-\varepsilon_B}{1-\varepsilon_G}\right)^{2/3}\mu_G + \frac{E_2(1-\varepsilon_G)}{d_p}\left(\frac{1-\varepsilon_B}{1-\varepsilon_G}\right)^{1/3}\rho_G\lvert\vec{u}_G - \vec{u}_L\rvert$	(2-18)
	$K_{GS} = \frac{E_1(1-\varepsilon_G)^2}{\varepsilon_G d_p^2}\left(\frac{1-\varepsilon_B}{1-\varepsilon_G}\right)^{2/3}\mu_G + \frac{E_2(1-\varepsilon_G)}{d_p}\left(\frac{1-\varepsilon_B}{1-\varepsilon_G}\right)^{1/3}\rho_G\lvert\vec{u}_G\rvert$	(2-19)
	$K_{LS} = \frac{E_1(1-\varepsilon_B)^2}{\varepsilon_L d_p^2}\mu_L + \frac{E_2(1-\varepsilon_B)}{d_p}\rho_G\lvert\vec{u}_L\rvert$	(2-20)
Holub et al., 1992a	$K_{GS} = \left[\frac{E_1(1-\varepsilon_B)^2}{\varepsilon_G^3 d_p^2}\mu_G U_G + \frac{E_2(1-\varepsilon_B)}{\varepsilon_G{}^3 d_p}\rho_G U_G^2\right]\frac{1}{(1-\varepsilon_B)\lvert\vec{u}_G\rvert}$	(2-21)
	$K_{LS} = \left[\frac{E_1(1-\varepsilon_B)^2}{\varepsilon_L^3 d_p^2}\mu_L U_L + \frac{E_2(1-\varepsilon_B)}{\varepsilon_L{}^3 d_p}\rho_L U_L^2\right]\frac{1}{(1-\varepsilon_B)\lvert\vec{u}_L\rvert}$	(2-22)
Saez and Carbonell, 1985	$K_{GS} = \left[\frac{E_1(1-\varepsilon_B)^2\varepsilon_B^{1.8}}{\varepsilon_G^{4.8} d_p^2}\mu_G U_G + \frac{E_2(1-\varepsilon_B)\varepsilon_B^{1.8}}{\varepsilon_G{}^{4.8} d_p}\rho_G U_G^2\right]\frac{1}{(1-\varepsilon_B)\lvert\vec{u}_G\rvert}$	(2-23)
	$K_{LS} = \left[\frac{E_1(1-\varepsilon_B)^2}{\varepsilon_L^3 d_p^2 \delta_L^{2.43}}\mu_G U_G + \frac{E_2(1-\varepsilon_B)}{\varepsilon_L{}^3 d_p \delta_L^{2.43}}\rho_G U_G^2\right]\frac{1}{(1-\varepsilon_B)\lvert\vec{u}_L\rvert}$	(2-24)

geometrical considerations, estimated the radii of curvature of the gas-liquid interface and then included them into Young-Laplace equation. The resulting expression for the capillary pressure is given by equation (2-25). This capillary closure is derived and valid only for the conditions corresponding to trickle-to-pulse transition, but in the CFD models (Jiang et al., 2002a, Gunjal et al., 2005a) is considered valid for the entire trickle flow regime.

Note that some authors (see Souadnia and Latifi, 2001), while developing their CFD model for TBR, proposed to neglect capillary effect based on the large difference in the value of capillary pressure (~100 Pa) as compared to the operating pressure (~10^5 Pa or higher). However, capillary effects are related to the gradient of liquid phase holdups;

$$P_c = \frac{2\sigma}{d_p}\left(\frac{1-\varepsilon_B}{1-\varepsilon_G}\right)^{1/3}\left[1+\left(\frac{\sqrt{3}}{\pi}-\frac{1}{2}\right)^{-1/2}\right] \tag{2-25}$$

see equations (2-25), and (2-11). Thus, their effect cannot be judged based solely on the absolute value of capillary pressure.

In order to capture the experimentally observed distinctly better spreading of liquid from a point distributor in the prewetted bed than in the non-prewetted bed, Jiang et al., 2002a proposed the following modification of the capillary pressure:

$$P_c^{\,\mathrm{mod1}} = (1-f)P_c, \tag{2-26}$$

Hence, the effective (P_c^{mod1}) capillary pressure was assumed dependent on the wetting efficiency (f). By setting f = 1 and f = 0 for prewetted and non-prewetted beds, respectively, this modification enabled to predict better spreading of liquid in the prewetted beds. However, this approach did not yield satisfactory quantitative predictions of point source liquid spreading as compared with computed tomography experimental data discussed below.

The Eulerian CFD model has been extensively applied to TBR hydrodynamic studies in the last decade. Propp et al., 2000 (see also Souadnia and Latifi, 2001) have investigated the behavior of liquid phase front as it travels down the bed. Their study clearly outlines the effect of implementation of porosity distribution, Ergun type terms in phase interaction closures and capillary closure. Introducing the capillary term leads to the smearing of the liquid phase front as it travels down the bed. Also, capillary effects lead to the "diffusion" of liquid phase from the region of higher porosity into the region of lower porosity. The phase interaction closures reduce the speed at which the liquid front travels and increase the liquid saturation of the front. Hence, Ergun type phase interaction closures only change the magnitude but not the qualitative character of the solution, while capillary pressure term does change the character of the solution (Propp et al., 2000). Jiang et al., 2001 also investigated numerically the influence of the non-uniformity of porosity on the predictions. They found that the influence of the non-uniformity of porosity distribution (in their model specified through the standard deviation of porosity distribution) is mostly expressed through the capillary term. In other words, if the

capillary term is not included in the solution process the flow distribution will not change significantly with the increase in standard deviation of the porosity distribution. Boyer et al., 2005 studied the spreading of the liquid phase from a point distributor both

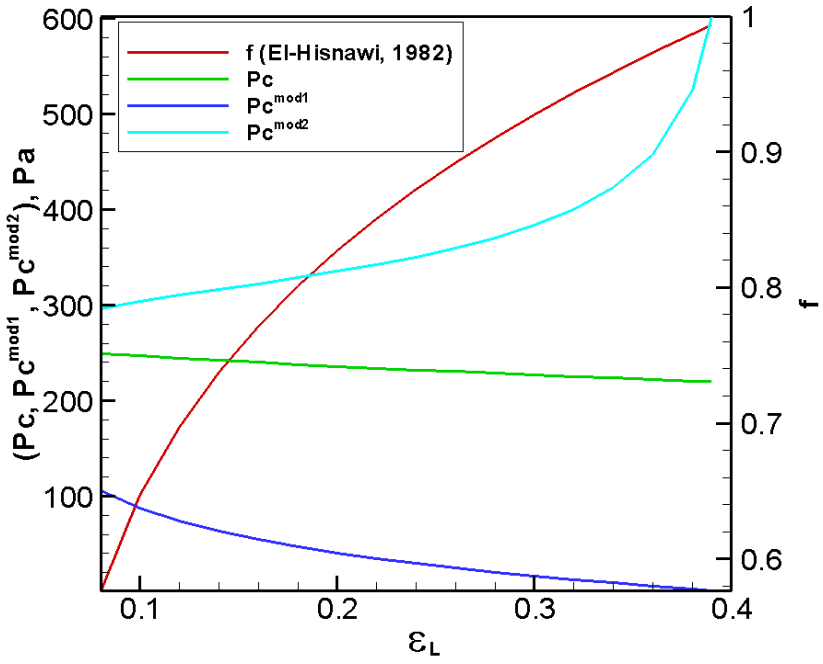

Figure 2.5. Dependence of capillary pressure expressions on liquid holdup. Pc, Pc^{mod1} and Pc^{mod2} are given by equations (2-25), (2-26), and (2-27), respectively. Wetting efficiency (f) was predicted using El-Hisnawi et al., 1982 correlation and is given on the right-hand side axis.

experimentally and numerically. The authors concluded that the prediction capabilities are very sensitive to the implementation of the capillary term. They generalized Jiang et al., 2002a (1-f) term, see equation (2-26), into $(1\text{-}f)^n$ and designated separate *negative* values of the exponent for the prewetted ($n = -0.2$) and non-prewetted ($n = -0.6$) beds, see equation (2-27). Such formulation helped bring the liquid radial spreading predictions

more closely to the experimental results, but, unfortunately, at the price of using physically unsound approach for the following reason. In Figure 2.5 the predictions of the three expressions (Attou and Ferschneider, 1999, and modifications given by equations (2-26), and (2-27)) are shown. It is evident that only Pc^{mod2} decreases with the increase in liquid holdup. However, capillary pressure should decrease as the wetting (liquid) phase saturation increases (see Section 2.4.2).

$$P_c^{\,\mathrm{mod}\,2} = (1-f)^{-0.2} P_c\,, \tag{2-27}$$

The problems in capturing the trends by Boyer et al., 2005 can be related to the issue of the dynamic effects in capillary pressure-saturation relationships. The relationship between capillary pressure and wetting phase saturation (Figure 2.4) is different for steady and unsteady state conditions. For example, the generalized expression for the capillary pressure proposed by Mirzaei and Das, 2007 is given as

$$P_c^{\,dynamic} = P_c^{\,static} + \tau_1^{\,Pc}\left(\frac{\partial S_L}{\partial t}\right) + \tau_2^{\,Pc}\left(\frac{\partial S_L}{\partial t}\right)^2. \tag{2-28}$$

Hence, if the strong gradients exist on the domain (like on the line separating gas and liquid phase during liquid spreading from a point source), implementation of the static dynamic holdup might be incorrect.

Gunjal and Ranade, 2007 studied the hydrodesulphurization in a pilot plant TBR using CFD, thus expanding the use of the model to the reacting systems. Alopaeus et al., 2006 based their interactions on the slit model and developed the CFD approach that is applicable to Newtonian and non-Newtonian fluids, high and low pressure operation, and

co and countercurrent operation. Other representative CFD studies of TBR have been performed by Bell, 2005; Atta et al., 2007a; Lopes and Quinta-Ferreira, 2008b; Lopes and Quinta-Ferreira, 2007, and Atta et al., 2007b.

At this moment, it would be instructive to further assess the Eulerian CFD model prediction capabilities and introduce modifications that do not require the film flow assumption. Also, the hydrodynamic model should be extended by considering species balance and coupling particle scale equations. We explore these issues in more depth in Chapter 5.

Chapter 3
Flow Distribution Studies in a High Pressure Trickle Bed Reactor

3.1 Introduction

Flow distribution studies represent an important research area in the investigation of TBRs. Improper liquid distribution reduces the extent of catalyst utilization and for the case of highly exothermic reactions can lead to hot spots and reactor runaway (Jaffe, 1976, Hanika, 1999). Thus, understanding of flow distribution is crucial in order to have optimal performance and stable operation in TBRs.

In general, flow distribution in TBRs is influenced by liquid and gas phases' properties and flow rates, operating pressure, size, shape and orientation of the packing particles in the bed, packing methodology, inlet distributor design, reactor length, column to particle diameter ratio, and liquid-solid wettability (Maiti et al., 2004). The value of liquid flux is the predominant factor in determining the quality of the flow distribution. Flow distribution improves with the increase in liquid superficial velocity. For the lower values of liquid velocity (Herskowitz and Smith, 1978 proposed $L<4$ kg/m^{2}s) liquid channeling is present. In this case often rivulet or filament flow leading to small gas-liquid interfacial area and poor catalyst utilization occurs. With the increase in liquid velocity, the flow

distribution becomes more uniform. Studies performed by Lutran et al., 1991; Ravindra et al., 1997; Saroha et al., 1998b; Toye et al., 1999; Marchot et al., 1999; Marcandelli et al., 2000, and Kundu et al., 2001 have verified this trend by the use of non-invasive flow visualization (Chaouki et al., 1997a, and Boyer et al., 2002) or the collection of effluent liquid fluxes. For the fixed value of liquid velocity, the increase in gas-liquid interactions improves the liquid distribution. The effects of operating pressure and gas velocity have been examined in the studies of Ellman et al., 1988; Ellman et al., 1990; Wammes et al., 1991; Larachi et al., 1991; Ring and Missen, 1991; Larachi et al., 1992; Al-Dahhan and Dudukovic, 1994; Al-Dahhan and Dudukovic, 1995; Al-Dahhan et al., 1998; Harter et al., 2001; Kundu et al., 2002; Kundu et al., 2003b; Iliuta et al., 2005; Boyer et al., 2007, and Aydin and Larachi, 2008. Note that, most commonly, improvement of flow distribution has been identified by the increase in the overall wetting efficiency with the increase in gas velocity or pressure. Also, in some cases the increase in the overall gas-liquid interfacial area and mass transfer have been reported (see the discussion in Al-Dahhan et al., 1997).

Collection of the effluent liquid fluxes is commonly employed in the flow distribution studies (Herskowitz and Smith, 1978; Hoek et al., 1986; Moller et al., 1996; Ravindra et al., 1997; Saroha et al., 1998b; Marcandelli et al., 2000; Kundu et al., 2001; Babu et al., 2007, and Llamas et al., 2008a). The favorable effect of liquid superficial velocity on liquid flow distribution has been verified in these studies, i.e., the effluent liquid fluxes become more uniform with the increase in overall superficial liquid velocity. Overall, the

effluent liquid fluxes become more uniform with the increase in gas velocity. However, for some conditions, the opposite trends (i.e., deterioration of uniformity of liquid distribution with the increase in gas velocity) have been reported. For example, Marcandelli et al., 2000 noticed the increase of maldistribution factor (normalized standard deviation of the values of the effluent liquid fluxes, see equation (3-1) below) with gas velocity in a bed packed with alumina extrudates at the liquid velocities in the range of about 3-5 mm/s. Similar trends have been reported by Llamas et al., 2008b in a bed of alumina extrudates at the liquid velocity of about 8 mm/s.

In this study, we examine the influence of liquid and gas velocity and operating pressure on the flow distribution in a TBR in terms of the two criteria: distribution of the effluent liquid fluxes and cross-sectional liquid holdups. Since each of these criteria gives us a insight into the flow distribution, we are interested not only in their individual trends, but also in their relation to operating conditions.

3.2 Experimental

Figure 3.1 is a schematic of the high pressure trickle bed reactor setup. It is designed to operate at pressures up to 10 barg (~150 psig). It consists of a 16.3 cm inner diameter stainless steel reactor column, gas and liquid delivery system, gas-liquid separator, and effluent fluxes measurement system. The setup enables measurement of the overall liquid holdup and pressure drop, and the distribution of the liquid phase fluxes at the column

outlet. With the aid of gamma-ray CT, the cross-sectional distribution of gas, solid and liquid phase holdups can be obtained at the designated axial positions.

Liquid is stored in a pressurized tank and supplied via a high pressure pump to the distributor at the top of the column. The distributor dispenses liquid uniformly across the top of the bed. The liquid flow rate is controlled using the needle valve and measured using the flow meter placed in the inlet line. After the gas-liquid separation in a bypass separator the liquid is directed back to the tank. The gas flow is regulated using the needle valves located after the gas-liquid separator. The gas flow rate is measured with

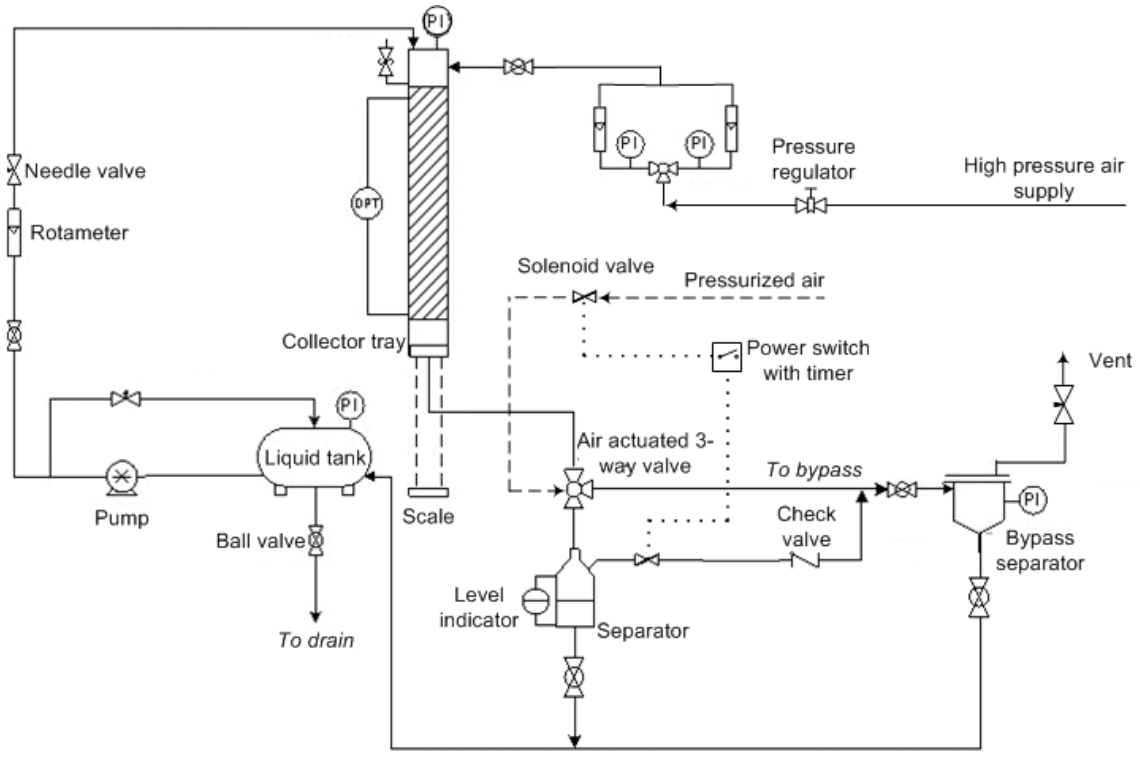

(a)

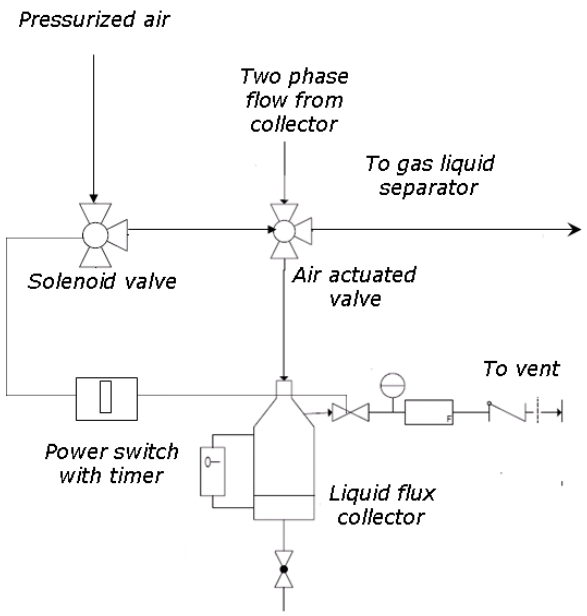

(b)

Figure 3.1 High pressure trickle bed reactor – experimental setup

two flow-meters (high and low range) located in the inlet line. Two Validyne differential pressure transducers, (low range 1.25 psid and high range 5 psid), with pressure taps spaced 50 cm apart, were used for the pressure drop measurements. The column was set on the Arlyn weight scale thus enabling the measurement of the overall liquid holdup using the weighting method.

A collecting system attached to the bottom of the column enables the measurement of the spatially distributed liquid phase effluent fluxes. A collecting tray (Figure 3.2), positioned below the packing support mesh, has 15 compartments each of which is connected to a gas-liquid separator. One such gas-liquid separator is shown in Figure

3.1. During the flux measurements, two phase flow is directed to 15 separators instead into the single bypass separator. Thus, the entire effluent gas-liquid stream is split into 15 streams and then, each of them is directed to its own gas-liquid separator. To achieve this, an air actuated three-way valve is placed above each of the 15 liquid separators. The actuation of the three-way valve is controlled with the normally closed solenoid valve connected to the pressurized air (Figure 3.1-b). The solenoid valve, using power switch with timer, is energized only for a prescribed period of time thus determining collection time. During this time, solenoid valve is open and the pressurized air actuates the air actuated three-way valve. Once actuated, the three-way valve directs the flow into the liquid collectors instead into the main, bypass separator. Once the collection time lapsed, the liquid volume collected in each separator is read of the level indicator. Liquid flow rate at each compartment is calculated as the average value during the collection time.

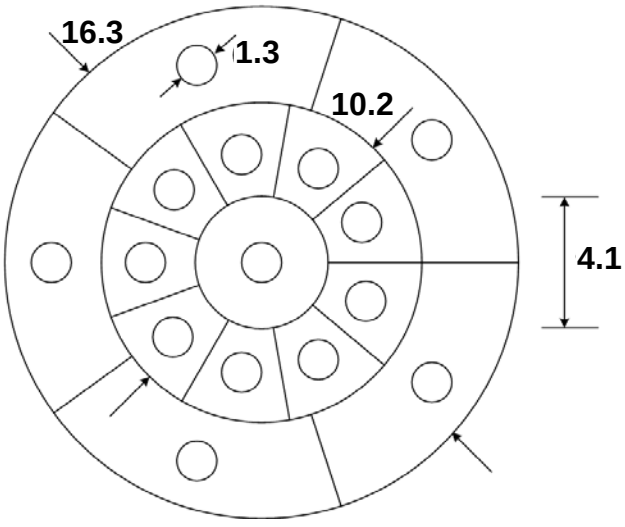

Figure 3.2 Collecting tray (top view). All dimensions are given in centimeters. Each of the 15 compartments is connected to a gas-liquid separator through 0.5” flexible tubing.

Cross-sectional phase holdups are obtained using gamma-ray CT. For this purpose, the reactor column is placed between the gamma-ray source (Cs^{137}) and 11 NaI scintillation detectors. During measurements, the source and the detectors rotate around the column and at each position the attenuation of gamma-rays detected by the 11 detectors is recorded with the aid of data acquisition system connected to a PC. Then, a reconstruction procedure based on the expectation-maximization (EM) algorithm is used to reconstruct the cross-sectional phase holdups. More details on CT hardware, data acquisition system, and reconstruction procedure can be found in Kumar, 1994, and Kumar and Dudukovic, 1997. Principles of EM algorithm are given in Dempster et al., 1977, while the application of the algorithm for the transmission tomography is discussed in Lange and Carson, 1984. Specific procedure for the calculation of phase holdups in a TBR using gamma-ray CT is available in Chen et al., 2001. The operating procedure for the high pressure TBR is given in Appendix B; the details on use of computed tomography unit and EM algorithm are given in Appendix C. Appendix A gives the outline of the procedure for assessment of gamma-ray scanner performance.

Table 3.1 summarizes the experimental conditions. The bed was packed with 1.9 mm porous alumina extrudates (trilobes) to a height of 0.70 m. The resulting average porosity of the bed was 0.39. The fluids used were water and air. CT unit was employed to examine the cross-sectional distribution of porosity and of liquid holdup at three axial positions specified in Table 3.2. In the remainder of the text, we refer to these positions

according to the values given in the second column of Table 3.2, i.e., as the distance from the packing support mesh.

Table 3.1 Experimental setup and operating conditions

Column diameter, m	0.163
Bed height, m	0.70
Fluids used	water and air
Packing	alumina extrudates (trilobes); 1.9 mm equivalent diameter
Bed porosity	0.39
System pressure, barg	0 – 7
Gas velocity, mm/s	30 – 200
Gas mass flux, kg/m^2s	0.036 – 1.68
Liquid velocity, mm/s	1.9 – 9
Liquid hourly space velocity, 1/hr	10 - 46

Table 3.2 CT scan - axial positions

Position	Distance from the packing support mesh, cm	Distance from the top of the packing, cm
Top	65	5.0
Middle	35	35
Bottom	2.5	67.5

The experimental procedure was as follows. The bed was flooded and left overnight to ensure that catalyst particle pores are filled with water. Afterwards, the bed was drained until only static liquid holdup remained and the system was pressurized. Weight scale was zeroed and gas flow initiated and set to the operating value. To minimize the

hysteresis effects on the measurements (see for example Maiti et al., 2006) the Kan-liquid prewetting procedure was used. Thus, first, the liquid flow rate was increased until the pulsing flow regime was reached. Afterwards, the liquid flow rate was set to the operating value. The measurements of liquid holdup (weight scale reading) and pressure drop (differential pressure transducer reading) were performed once the steady state flow conditions have been established. Then, the CT measurements were initiated to collect the values of gamma-ray attenuation. Once the CT scan was done, the timer on the power switch (Figure 3.1-b) was set to the fluxes collection time. After the collection time lapsed, the value of liquid level in each of the 15 liquid collectors was recorded. These values and the collection time were used to calculate average liquid flow rate for each of the 15 compartments of the collecting tray (Figure 3.2).

3.3 Results and discussion

3.3.1 Porosity distribution

Voidage (porosity) distribution of the packed bed was characterized at three axial positions (see Table 3.2) using CT as per the procedure given in Appendix C. The results are presented in Figure 3.3 through Figure 3.5 and in Table 3.3. Figure 3.3 presents the cross-sectional distribution of voidage at the three axial locations examined. Figure 3.4 shows the radial distribution of mean voidage at the three elevations, and Figure 3.5 displays the voidage probability density function at the three elevations. In general, the observed porosity distribution is dependent upon the length scale (resolution) at which the measurements are performed. For the high resolution imaging (Baldwin et al., 1996,

and van der Merwe et al., 2007a), the results can be obtained on the length scale that is significantly lower (e.g., one order of magnitude) than the particle diameter. The pixels in the image contain either gas or solid solely, which overall is represented by bimodal distribution with one peak representing solids and the other representing voids. In our case, the resolution is on the order of couple of particle diameters for which the observed

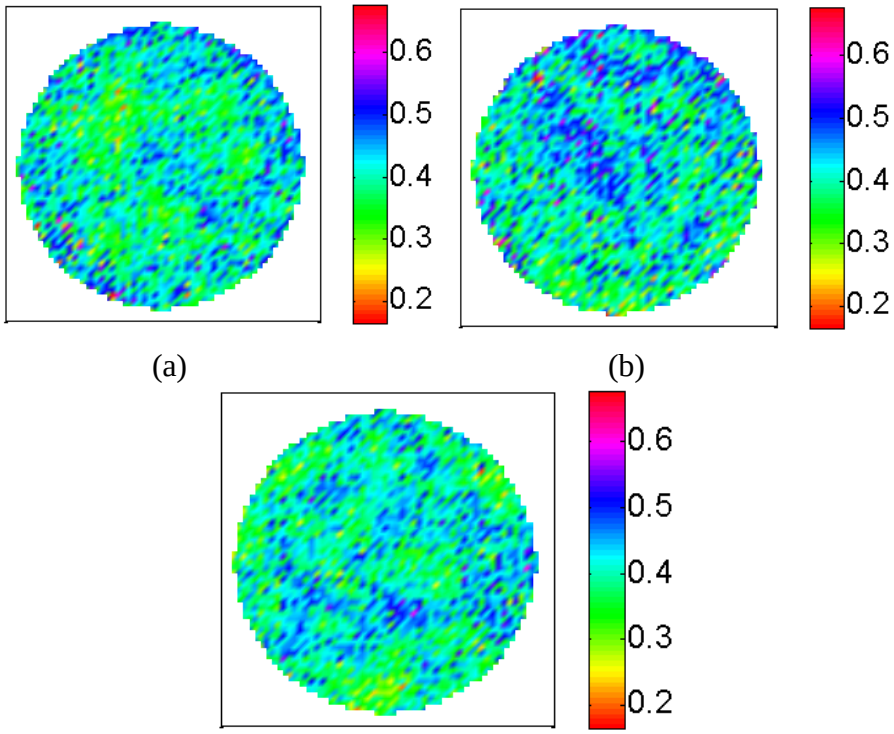

Figure 3.3 Cross sectional porosity map for (a) z = 65, (b) z=35, and (c) z=2.5 cm

porosity distribution resembles a Gaussian one (see the discussion in Jiang et al., 2002b and the experimental study by Baldwin et al., 1996). Figure 3.5 illustrates that the results of this study show the same trend. The results for the standard deviation of porosity in the three cross-sections (Table 3.3) are in agreement with the above mentioned studies. Also,

the results do not indicate a significant dependence of porosity distribution and its parameters on the axial position. Average value of the cross-sectional porosity obtained using CT is in good agreement (deviation < 5%) with the

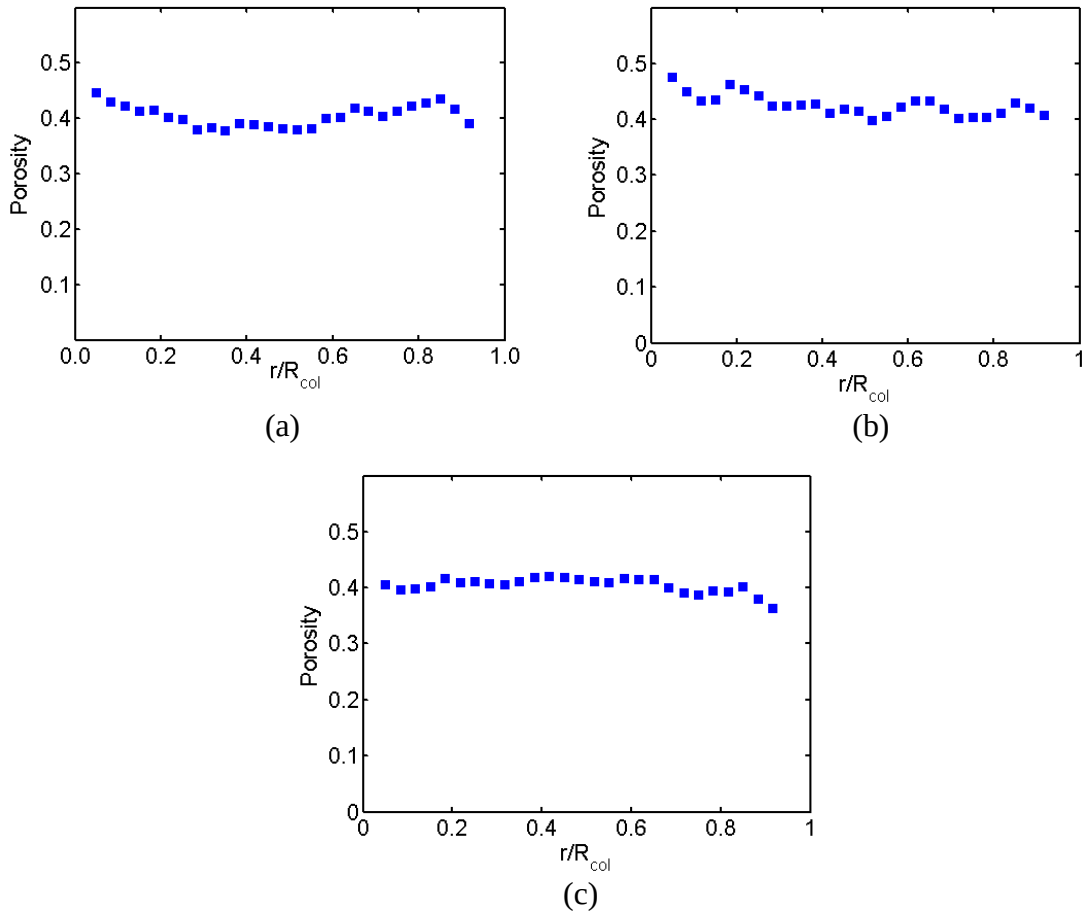

Figure 3.4 Radial profile of porosity for the (a) z = 65, (b) z=35, and (c) z=2.5 cm

overall porosity obtained by the weighting method as shown in Table 3.3.

Table 3.3 Porosity distribution parameters

Position, cm	Average porosity	Standard deviation of porosity on the cross-sectional domain, %	Overall porosity (weight method)
65	0.40	14.8	0.39
35	0.41	16.1	
2.5	0.40	13.9	

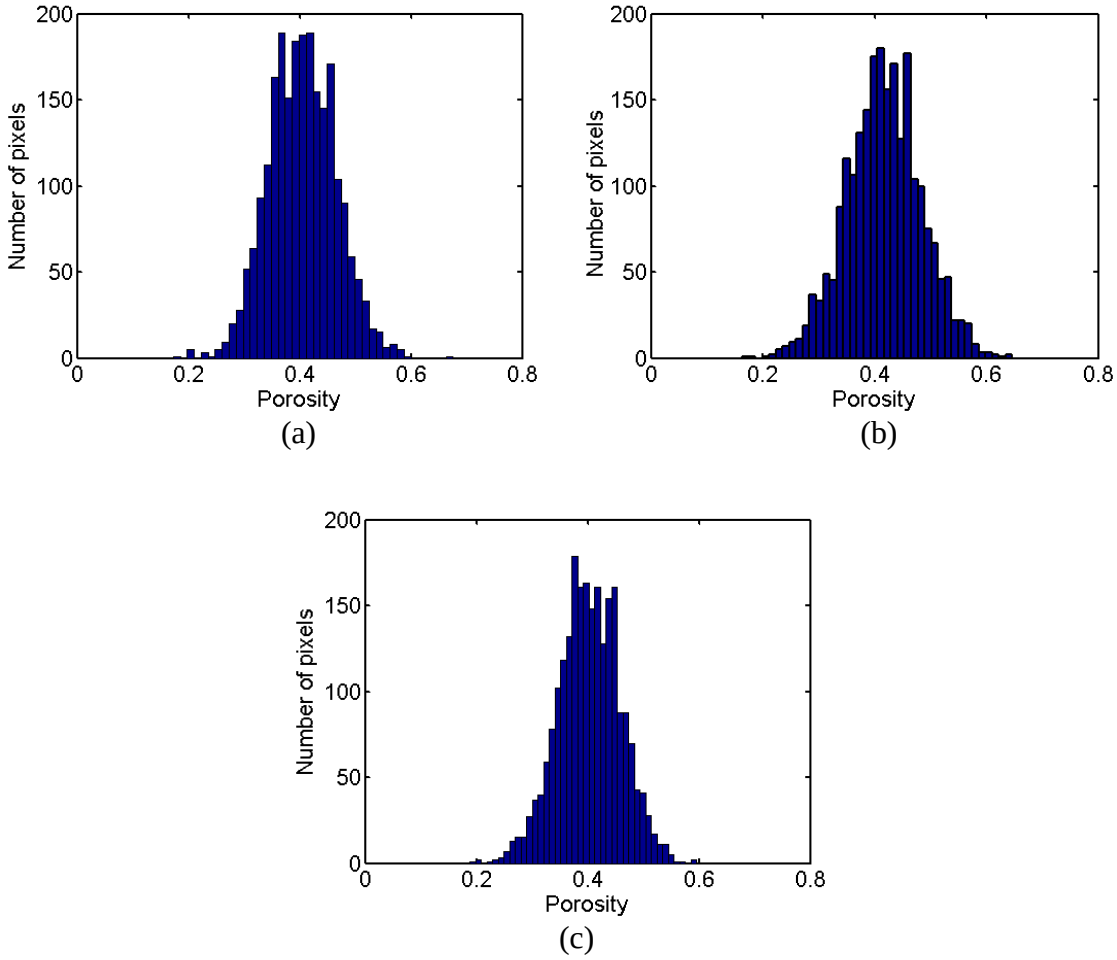

Figure 3.5 Porosity distribution for (a) z = 65, (b) z=35, and (c) z=2.5 cm

3.3.2 Characterization of the flow distribution

In this study, the quality of flow distribution is characterized in terms of the cross-sectional liquid holdup distribution (obtained using CT), and in terms of the liquid phase effluent fluxes distribution (obtained using the collecting system described above).

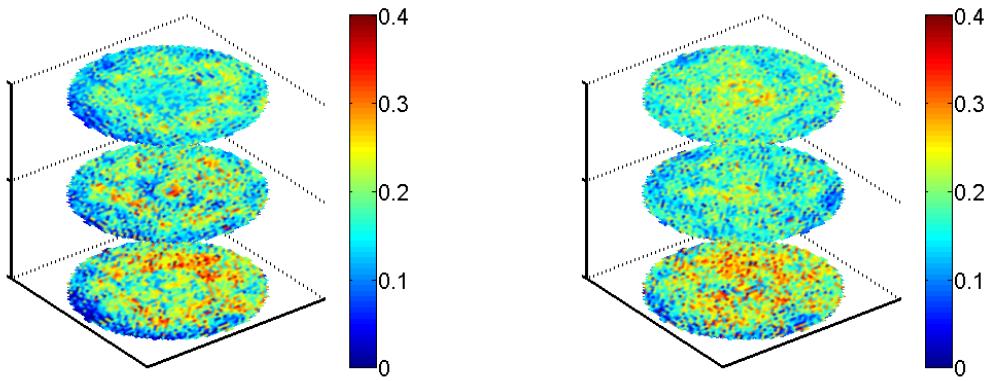

(a) (b)

Figure 3.6 Cross-sectional liquid holdup distribution for the three axial positions (z = 65, z=35, and z=2.5 cm) obtained using CT. (a) P = 2 barg, U_L=3 mm/s, U_G=3 mm/s, (b) P = 7 barg, U_L=9 mm/s, U_G=100 mm/s

Figure 3.6 gives two examples of the cross-sectional liquid holdup map. Figure 3.7 gives the azimuthally averaged radial profile of the liquid holdup for all of the operating conditions considered in the study. As expected, the liquid holdup increases with the increase in liquid superficial velocity, and decreases with the increase in gas superficial velocity or operating pressure. Also, the liquid holdup radial profile becomes more uniform with the increase in liquid velocity (Figure 3.7).

The liquid phase effluent fluxes distribution can be characterized in terms of the percentage of the total mass flow (Figure 3.8) in each of the 15 compartments of the collecting tray. The effluent fluxes distribution becomes more uniform with the increase in liquid superficial velocity (cf. Figure 3.8-a and Figure 3.8-b, and Figure 3.8-c and Figure 3.8-d). The effect of the other operating parameters is not easily deduced from these images or the values of the mass fluxes in general. To ease the analysis, it is preferable to have a lumped numerical value that characterizes the degree of uniformity of flow

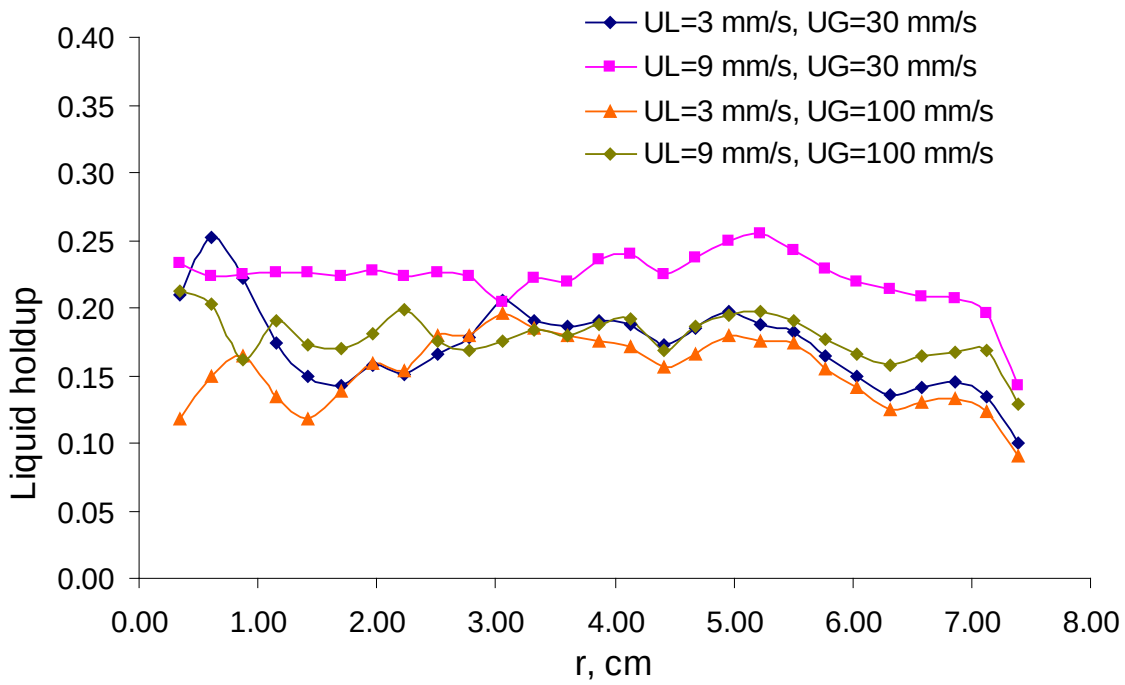

(a)

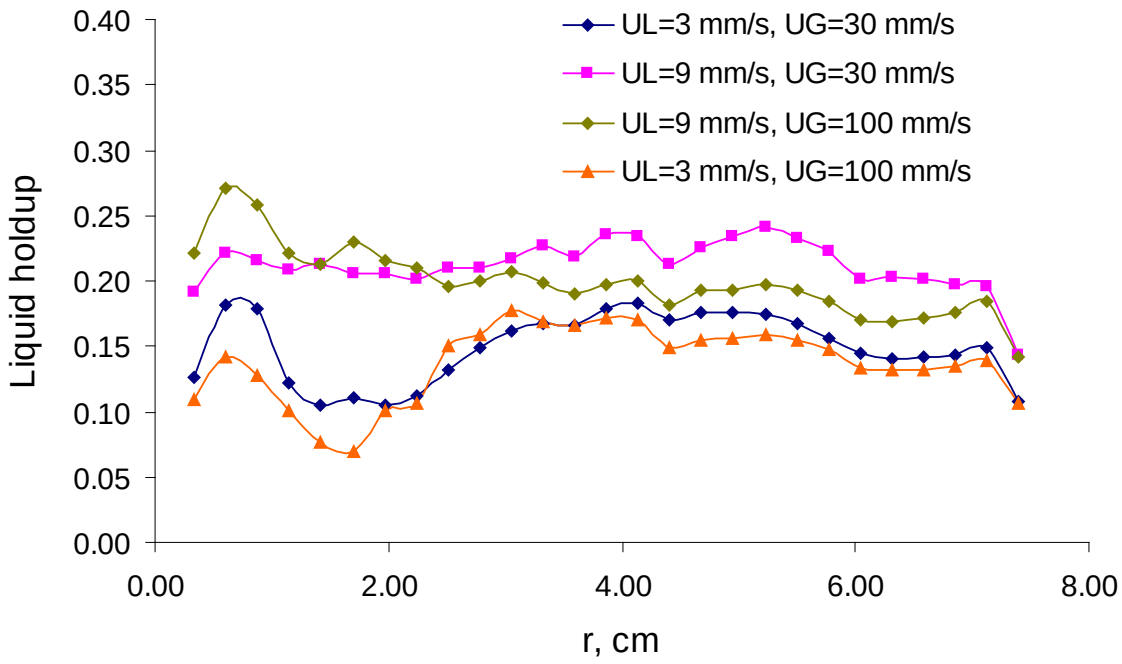

(b)

Figure 3.7 Radial profile of liquid holdup at z=35 cm. (a) P=2 barg, (b) P=7 barg

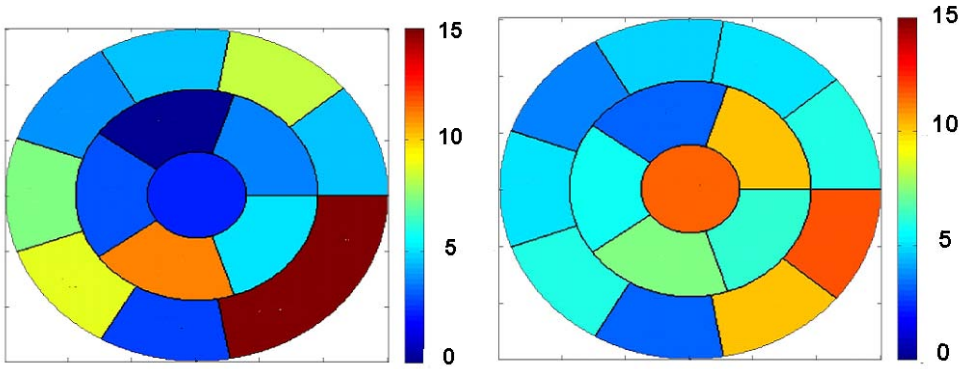

(a) (b)

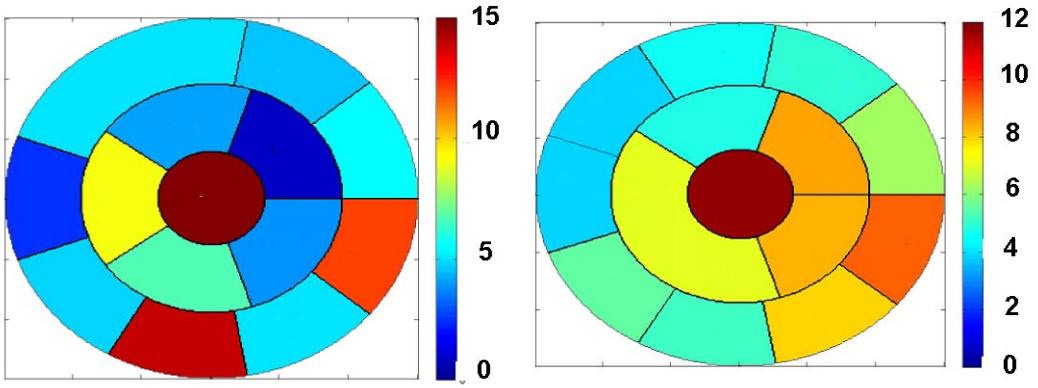

(c) (d)

Figure 3.8 Effluent liquid fluxes distribution: percentage of total mass flow in each of the 15 compartments: (a) P = 2 barg, U_L = 3 mm/s, U_G = 30 mm/s; (b) P = 2 barg, U_L = 9 mm/s, U_G = 30 mm/s, (c) P = 7 barg, U_L = 3 mm/s, U_G = 110 mm/s, (d) P = 7 barg, U_L = 9 mm/s, U_G = 110 mm/s. Colorbars represent the percentage of total mass flow in each of the 15 compartments (i.e, (kg/s in compartment *i*)/(kg/s total effluent)*100%)

distribution. Here we use the maldistribution factor proposed by Marcandelli et al., 2000, given by equation (3-1). The maldistribution factor represents the value of standard

$$M_f = \sqrt{\frac{1}{N(N-1)}\sum_{i=1}^{N}\left(\frac{FLUX_i - \overline{FLUX}}{\overline{FLUX}}\right)^2} \qquad (3\text{-}1)$$

deviation of fluxes ($FLUX_i$) normalized by the average value of flux ($\overline{FLUX}$) and the number of compartments in the collecting tray (N=15). Hence, M_f takes values from zero (ideal, uniform distribution) to one (all the liquid goes to one compartment, i.e., fully maldistributed flow). The results for the maldistribution factor are given in Figure 3.9. Note that the data within one chart are grouped in terms of liquid superficial velocity. For

example, in Figure 3.9-a, both bars on the left hand side are for the U_L=3 mm/s; the bars on the right hand side are both for U_L=9 mm/s.

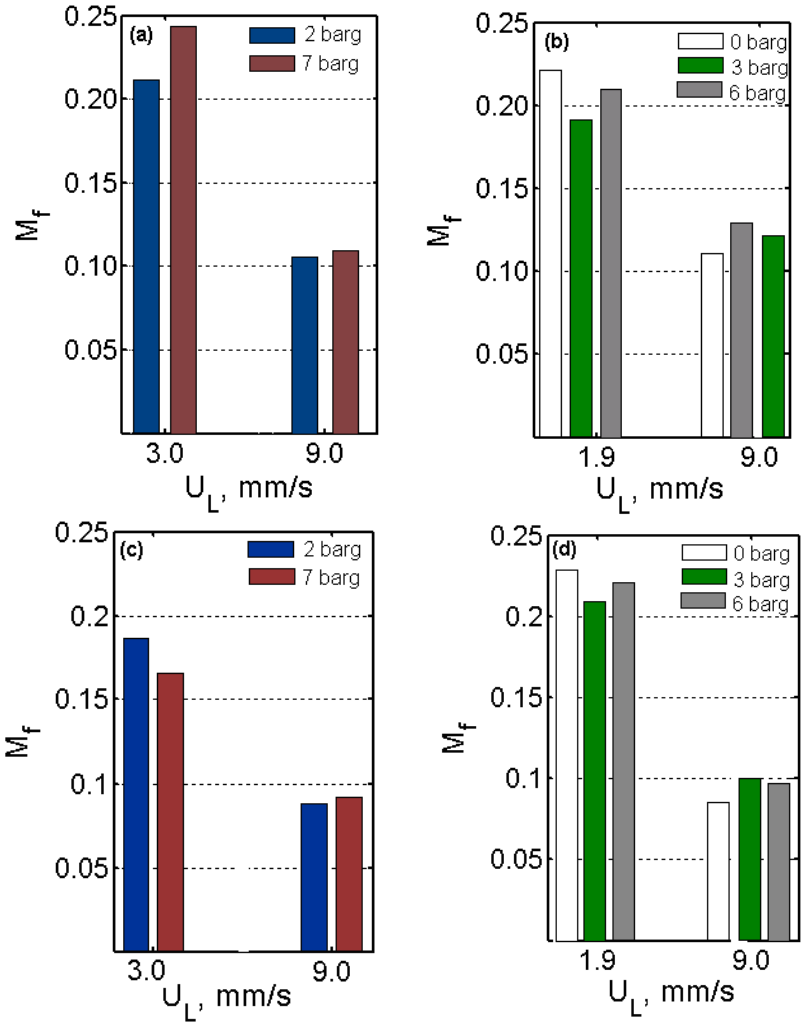

Figure 3.9 Maldistribution factor for effluent liquid fluxes: (a) U_G = 30 mm/s, (b) U_G = 60 mm/s, (c) U_G = 100 mm/s, and (d) U_G = 200 mm/s

Similarly to the maldistribution factor of effluent liquid fluxes, the maldistribution factors for the cross-sectional liquid holdup at the axial position z=2.5 cm (just above the

collector tray) have been calculated. The comparison of scaled factors, defined in equation (3-2), is given in Figure 3.10. The scaling is performed to ease the graphical

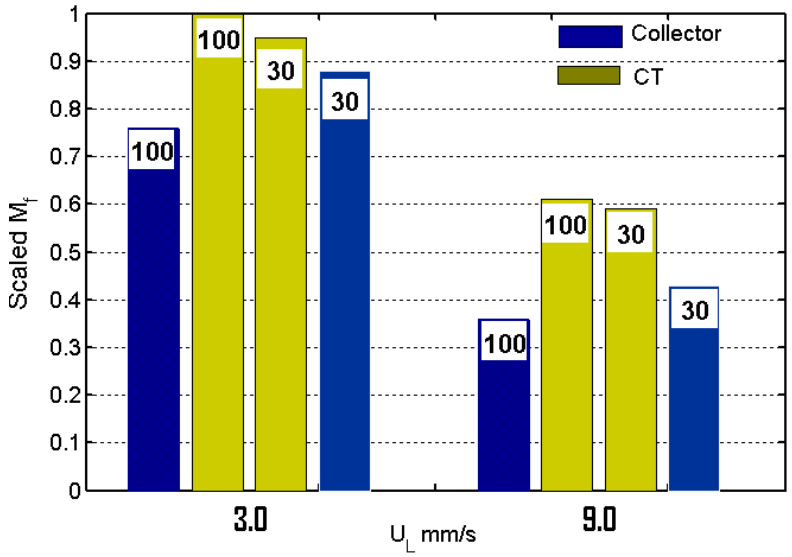

(a)

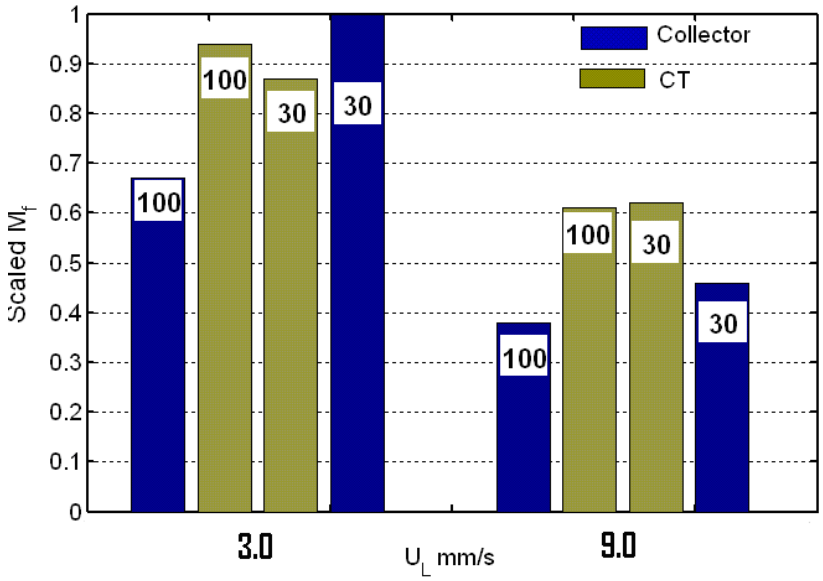

(b)

Figure 3.10 Scaled Mf factors for liquid holdup (z=2.5 cm) and effluent fluxes. Numbers indicate gas velocity in mm/s. (a) P = 2 barg, (b) P = 7 barg

representation since the absolute values of factors for effluent fluxes are about five times higher than the ones for holdups. The comparison of the trends of the two maldistribution factors is given in Table 3.4.

$$\left(M_{f,i}\right)_{scaled} = \frac{M_{f,i}}{\max\{M_{f,i}\}} \tag{3-2}$$

Table 3.4 Trends in the maldistribution factors defined based on liquid holdup and effluent fluxes

Operating parameter	Other operating parameters	Trend in maldistribution factor data based on:		Expected based on HP TBR studies
		Effluent fluxes	Liquid holdup	
Increase in U_L	All conditions	Decreases	Decreases	Decrease
Increase in U_G for P=const.	Low U_L	Decreases	Increases	Decrease
	High U_L	Decreases	Decreases	Decrease
Increase in pressure	All conditions	Overall, no particular trend	Decreases	Decrease

The last column in Table 3.4 represents the expectations for liquid maldistribution which are obtained *indirectly* based on the extensive high pressure TBR investigations of the wetting efficiency, liquid holdup and pressure drop and their assumed relation to the quality of liquid distribution. These results serve as a basis for the general statement that the flow distribution improves with the increase in pressure, and gas and liquid superficial velocity. However, the actual confirmation of this statement for the quantities examined in this study (liquid holdup and effluent fluxes maldistribution factors) is still under experimental investigation. Both liquid holdup and effluent fluxes maldistribution factors decrease with the increased value of liquid superficial velocity and hence indicate the improvement of flow distribution at conditions of increased liquid velocity (see similar results in the studies by Marcandelli et al., 2000, Kundu et al., 2001, Llamas et al., 2008a). For the higher value of liquid velocity, both factors decrease with the increase in

gas velocity. Also, liquid holdup based maldistribution factor decreases with the increase in pressure. However, there are two definite deviations of the trends of maldistribution factors from the ones inferred based on previous HP TBR investigations.

First, the effluent fluxes maldistribution factor does not exhibit any particular trend with respect to the operating pressure. This perhaps be attributed to the span of values of operating pressure used in this study. Typically, HP TBR investigations have about 30-70 fold increase in operating pressure (see the detailed review of high pressure investigation in Al-Dahhan et al., 1997). Here, due to the large scale of TBR used in this study and other considerations we are limited to the maximum of about ten fold increase in operating pressure. Hence, we do not see systematic variations of the effluent fluxes M_f factor with the change of pressure over that relatively small range of pressures (Figure 3.9).

Second, the liquid holdup based maldistribution factor *increases* with the increase in gas superficial velocity for the conditions of low liquid superficial velocity while the effluent fluxes maldistribution factor exhibits the opposite trend and decreases indicating a more uniform liquid distribution with increase in superficial gas velocity. At the same time, as shown in Figure 3.11, the overall liquid holdup decreases with the increase in gas superficial velocity as observed in HP TBR studies listed above. This implies that, for the lower liquid velocities, increased gas velocity, through higher gas-liquid interactions,

lowers the overall volume of liquid present in the bed and redistributes the liquid in a less

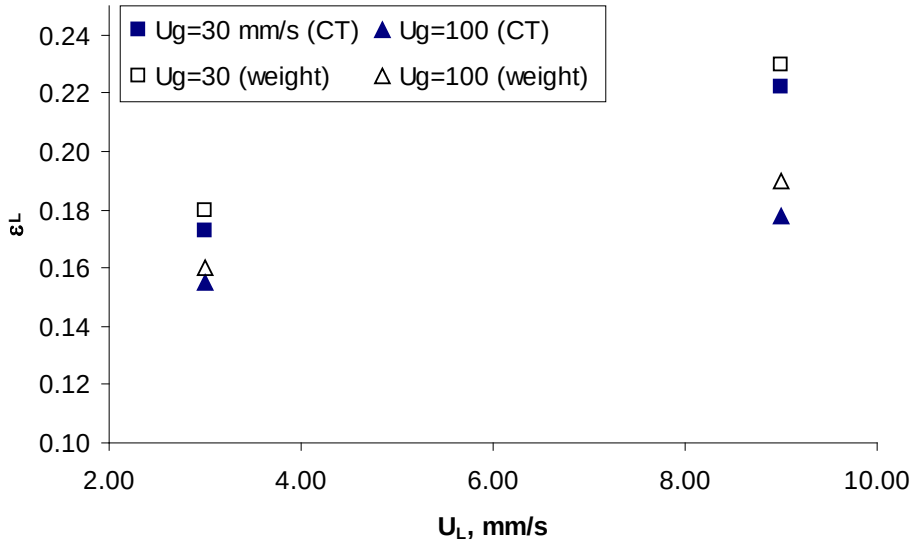

(a)

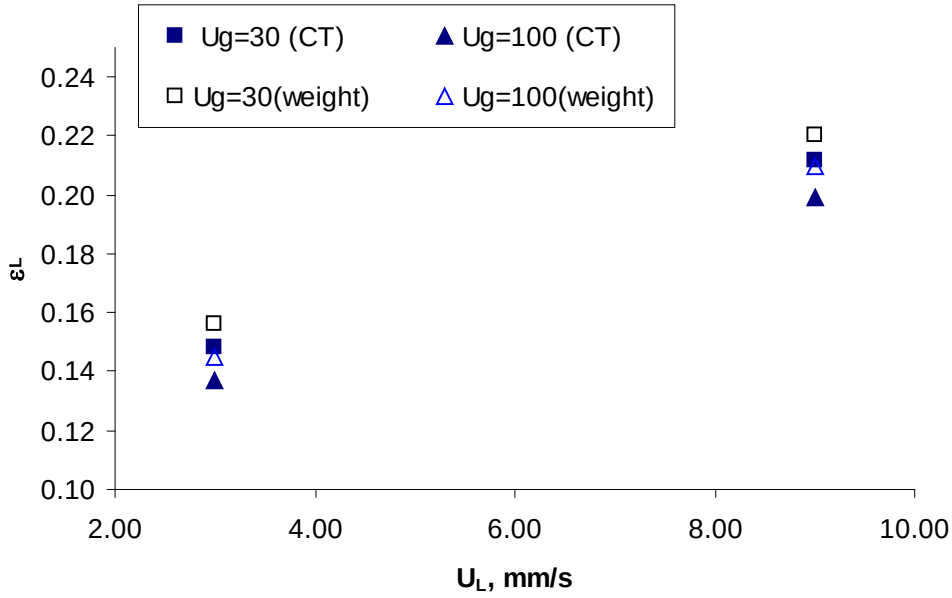

(b)

Figure 3.11 Overall liquid holdup obtained by the weighting method and cross-sectional average liquid holdup obtained by CT at z=35 cm. (a) P=2 barg, (b) P=7 barg

$$\frac{(M_f)_{Fluxes}}{\sqrt{N(N-1)}} = \sqrt{\left(\frac{\int_{Compartment} \varepsilon_L u_L \rho_L dA_{Compartment} / \int_{Compartment} dA_{Compartment} - \int_{Column} \varepsilon_L u_L \rho_L dA_{Column} / \int_{Column} dA_{Column}}{\int_{Column} \varepsilon_L u_L \rho_L dA_{Column} / \int_{Column} dA_{Column}} \right)^2} \quad (3\text{-}3)$$

uniform way. Interestingly, at the same time, the liquid flow distribution becomes more uniform in terms of the liquid flow rate in each compartment (Table 3.4, Figure 3.10). In principle, the two maldistribution factors used in this study can be related as shown in equation (3-3). If the results for the liquid holdup had been available at the same resolution as for the liquid holdup, we could have calculated the corresponding liquid physical velocities (u_L) in each pixel on the domain. This would establish the correlation between liquid velocities and holdups and could lead to an explanation of the observed trends. However, the resolution at which the fluxes data have been obtained (i.e, only 15 sections compared to about 2000 sections for liquid holdup measurements) is not high enough to numerically solve integrals in equation (3-3) and obtain the liquid velocities. In a recent study, Llamas et al., 2008b, applied the wire mesh tomography and liquid collectors to examine the quality of liquid flow distribution in a TBR packed with alumina extrudates. Some of their results for maldistribution factors based on liquid holdup and effluent fluxes exhibit the same trend (namely, increase in M_f based on liquid holdups and decrease in M_f based on liquid effluent fluxes with the increase in gas velocity) which confirms the results obtained in this study. The authors attributed the observed trends to the existence of the high and low liquid holdup zones in the reactor.

In the regions of low liquid holdup there is less resistance to gas flow and hence these regions will have higher gas velocity. The opposite holds for the regions of higher liquid holdup. Hence, lower liquid holdup regions tend to exhibit higher liquid velocity induced by the gas shear. Using similar reasoning, higher holdup regions tend to exhibit lower liquid velocity. Using the definition of mass flux or equation (3-3), the opposite trends in the maldistribution factors defined based on liquid holdup and effluent fluxes can be reconciled. At this moment, only MRI studies can provide all the data needed for full experimental evaluation of this phenomenon.

3.4 Summary

The flow distribution in a high pressure TBR has been investigated in terms of the distribution of cross-sectional liquid holdup and liquid phase effluent fluxes. Based on the general literature concerning high pressure trickle bed reactors it was expected that both liquid holdup and effluent liquid fluxes would become more uniform with the increase in pressure, and gas or liquid velocity. The anticipated results have been fully obtained only for the effect concerning liquid velocity. No pronounced trend was observed with respect to operating pressure which can be attributed to lower span of operating pressures used in this study as compared with typical high pressure TBR studies. A somewhat puzzling result has been obtained for the effect of increase in gas velocity in the region of lower liquid velocities. The results indicate improvement in the effluent fluxes distribution and deterioration in the cross-sectional holdup distribution with the increase in gas velocity. A unified experimental study in which holdups and

velocity data can be obtained (such as MRI imaging) is needed to reveal the causes of such results and enable their full quantification.

Chapter 4
Effect of Operating Conditions on the Extent of Hysteresis in a High Pressure Trickle Bed Reactor

4.1 Introduction

Among the basic design and operating parameters for trickle beds are pressure drop and liquid phase holdup. These parameters are not only very dependent on the operating conditions, such as flow rates and bed characteristics, but also exhibit dependence on the flow history of the bed. This is termed *hysteresis* or *the multiplicity of hydrodynamic states* in trickle beds. In the landmark study by Kan and Greenfield, 1978, the gas flow rate, at a fixed liquid velocity, was gradually increased between zero and the prescribed maximum value and then decreased back to zero. At each condition a steady state was established and pressure drop measured. The measured pressure drop was higher for the branch formed by increasing gas velocity (the upper branch) than the corresponding values in the branch formed by decreasing gas velocity (the lower branch). Based on this and similar studies (Christensen et al., 1986; Levec et al., 1988; Lutran et al., 1991; Ravindra et al., 1997; Gunjal et al., 2005a; Maiti et al., 2005; see also Maiti et al., 2006 and references therein), it became evident that the extent of hysteresis depends on the packing size, particle characteristics (e.g., whether the particles are porous), and fluid

properties (such as surface tension). The existence of hysteresis has been attributed to the fact that predominant flow structures, for example, film flow or rivulet flow, are different for the upper and lower branches (Christensen et al., 1986, and Lutran et al., 1991). The flow structure determines the extent of the interaction between the phases and thus each leads to distinct values of hydrodynamic parameters, such as the pressure drop and liquid holdup.

In the studies performed by Ellman et al., 1988; Wammes et al., 1991; Larachi et al., 1991; Al-Dahhan and Dudukovic, 1994; Nemec and Levec, 2005; Highfill and Al-Dahhan, 2001, and Iliuta et al., 2005, it was shown that increased operating pressure alters the phase interactions, hydrodynamic parameters, and flow regime transition. However, there seems to be no study in the literature performed to examine the effect of the operating pressure on the extent of hysteresis in TBRs, even though, typically, industrial trickle beds operate at elevated pressure (Al-Dahhan et al., 1997). As mentioned earlier, operating pressure affects the phase interactions and wetting efficiency, and hence the flow pattern. Thus, it is expected that pressure will affect the extent of hysteresis as well. Therefore, the focus of this part of study is to experimentally examine the effect of elevated pressure on the extent of hysteresis of pressure drop in a TBR.

In this work, different flow histories were achieved in two ways: by looping (by this we mean increasing from lower bound to upper bound followed by a decrease) the liquid

velocity for a fixed gas velocity and operating pressure, and by setting different initial states of the bed using four prewetting modes summarized by van der Merwe and Nicol, 2005, and Loudon et al., 2006. In both procedures the intention is to bring the system into the same operating conditions, with the only distinction being the flow history, and to quantify the resulting difference in the pressure drop.

In the studies by van der Merwe and Nicol, 2005, and Loudon et al., 2006, the observed pressure drop and liquid holdup were recorded as a function of the applied prewetting mode for a nitrogen-water-3 mm glass beads system at atmospheric conditions. Five cases of prewetting were considered. The authors name them as: 1) a non prewetted bed, 2) Levec prewetted bed, 3) Kan-liquid prewetted bed, 4) Kan-gas prewetted bed, and 5) Super prewetted bed for which we shall use the name Nicol prewetted bed. In the Levec mode, the bed is flooded and the liquid is then allowed to drain under gravity. After that, gas and liquid flows are initiated. In the Kan-liquid mode, the gas velocity is kept at the operating value while the liquid velocity is increased in order to reach the pulsing regime and is then reduced to the operating value. In the Kan-gas mode, the liquid velocity is kept at the operating value and the gas velocity is varied to achieve pulsing and then is adjusted to the operating value. The Nicol prewetted bed is achieved by first flooding the bed and then draining it *without* interruption of liquid flow. During this process, the liquid velocity is kept at the operating value, and gas flow is initiated after drainage is complete. Significant differences in the values of pressure drop and liquid holdup were found among the cases described above. A non-prewetted bed invariably exhibited the

lowest pressure drop and liquid holdup. The Nicol and Kan-liquid modes had the highest values of pressure drop, while the Kan-gas mode had the highest values of liquid holdup. Among the prewetted beds, the Levec mode always had the lowest pressure drop and liquid holdup. The authors attributed the higher values of pressure drop and liquid holdup to film flow and the lower values to rivulet flow. A very interesting result obtained in these studies is that the Kan-gas mode had intermediate values of pressure drop while at the same time exhibited the highest corresponding liquid holdup. The authors attributed this to the fact that the flow textures are a combination of film and rivulet flow, and that their interplay with the effect of tortuosity of the path is such that pressure drop is reduced without affecting the resulting liquid holdup.

The four cases of prewetting mentioned above have been examined in this study at varying operating pressures up to 8 barg. To avoid repacking the bed, which changes the bed structure, the non-prewetted mode was not studied here.

The effect of the increased pressure on the extent of hysteresis can be described using the phenomenological analysis proposed by Al-Dahhan and Dudukovic, 1994. These authors introduced five limiting cases that are determined by the values of operating pressure and gas velocity. Their effect on the hydrodynamic parameters, such as pressure drop, liquid holdup, catalyst wetting efficiency, and gas-liquid interfacial area was examined. Limiting cases are interpreted in terms of the dimensionless pressure drop

defined as $(\Delta P/L)/\rho_L g$. The analysis of Al-Dahhan and Dudukovic, 1994 is summarized next.

Case 1: No gas flow, all pressures. The dimensionless pressure gradient $(\Delta P/L)/\rho_L g$ is zero and the liquid flow is driven by gravity only. The system is characterized by the largest value of liquid holdup for a given liquid velocity. Due to poor spreading of the liquid it also exhibits the smallest values of catalyst wetting efficiency and gas-liquid interfacial area at given liquid velocity.

Case 2: Low pressure and low gas superficial velocity. The dimensionless pressure drop is small and its change with gas velocity can be neglected. Hence, the liquid flow is gravity driven and to a large extent gas independent, i.e., it does not depend on the operating pressure and gas flow rate.

Case 3: Low pressure and high superficial gas velocity. In this case, for a fixed gravitational force, i.e., given liquid density, the pressure gradient increases with increased gas velocity, and as a consequence the dimensionless pressure gradient increases as well. A decrease in liquid holdup and an increase in the catalyst wetting efficiency and gas-liquid interfacial area at given liquid velocity is observed at increased pressure drop. This is the result of the increased spreading of liquid on both the macro level (across the reactor) and micro level (over the external area of the packing particle) due to higher gas flow rate.

Case 4: High pressure and low gas superficial velocity. The pressure drop and dimensionless pressure gradient at a given gas velocity are now larger due to the higher gas density. The resulting effect is similar to Case 3, but less pronounced since the pressure gradient is more sensitive to velocity changes than to gas density changes.

Case 5: High pressure and high gas superficial velocity. In this case, gas-liquid interactions are the most pronounced. Shear stress on the gas-liquid interface increases significantly, and due to this, liquid holdup decreases while catalyst wetting efficiency and gas-liquid interfacial area increase. This effect is more pronounced at higher liquid flow rates than at low flow rates.

This analysis is now extended to interpret the effect of elevated pressure on the extent of hysteresis.

4.2 Experimental Setup and Conditions

The description of the high pressure trickle bed experimental setup (Figure 4.1) is given in Chapter 3.2 and Appendix B. The details of the standard operating procedure are given in Appendix B.

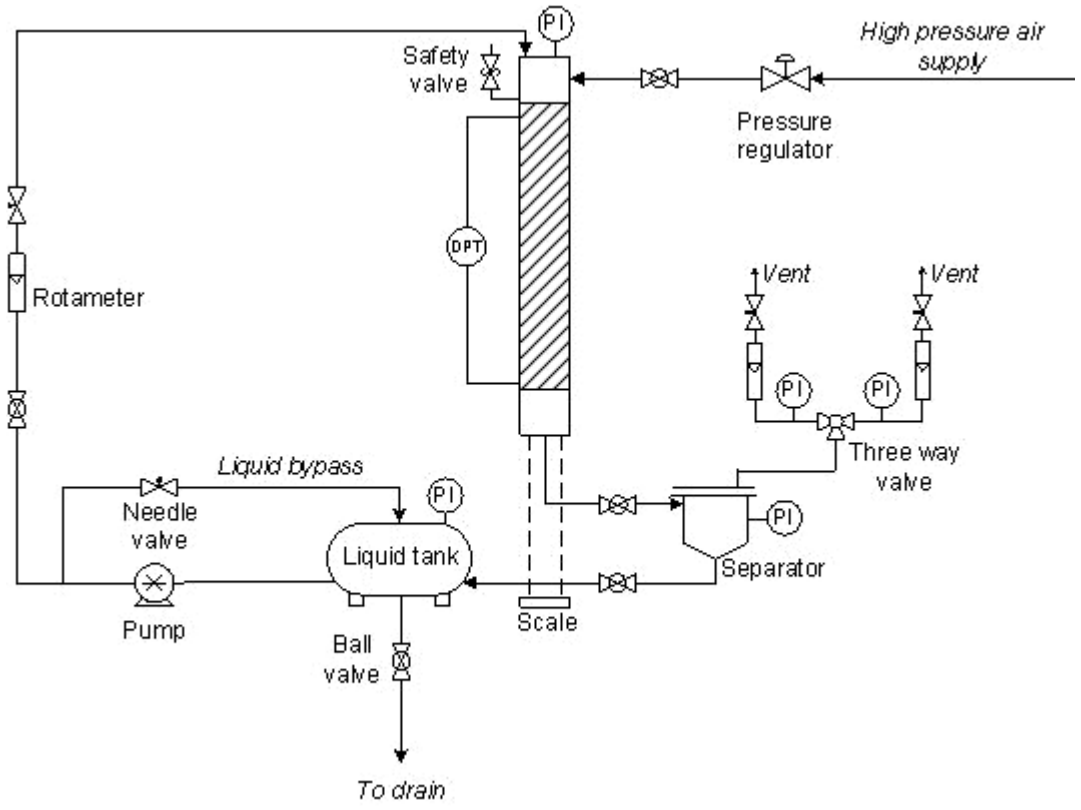

Figure 4.1 High pressure trickle bed reactor - experimental setup

The experimental work consisted of two parts: 1) setting the different initial state of the bed using on of the four prewetting modes, and 2) 'looping' the liquid velocity (i.e. increasing gradually the liquid velocity from a preset minimum to a maximum value and measuring pressure drop at each steady state and then reducing the liquid velocity over the same range of values) for a fixed gas velocity and operating pressure. Both procedures enabled us to investigate the effect of flow history on the pressure drop and the extent of its hysteresis.

Table 4.1 summarizes the experimental conditions. The bed was packed with 3 mm glass beads to a height of 0.68 m. The resulting average porosity of the bed was 0.41. The fluids used were water and air. The experiments covered five operating pressures (1, 2, 4, 6 and 8 barg). The gas (air) density at these pressures is in the range 1 to 8 kg/m^3, and therefore corresponds to typical hydrogen gas densities at industrial conditions used in commercial hydrogenation units where pressures and temperatures are typically in the range 1 to 20 MPa and 300 to 400 ^{0}C, respectively (Kundu et al., 2003a). As shown in Al-Dahhan et al., 1997 the hydrodynamics of high pressure units with hydrogen can be simulated in lower pressure units provided that the gas densities are matched. The present results are therefore applicable to industrially relevant cases. Since the case of the non-

Table 4.1 Experimental setup and operating conditions

Column diameter, m	0.163
Bed height, m	0.68
Fluids used	water and air
Packing	glass beads, 3 mm diameter
Bed porosity	0.41
System pressure, barg	1 – 8
Gas velocity, mm/s	27 – 94
Liquid velocity, mm/s	1.9 – 9.5
Pre-wetting modes considered	Levec, Kan-gas, Kan-liquid, Nicol

prewetted bed was not considered in this study, it was possible to examine all of the above conditions without any need for repacking the column. Thus, the results obtained are not affected by a change in the overall porosity or the structure of the bed. The

experimental procedure was as follows. In the Nicol prewetting mode, the bed was first pre-wetted and drained until only residual holdup remained. The pressure was increased to the operating value. Then, liquid flow was set to the appropriate value for the current experiment, and bed was flooded by closing the outlet valve. Once the bed was flooded, the outlet valve was opened, allowing liquid to drain while keeping the liquid flow on. After the bed drained fully, the gas flow was initiated. Pressure drop was recorded once the steady state was reached. In the Levec prewetting mode, the bed was flooded, liquid flow was shut off, and the bed was drained. Then, the gas flow was initiated. Ten minutes later, liquid flow was set to the operating value and, after steady state was reached, measurements were taken. The Kan-liquid and Kan-gas procedures were obtained by reaching the pulsing regime by increasing the liquid and gas phase flow rates, respectively, and then setting them to the operating values.

For each of the experimental conditions the order in which the modes were used was invariably: Nicol, Levec, Kan-liquid and Kan-gas. Separately, it was verified that the order in which the modes are applied does not affect the resulting pressure drop gradient or the extent of hysteresis. This was confirmed by varying the sequence for a couple of sets of experimental conditions. Thus, all the results are to be attributed purely to the modes used and not to the sequence in which they are applied.

In each of the ‘looping’ experiments, the bed was first flooded and then drained until only static holdup remained. Thus, Levec prewetting mode was used. Then, for a fixed

operating pressure (1 or 8 barg) and gas velocity (27 or 94 mm/s), liquid velocity was looped from 1.9 to 9.5 mm/s (which is short of the pulsing velocity) and back. The pressure drop was recorded for each of the liquid velocities.

4.3 Results and Discussion

The results for pressure drop, based on the looping liquid velocity experiments, are given in Figure 4.2. The data points group into two distinct branches: one formed by increasing liquid velocity (”lower branch”) and one formed by decreasing liquid velocity (“upper branch”). The pressure drop is always higher for the case of decreasing liquid velocity and is also always higher for the case of higher operating pressure. Hysteresis is present irrespective of the operating pressure or gas velocity. In the lower branch liquid spreads across a progressively higher area of the column. Some of the liquid films that were developed in this process remained irrigated in the upper branch (Maiti et al., 2005). The enhanced spreading led to a higher pressure drop. The generalization of this interpretation is that the hysteresis is a phenomenon caused by a change in the predominant flow pattern during the hysteresis loop (Christensen et al., 1986, Lutran et al., 1991, Wang et al., 1995). In the lower branch, liquid flows predominantly in the form of filaments (Figure 4.3). With and increase of liquid velocity, the filaments enlarged and merged, creating predominantly film flow. Once the liquid flow rate was decreased, predominant flow patterns were again filaments, but with the larger contribution coming from film flow. Similar analysis was used by Wang et al., 1995, to

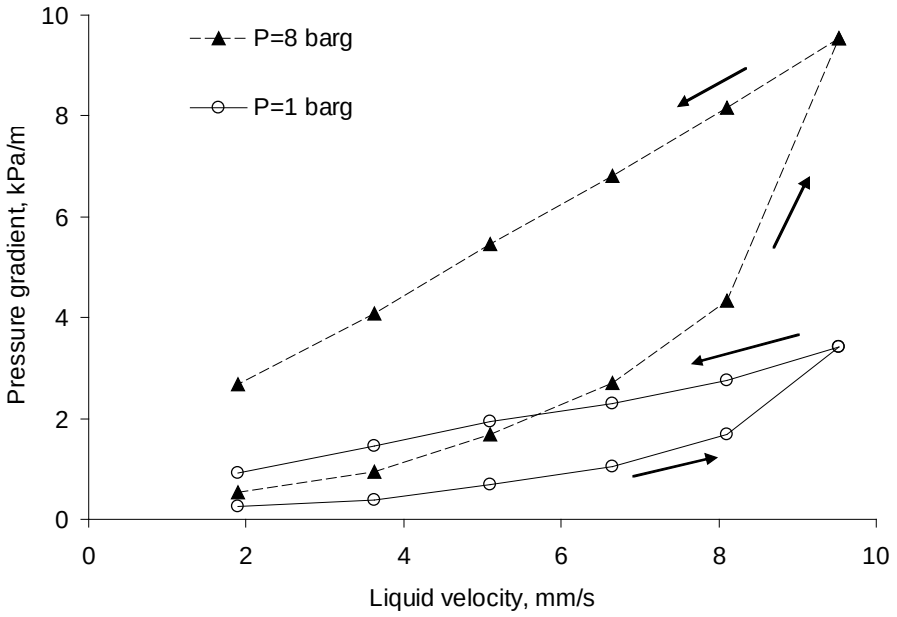

(a)

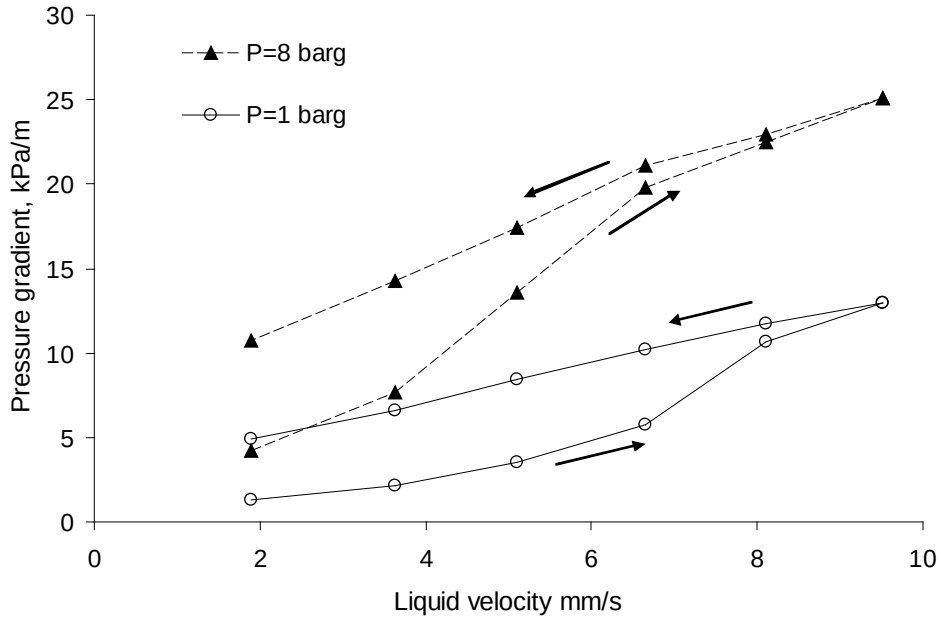

(b)

Figure 4.2 Hysteresis loops: (a) U_G=27 *mm/s* (b) U_G=90 *mm/s*

develop a model capable of conceptually quantifying the extents of film and rivulet flow. In their model, fitting parameters are used to assign areas of reactors associated with film and filament flow in the lower branch. In Figure 4.4 - Figure 4.6, the pressure drop is given as a function of the applied prewetting mode. The data indicate existence of hysteresis for the high pressure system under investigation. Pressure drop is the highest for the Nicol and Kan-liquid pre-wetting modes, while the Levec mode tends to exhibit lower values.

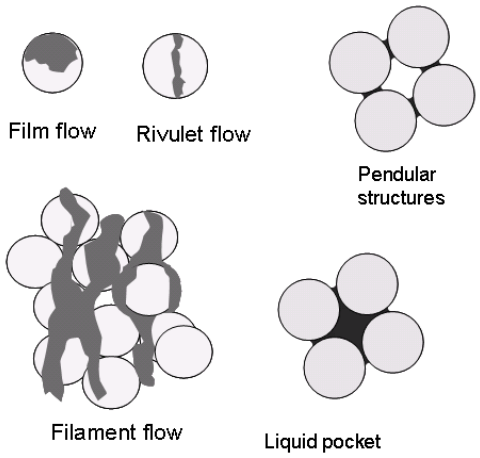

Figure 4.3 Trickle flow patterns (adapted from Lutran et al., 1991)

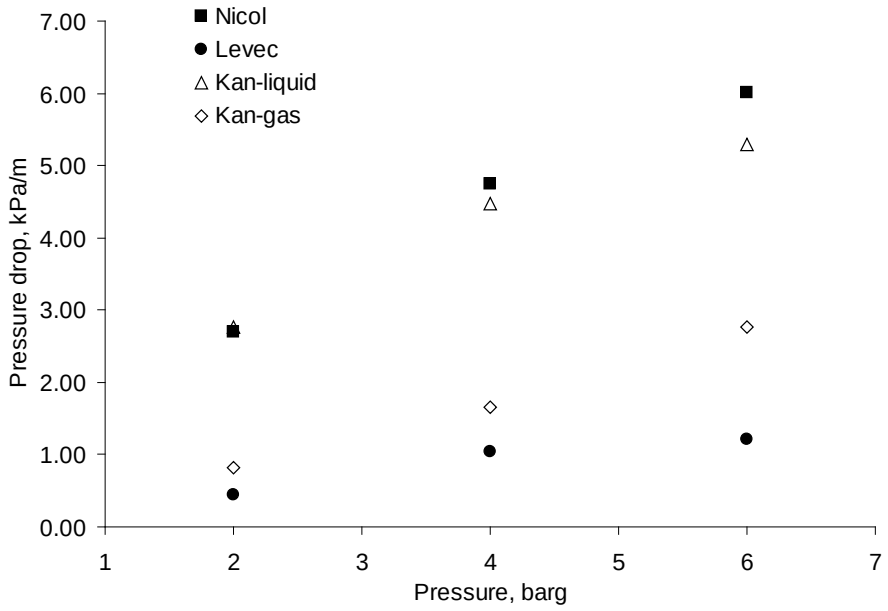

(a)

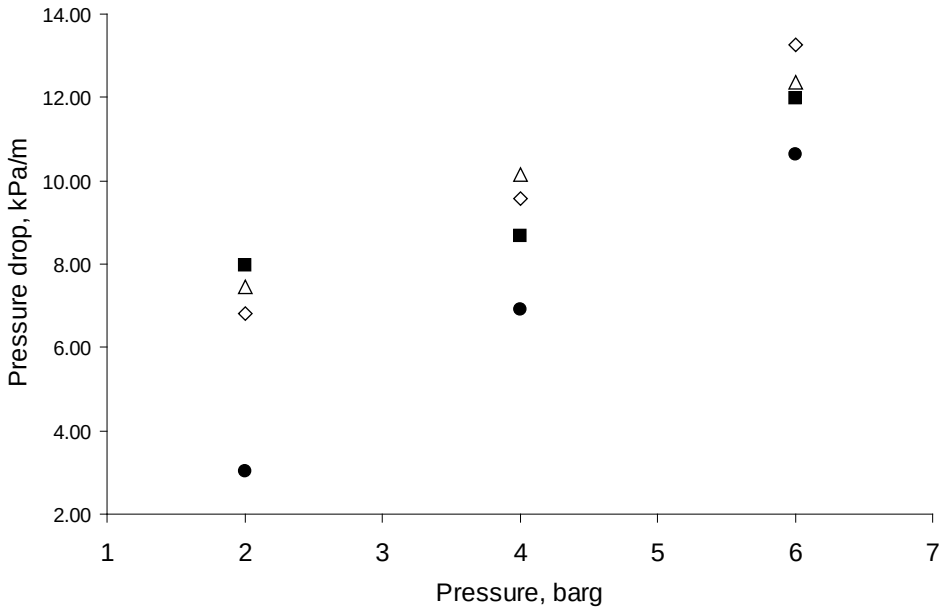

(b)

Figure 4.4 Dependence of the pressure gradient on the applied prewetting mode (U_G=36 mm/s). (a) U_L=3.6 mm/s, (b) U_L=9.52 mm/s

The analysis of Loudon et al., 2006, discussed above can be extended as follows. The initial state of the bed depends on the applied prewetting procedure and, in terms of flow structures, consists of the patterns shown in Figure 4.3. Draining the bed, i.e., applying the Levec mode, yields an initial state with predominantly pendular structures with small contributions from liquid pockets. Among others, this was demonstrated in the experiments performed by Kramer, 1998, in which the bed was flooded, drained and the resulting structures were photographed. Pendular structures are located between two touching spheres and liquid is held by the capillary forces. The Nicol mode apparently yields an initial state that has a bigger contribution of liquid pockets due to irrigation of the bed during draining. Due to very high liquid flow rate, the

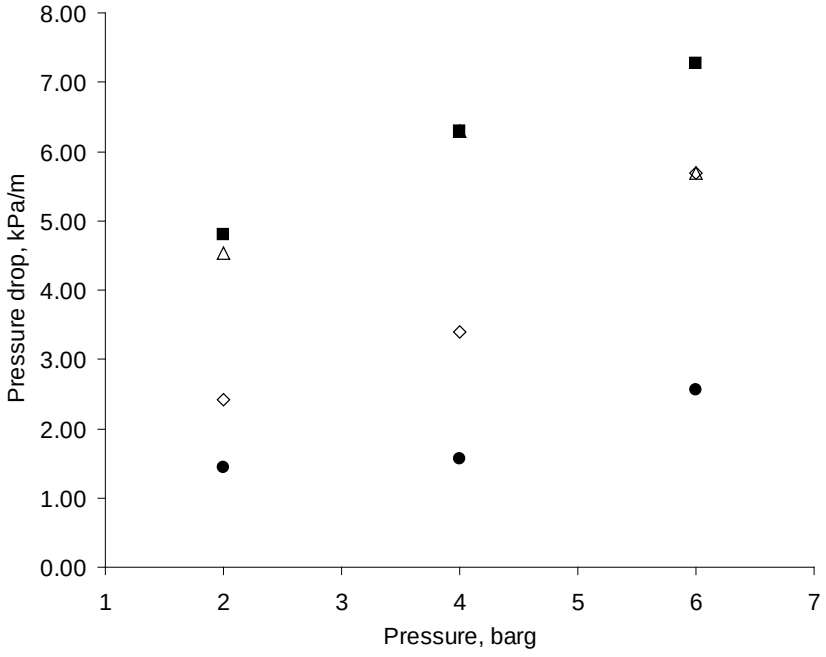

(a)

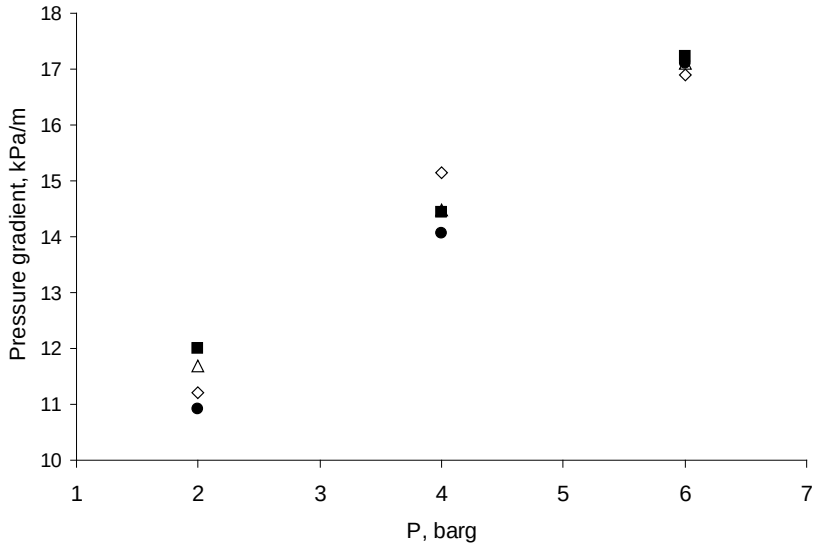

(b)

Figure 4.5 Dependence of the pressure gradient on the applied prewetting mode (for symbols see Figure 4.4). U_G=58 mm/s. (a) U_L=3.6 mm/s, (b) U_L=9.52 mm/s

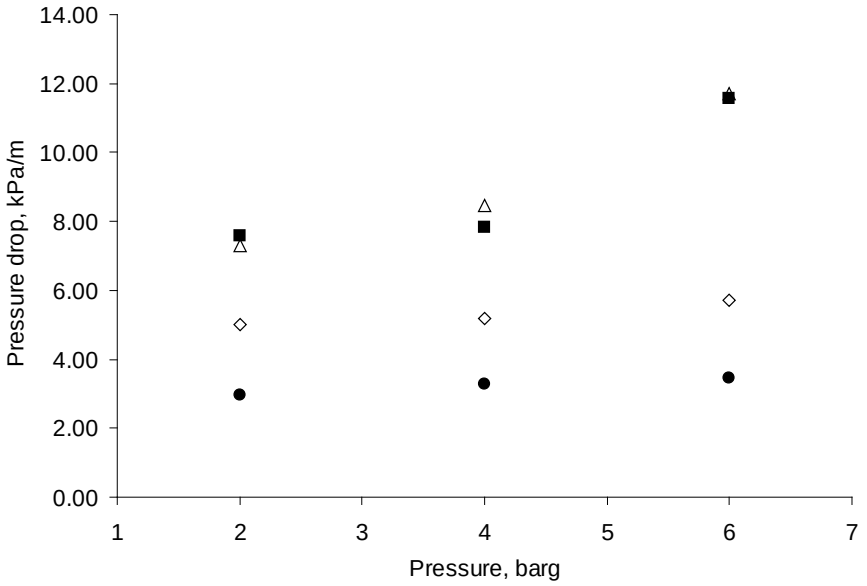

(a)

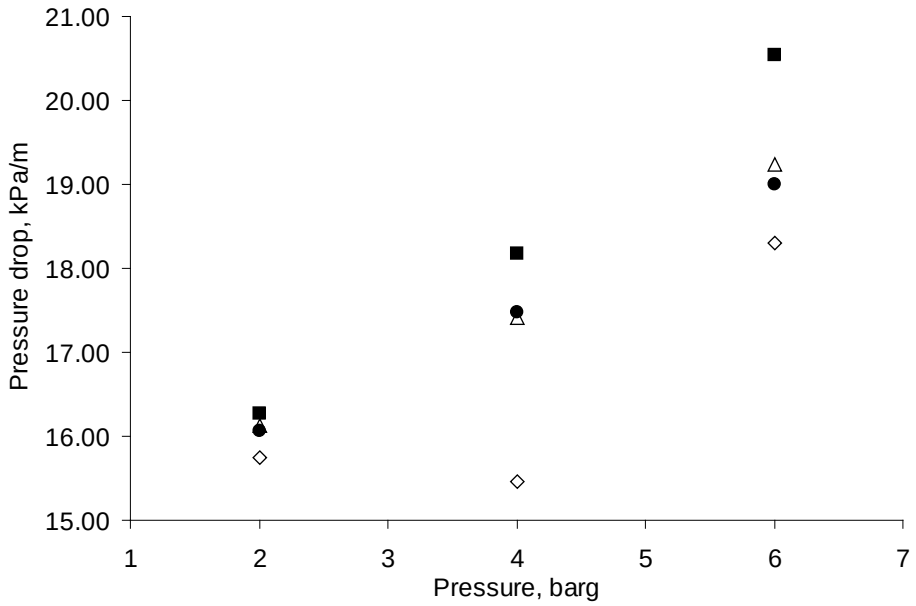

(b)

Figure 4.6 Dependence of the pressure gradient on the applied prewetting mode (for symbols see Figure 4.4). U_G=90 mm/s. (a) U_L=3.6 mm/s, (b) U_L=9.52 mm/s

Kan-liquid mode yields a similar initial state of the bed, while the Kan-gas mode gives an intermediate state between the Levec and Kan-liqud mode. The initial state of the bed determines the resulting flow distribution, just like in the cases of prewetted and non-prewetted beds (Lutran et al., 1991), and hence the variability of such state is the cause of the observed hysteresis. The better initial irrigation of the bed present in the Kan-liquid and Nicol modes yields flow distribution and patterns with corresponding higher pressure drops. One indication that this corresponds to the actual flow patterns was given by van Houwelingen et al., 2006. They examined the distribution of wetting efficiency for the case of the Kan-liquid and Levec prewetting modes. The Levec mode had a bimodal

distribution of wetting efficiency, while the Kan-liquid mode exhibited a more uniformly distributed wetting efficiency with a higher average value.

4.3.1 Effect of operating conditions on the extent of hysteresis

Figure 4.2 and Figure 4.4 - Figure 4.6 indicate that the difference in the pressure drop due to the flow history of the bed (i.e., *the extent of hysteresis*) is a strong function of the operating flow rates. For the lower flow rates (Figure 4.4-a and Figure 4.5-a), the system exhibits behavior similar to the low pressure data of Loudon et al., 2006. Three distinct regions can be seen: the Levec mode with the lowest, the Kan-liquid and Nicol mode with the highest, and the Kan-gas mode with intermediate values of pressure drop. These three regions are also present for intermediate (Figure 4.5-a) and high (Figure 4.6-a) gas velocity cases, provided that liquid velocity is in the low range. Increasing the liquid velocity (Figure 4.4-b, Figure 4.5-b and Figure 4.6-b) diminishes the difference in the pressure drop data. In a study by Wang et al., 1995, the same operating conditions were reached by looping first the liquid and then the gas velocity. The difference between the pressure drops of the upper and lower branches was higher when liquid flow was varied. The present study leads to a similar conclusion – the liquid velocity has a more pronounced effect on the extent of hysteresis than the gas velocity. The reason is that the initial state of the bed, dependent on the applied prewetting procedure as discussed

earlier, has a less pronounced effect on the flow distribution in the case of a higher liquid velocity.

In order to quantify the effect of operating flow rates and pressure on the extent of hysteresis, a *hysteresis factor* was introduced as:

$$f_H = 1 - \frac{(\Delta P / L)_{\text{Lower branch}}}{(\Delta P / L)_{\text{Upper branch}}} \tag{4-1}$$

For the investigation of the prewetting modes on the hysteresis factor, the lower branch for the pressure drop in equation (4-1) is chosen from the Levec mode, while the upper branch is taken from the Kan-liquid mode. The no hysteresis case is defined as $f_H=0$, while increased values of the hysteresis factor indicate progressively higher extents of hysteresis. According to the phenomenological analysis discussed above, increased gas flow rate enhances the liquid spreading and wetting efficiency (Case 3). Increased operating pressure has a similar, but less pronounced effect (Case 4). The effects of both gas velocity and operating pressure increase in the case of a higher liquid velocity. As a result, it is expected that the hysteresis factor, for a fixed liquid velocity, will be a decreasing function of both operating pressure and gas velocity, since enhanced spreading diminishes the influence of the initial state of the bed on the resulting pressure drop. Figure 4.7 displays the observed hysteresis factor based on the 'looping' liquid velocity data. Figure 4.8 displays the hysteresis factor based on the prewetting modes investigation. It can be seen that f_H shows strong dependence on the liquid flow rate and that two regions of values can be defined: a high hysteresis region for the low liquid

velocity and low hysteresis region for the higher liquid velocity. In the low liquid velocity region, the hysteresis factor maintains a high value irrespective of pressure or gas velocity. This implies that in this region the improvement in liquid spreading due to higher gas-liquid interactions (achieved through either higher gas density, i.e., operating pressure or higher gas velocity) is not significant. Note that these results are in agreement with X-radiography imaging of flow structures of the Levec mode performed by van der Merwe et al., 2007b, that showed no significant improvement of liquid spreading due to increased gas

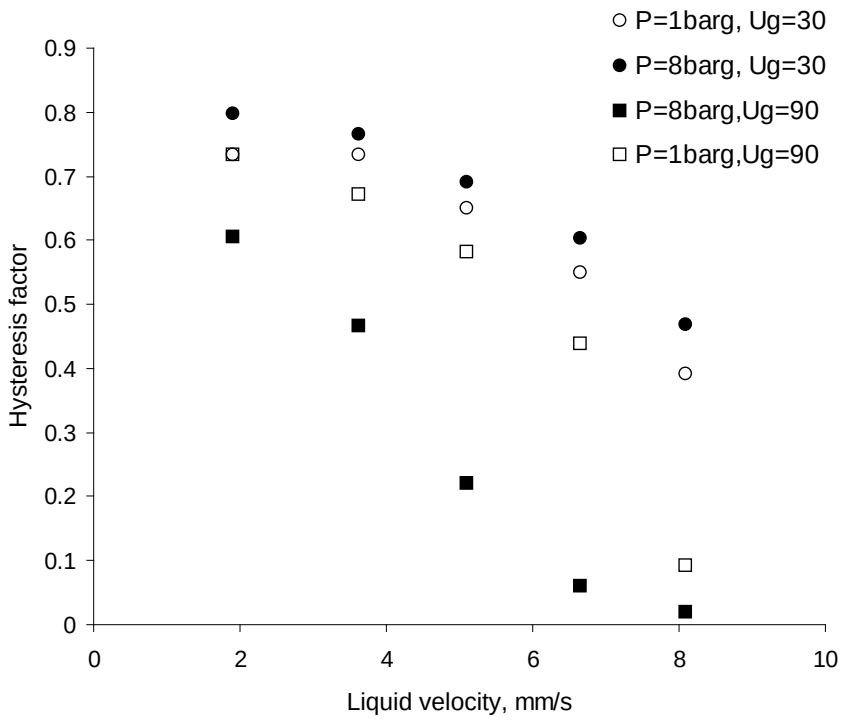

Figure 4.7 Hysteresis factor, given by equation (4-1), based on looping liquid velocity data

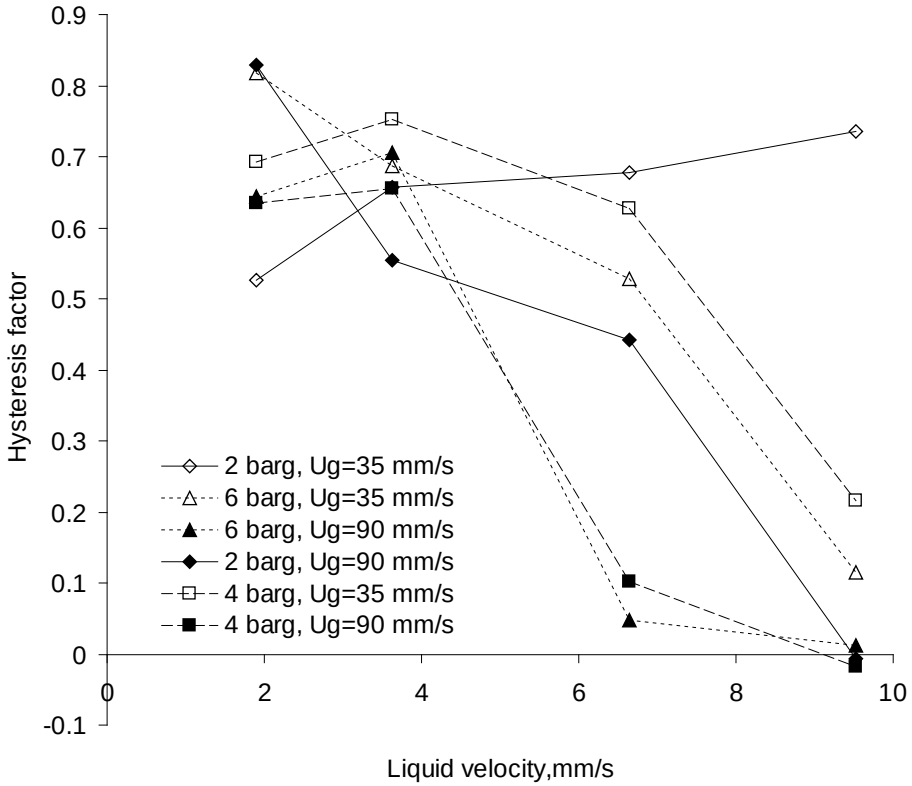

Figure 4.8 Hysteresis factor based on the prewetting modes investigation

velocity. The data points corresponding to higher liquid velocity are grouped in terms of both operating pressure and gas flow rate. The lowest values of hysteresis factor (conditions: P = 6 *barg,* U_G=90 *mm/s*) correspond to the highest pressure-highest gas velocity conditions, i.e., Case 5 of the phenomenological analysis. Gas velocity has a bigger effect on the extent of hysteresis, as seen in the three bottom curves on Figure 4.8, which are all for high gas velocity (U_G=90 *mm/s*) conditions. This is in agreement with Case 3 of the phenomenological analysis. The top three curves are for the low gas

velocity (U_G=35 *mm/s*) condition and, corresponding to the Case 4 of the analysis, are decreasing functions of operating pressure.

Figure 4.9 shows the hysteresis factor as a function of the pressure drop in the Levec mode. Note that the data all fall on one line despite the fact that they correspond to vastly different operating conditions (pressure, gas and liquid velocity). This implies that only for the Levec mode of prewetting the pressure drop uniquely determines the extent of hysteresis. Pressure drop data for the other prewetting modes do not show this trend. The linear fit of data with the non-zero value of hysteresis factor, i.e., for the pressure drops of up to 13 kPa/m, has the slope of about -0.06. It would be instructive to examine whether the slope of this line is a function of other system parameters, such as the size of packing, surface tension and density of the liquid phase. Such enlarged data set would allow development of the correlation for the prediction of the hysteresis factor.

In Chapter 5 the developed CFD model is used to predict pressure drop in Levec mode. Combined with results shown in Figure 4.9, this enables the prediction of the hysteresis factor and deduction of conditions which lead to hysteresis free operation.

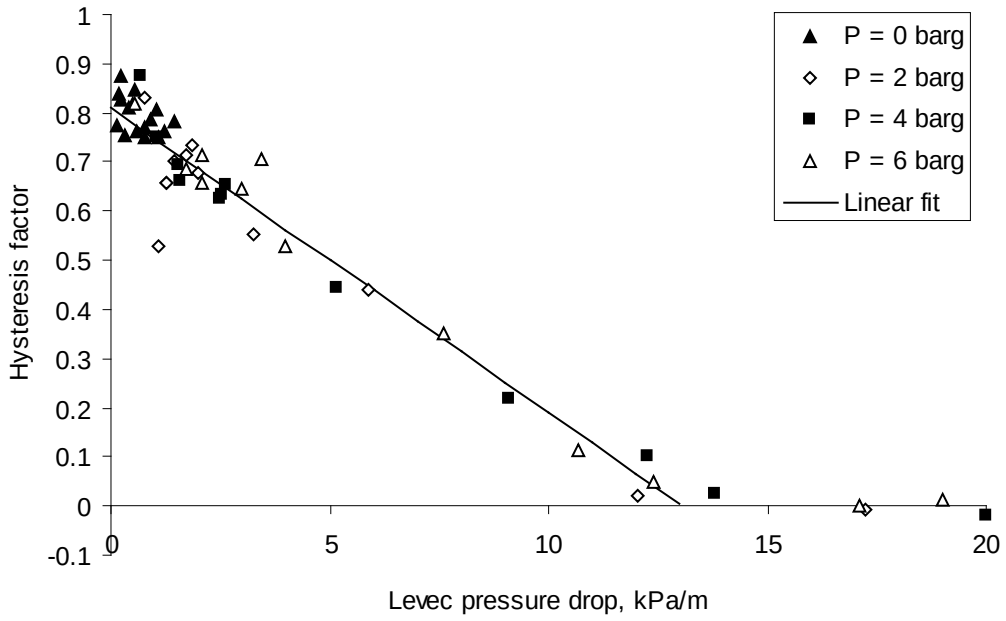

Figure 4.9 Hysteresis factor as a function of pressure drop in the Levec mode. P = 0 barg data adapted from Loudon et al., 2006(water-nitrogen-3 mm glass beads system, U_L=3-9 mm/s, U_G=20-90 mm/s)

4.4 Summary

The experimental results obtained by 'looping' liquid velocity while using different above described prewetting modes confirm the presence of hysteresis in a high pressure trickle bed. A hysteresis factor has been introduced to quantify the extent of hysteresis and was found to be a strong function of the operating flow rates and pressure. For the lower liquid flow rates, pressure drop hysteresis seems to persist regardless of the pressure or gas flow rate. However, in the region of higher liquid flow rates, increases in both pressure and gas flow rate will decrease the extent of hysteresis.

Chapter 5
Computational Fluid Dynamics Modeling of Trickle Bed Reactors

5.1 Introduction

General aspects of the computational fluid dynamics (CFD) approach applied to trickle bed reactors (TBRs) have been reviewed in Chapter 2. Note that throughout this text, we focus on the Eulerian CFD model of TBRs. For the other approaches, such as volume of fluid (VOF), see discussion in Raynal and Harter, 2001; Gunjal et al., 2005b; Lopes and Quinta-Ferreira, 2008a; and Augier et al., 2008. Comprehensive reviews of TBR phenomenological and CFD modeling are available in Kuipers and Van Swaaij, 1997, and Carbonell, 2000. The details of the derivation of the volume averaged governing equations are given in Anderson and Jackson, 1967; Ishii, 1975; Drew, 1983, and Bird et al., 2001.

5.2 Scope and Outline

Our study focuses on: (i) developing a robust hydrodynamic Eulerian CFD model, and (ii) use of predicted hydrodynamic solution together with species balance to yield TBR performance assessment. This reactive flow study addresses gas and liquid limited

systems and for each case a closed form approach of coupling bed and particle scale solution within CFD framework is presented.

5.3 Model description

5.3.1 Governing equations

Governing equations of the Eulerian CFD model are the volume averaged mass and momentum conservation equations (Anderson and Jackson, 1967; Ishii, 1975; Drew, 1983, and Bird et al., 2001) given in Table 5.1.

Table 5.1 Governing equations of the Eulerian CFD model

$\frac{\partial}{\partial t}\left(\varepsilon_\alpha \rho_\alpha\right)+\nabla\cdot\left(\varepsilon_\alpha \rho_\alpha \vec{u}_\alpha\right)=0$	(5-1)
$\frac{\partial}{\partial t}\left(\varepsilon_\alpha \rho_\alpha \vec{u}_\alpha\right)+\nabla\cdot\left(\varepsilon_\alpha \rho_\alpha \vec{u}_\alpha \vec{u}_\alpha\right)=-\varepsilon_\alpha \nabla P_\alpha+\varepsilon_\alpha \rho_\alpha \vec{g}+\nabla\cdot\bar{\bar{\tau}}_\alpha+\vec{F}_\alpha$	(5-2)
$\vec{F_\alpha}=\sum_{\beta=1}^{n} K_{\beta\alpha}\left(\vec{u}_\beta-\vec{u}_\alpha\right)$	(5-3)
$\bar{\bar{\tau}}_\alpha=\varepsilon_\alpha \mu_\alpha\left(\nabla\vec{u}_\alpha+\left(\nabla\vec{u}_\alpha\right)^T\right)$	(5-4)

5.3.2 Implementation of experimental porosity distribution in the CFD grid

Porosity distribution as observed on the length scale of couple of particle diameters is Gaussian. (For more details see discussion in Chapter 2.5.2, the experimental study presented in Chapter 3.3; see also studies of Roblee et al., 1958; Benenati and Brosilow, 1962; Stephenson and Stewart, 1986; Mueller, 1991; Mantle et al., 2001, and Baldwin et al., 1996).

The need for implementation of porosity profile on the computational domain has been recognized first in the studies of packed beds with single phase flow (Stanek and Szekely, 1974). Such approach has been further developed and incorporated into the CFD models of TBRs (Propp et al., 2000, Jiang et al., 2002a, Gunjal et al., 2005a, Atta et al., 2007a). We extend such methodology to the three dimensional (3D) computational grid used in this study. Mueller, 1991 correlation (equation (5-5)) is used to generate the longitudinally averaged radial profile of porosity (Figure 5.1). Resulting profile is then integrated with respect to radial position to

$$\varepsilon_B(r) = \varepsilon_B + (1-\varepsilon_B) J_0(ar^*) \exp(-br^*)$$

$$(a,b) = f(D_c, d_p) \qquad (5\text{-}5)$$

$$r^* = r / d_p$$

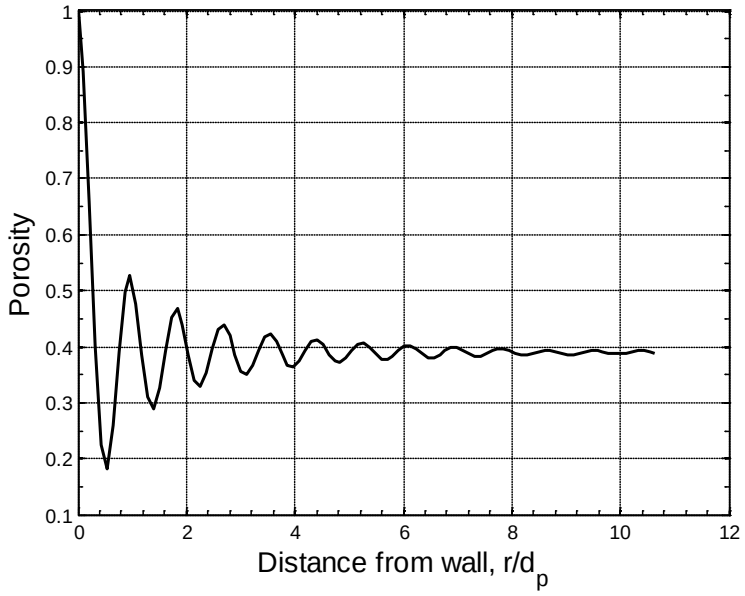

Figure 5.1. Longitudinally averaged radial profile of porosity generated using Mueller, 1991 correlation. Bed average value of porosity is 0.39; packing particle diameter is 3 mm.

yield the averaged porosity on 10 radial sections (equation (5-6)). In each radial section,

$$\left\langle \varepsilon_{B_i} \right\rangle = \frac{1}{r_i^{end} - r_i^{init}} \int_{r_i^{init}}^{r_i^{end}} \varepsilon_B(r) dr \tag{5-6}$$

Gaussian distribution is imposed around the calculated mean in each section with the standard deviation value (15%) obtained based on computed tomography (CT) imaging as given in Chapter 3.3. One such radial section is shown in Figure 5.2 together with the resulting porosity distribution for the entire computational domain.

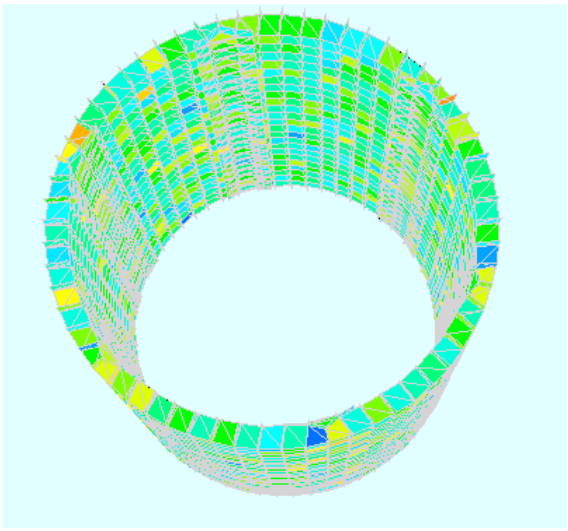

(a)

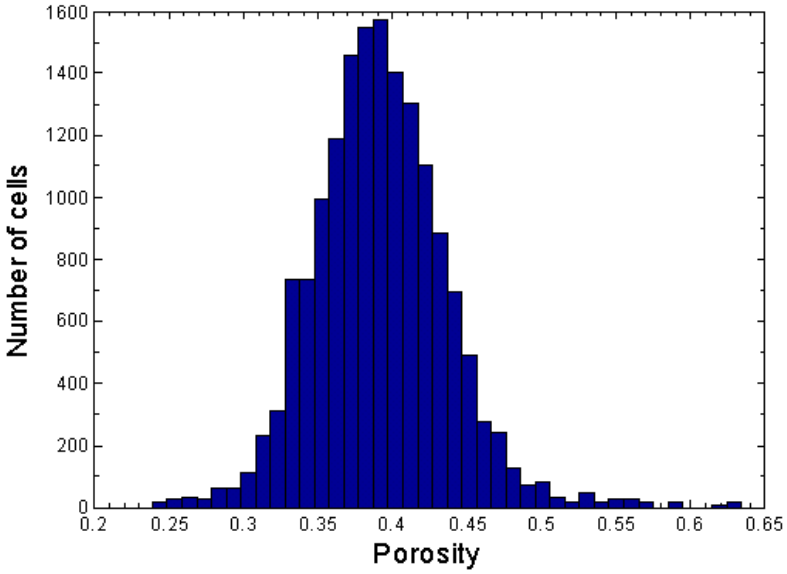

(b)

Figure 5.2. (a) Representative radial section ($0.90 \le r/(D_c/2) \le 1.0$) in the porosity map on the CFD computational domain. In each radial section, Gaussian distribution is imposed around the mean obtained by the integration of the Mueller, 1991 correlation. (b) Resulting porosity distribution map for the entire computational domain.

5.3.3 Closures

Phase interaction closures based on the model of Attou et al., 1999 are used (Table 5.2). We also examine the approach based on the principles of statistical hydrodynamics (Crine et al., 1992) as discussed below.

Table 5.2 Phase interaction closures (Attou et al., 1999)

Phases	Momentum exchange coefficient, kg/m^{3}s
gas-liquid	$K_{GL} = \frac{E_1(1-\varepsilon_G)^2}{\varepsilon_G d_p^2}\left(\frac{1-\varepsilon_B}{1-\varepsilon_G}\right)^{2/3}\mu_G + \frac{E_2(1-\varepsilon_G)}{d_p}\left(\frac{1-\varepsilon_B}{1-\varepsilon_G}\right)^{1/3}\rho_G\left\|\vec{u}_G - \vec{u}_L\right\|$ (5-7)
gas-solid	$K_{GS} = \frac{E_1(1-\varepsilon_G)^2}{\varepsilon_G d_p^2}\left(\frac{1-\varepsilon_B}{1-\varepsilon_G}\right)^{2/3}\mu_G + \frac{E_2(1-\varepsilon_G)}{d_p}\left(\frac{1-\varepsilon_B}{1-\varepsilon_G}\right)^{1/3}\rho_G\left\|\vec{u}_G\right\|$ (5-8)
liquid-solid	$K_{LS} = \frac{E_1(1-\varepsilon_B)^2}{\varepsilon_L d_p^2}\mu_L + \frac{E_2(1-\varepsilon_B)}{d_p}\rho_G\left\|\vec{u}_L\right\|$ (5-9)

Numerous studies (Lutran et al., 1991 ; Ravindra et al., 1997, and Marcandelli et al., 2000, see also Chapter 3.3) have provided ample experimental evidence of incomplete wetting and liquid channeling at lower values of the liquid flux (liquid mass velocity). To account for such observations, Christensen et al., 1986 (see also Charpentier et al., 1968) conceptualized the picture of the two phase flow through packed beds as the combination of rivulet and film flow. The contribution of each flow pattern depends on the operating conditions and the flow history of the bed. In this study, we base the CFD model development on such phenomenological picture and propose a methodology to introduce the dependence of CFD phase interaction closures upon the flow structures

Table 5.3. Basic equations of the extended model closure (Crine et al., 1992, Wijffels et al., 1974, Saez and Carbonell, 1985)

Description	Equation	
Local (mesoscale) Reynolds number	$\mathrm{Re}_{L,i} = \{0, \mathrm{Re}_{\min}, ..., i\,\mathrm{Re}_{\min}, ..., \mathrm{Re}_{\max}\}$	(5-10)
Minimum Reynolds number assuring catalyst wetting (Wijffels et al., 1974)	$\mathrm{Re}_{\min} = \frac{1}{E_1}\left(\frac{\varepsilon_B}{0.5}\right)^3 (1-\cos\theta)^3 Ga_L^3 \frac{\Delta P/\Delta z + \rho_L g}{\rho_L g}$	(5-11)
Reduced Reynolds number	$\mathrm{Re}^*_{L,i} = \frac{\mathrm{Re}_{L,i}}{\mathrm{Re}_{\min}}$	(5-12)
(Maximum) Reynolds number at which local flooding occurs	$\psi = E_1 \frac{\left(1-\varepsilon_B+\varepsilon_L^0\right)^2}{\left(\varepsilon_B-\varepsilon_L^0\right)^3}\frac{\mathrm{Re}_{\max}}{Ga_L} + E_2 \frac{\left(1-\varepsilon_B+\varepsilon_L^0\right)}{\left(\varepsilon_B-\varepsilon_L^0\right)^3}\frac{\mathrm{Re}^2_{\max}}{Ga_L}$	(5-13)
Probability of occurrence of $\mathrm{Re}^*_{L,i}$	$p(\mathrm{Re}^*_{L,i}) = \exp\left(c + d\,\mathrm{Re}_{L,i}\right)$	(5-14)
Constraint on the zeroth moment	$\int_0^{\mathrm{Re}^*_{\max}} p(\mathrm{Re}^*_{L,i})\, d\,\mathrm{Re}^*_{L,i} = 1$	(5-15)
Constraint on the first moment	$\int_0^{\mathrm{Re}^*_{\max}} \mathrm{Re}^*_{L,i}\; p(\mathrm{Re}^*_{L,i})\, d\,\mathrm{Re}^*_{L,i} = \mathrm{Re}_L$	(5-16)
Gas phase local momentum equation	$\frac{\rho_L}{\rho_G}(\psi - 1) = E_1 \frac{\left(1-\varepsilon_G\right)^2}{\varepsilon_G^{\,3}}\frac{\mathrm{Re}_{G,i}}{Ga_G} + E_2 \frac{\left(1-\varepsilon_G\right)}{\varepsilon_G^{\,3}}\frac{\mathrm{Re}^2_{G,i}}{Ga_G}$	(5-17)
Liquid phase local momentum equation	$\psi = E_1 \frac{\left(1-\beta_{dyn,i}\right)^2}{\beta^3_{dyn,i}}\frac{\mathrm{Re}_{L,i}}{Ga_L} + E_2 \frac{\left(1-\beta_{dyn,i}\right)}{\beta^3_{dyn,i}}\frac{\mathrm{Re}^2_{L,i}}{Ga_L}$	(5-18)
Estimate of liquid phase permeability (Saez and Carbonell, 1985)	$k_L = E_1 \frac{\left(1-\varepsilon_B\right)^2}{\varepsilon_B^3}\frac{\mathrm{Re}_L}{Ga_L} + E_2 \frac{\left(1-\varepsilon_B\right)}{\varepsilon_B^3}\frac{\mathrm{Re}^2_L}{Ga_L}$	(5-19)
Overall dynamic liquid holdup	$\beta_{dyn} = \int_0^{\mathrm{Re}^*_{\max}} \beta_{dyn,i}\, p(\mathrm{Re}^*_{L,i})\, d\,\mathrm{Re}^*_{L,i}$	(5-20)
Local wetting efficiency	$\eta_{CE,i} = \begin{cases} 1, & \mathrm{Re}^*_{L,i} \geq 1 \\ 0, & \mathrm{Re}^*_{L,i} < 1 \end{cases}$	(5-21)
Overall wetting efficiency	$\eta_{CE} = \int_0^{\mathrm{Re}^*_{\max}} \eta_{CE,i}\, p(\mathrm{Re}^*_{L,i})\, d\,\mathrm{Re}^*_{L,i}$	(5-22)

present in the bed. In this way, a more robust CFD model will allow more elaborate analysis of trickle flow and the prediction of phenomena such as hysteresis (discussed in Chapter 4).

In the study of Crine et al., 1992, trickle flow was modeled by considering overall (bed) and meso length scales. The bed scale flow is characterized by the average Reynolds number (Re_L). Further, it was assumed that, given the overall, average flow rate on the bed scale, there is the possibility of occurrence of a range of mesoscale flow rates ($Re_{L,i}$). Such probability was described by the exponential probability density distribution function (equation (5-14)). The local liquid Reynolds number cannot take values higher than the one corresponding to flooding (equation (5-13)). Gas and liquid phase flow at the mesoscale was modeled by Ergun-like equations (equations (5-17) and (5-18), respectively). The wetting criteria parameter of Wijffels et al., 1974 (equation (5-11)) was used to designate local catalyst wetting efficiency as either null or one (equation (5-21)). By averaging the local values, the overall values of dynamic holdup (equation (5-20)) and catalyst wetting efficiency (equation (5-22)) can be calculated.

In our study, to introduce the dependence of phase interaction closures on the type of flow structures the relative permeability concept is used. As discussed earlier (Chapter 2.4.3, equation (5-19)), Saez and Carbonell, 1985 defined the liquid and gas relative permeabilities as the ratio of pressure drop in single phase and two phase flow. Thus,

pressure drop in two phase flow is modeled based on the one phase flow pressure drop (i.e., Ergun, 1952 equation) and the value of relative permeability.

Relative permeability is then fitted to the experimental data and typically correlated to the liquid dynamic holdup (Chapter 2.4.3, Table 2.2). Based on the expressions presented in Table 5.3 liquid phase relative permeability is here further related to the wetting characteristics of the packing via the critical (minimum) Reynolds number value, Re_{min}.

Capillary closure is given by Grosser et al., 1988 model; i.e., correlation of Leverett J-function (Leverett, 1941, see also Chapter 2.5.4) for the conditions of trickle flow. The resulting expression is equation (5-23).

$$P_c = \frac{2\sigma}{d_p}\left(\frac{1-\varepsilon_B}{1-\varepsilon_G}\right)^{1/3}\left[1+\left(\frac{\sqrt{3}}{\pi}-\frac{1}{2}\right)^{-1/2}\right] \qquad (5\text{-}23)$$

5.3.4 Species balance and particle scale models

The general expression for species balance adapted to our Eulerian CFD model is given by equation (5-24). The last term on the RHS represent the creation/disappearance of species *i* in chemical reactions. Its proper representation, in general, requires consideration of interphase and intraparticle mass transfer of reacting species. We here introduce the particle scale equations to account for mass transfer and partial wetting in our reactive flow CFD model.

$$\frac{\partial}{\partial t}\left(\rho_\alpha Y_{i,\alpha}\right)+\nabla\cdot\left(\rho_\alpha \vec{u}_\alpha Y_{i,\alpha}\right)=\nabla\cdot\left(\rho_\alpha D_{i,m}\nabla Y_{i,\alpha}\right)+\sum_{r=1}^{N_R} R_{i,r} \tag{5-24}$$

The two general cases considered here are (i) liquid reactant limited reaction with non-volatile liquid phase, (ii) and gas reactant limited system. Both systems are considered isothermal; i.e., interphase and intraparticle thermal gradients are considered negligible. The particle scale implementation for case (i) is based on the exact solution for the partially wetted, infinitely long cylinder particle (Mills and Dudukovic, 1979, Table 5.4). The hydrodynamic CFD solution is used to prescribe the local flow field, and values of wetting efficiency and rates of interphase mass transfer (see below for more details).

The particle scale implementation for case (ii) is based on the approximate solution as proposed by Beaudry et al., 1987. To make analytical or numerical solution feasible, the existence of dry, wetted and half wetted catalyst particles is assumed. The solution is then sought for each case and overall catalyst efficiency is obtained as the weighted average of the three contributions as given in equation (5-25).

$$\eta=\left(1-\eta_{CE}\right)\ \eta_d+2\ \left(1-\eta_{CE}\right)\eta_{CE}\eta_{hw}+\eta_{CE}^2\eta_w \tag{5-25}$$

The needed estimate of mass transfer parameters was obtained using correlations given in Table 5.5; however, experimental values are used where available. The Eulerian model does not yield the value of wetting efficiency since no particle scale geometry is assumed

and gas-liquid interpface is not resolved. Hence, the correlations given in Table 5.5 are used.

Table 5.4 Solution to the particle scale model for liquid limited reaction for with non-volatile liquid phase (Mills and Dudukovic, 1979)

$\sum_{j=1}^{\infty} A_{i,j} e_j = G_i$	(5-26)
$u(\xi,\kappa) = \frac{e_1}{\phi}\frac{I_0(\phi\,\xi)}{I_1(\phi)} + \sum_{n=2}^{\infty} \frac{e_n \cos[(n-1)\theta]}{\phi \frac{I_{n+1}(\phi)}{I_n(\phi\,\xi)} + n - 1}$	(5-27)
$A_{11} = \pi\left[1 + \eta_{CE}\left(t_1^2 - 1\right)\right]$	(5-28)
$A_{i1} = \frac{\sin\lfloor(i-1)\pi\ \eta_{CE}\rfloor}{i-1}\left(t_i t_j - 1\right)$	(5-29)
$A_{1i} = \frac{\sin\lfloor(i-1)\pi\ \eta_{CE}\rfloor}{i-1}\left(t_i t_j - 1\right), 2 \le i \le \infty$	(5-30)
$A_{ij} = \frac{1}{2}\left[\frac{\sin\lfloor(i+j-2)\pi\ \eta_{CE}\rfloor}{i+j-2} + \frac{\sin\lfloor(i-j)\pi\ \eta_{CE}\rfloor}{i-j}\right]\left(t_i t_j - 1\right), 2 \le i \le \infty$	(5-31)
$A_{ii} = \frac{\pi}{2} + \frac{1}{2}\left[\pi\ \eta_{CE} + \frac{\sin\left[2\ (i-1)\pi\ \eta_{CE}\right]}{2\ (i-1)}\right]\left(t_i^{\,2} - 1\right), 2 \le i \le \infty$	(5-32)
$G_1 = \pi\ \eta_{CE}\ t_1 \quad G_i = t_i \frac{\sin\lfloor(i-1)\pi\ \eta_{CE}\rfloor}{i-1}, \quad 2 \le i \le \infty$	(5-33)
$t_i^{-1} = \phi \frac{I_i(\phi)}{I_{i-1}(\phi)} + i - 1, \quad 1 \le i \le \infty$	(5-34)

Table 5.5 Correlations used in the reactive flow CFD model

$k_{LS} = 4.25 \frac{D_{i,m}\varepsilon_p}{d_p \eta_{CE}} \mathrm{Re}_L^{0.48}\, Sc_L^{0.33}$	Tan and Smith, 1982	(5-35)
$D_{i,m} = \frac{7.4 \cdot 10^{-10} \left(2.6\ M_B\right)^{1/2} T}{\mu_B V_A^{0.6}}$	Wilke and Chang, 1955	(5-36)
$\eta_{CE} = 1.617\ \ \mathrm{Re}_L^{0.146}\ \ Ga_L^{-0.071}$	El-Hisnawi et al., 1982	(5-37)
$\eta_{CE} = 1.104\, \mathrm{Re}_L^{1/3} \left(\frac{1 + \Delta P / \Delta z / (\rho_L g)}{Ga_L} \right)^{1/9}$	Al-Dahhan and Dudukovic, 1995	(5-38)

5.3.5 Solution Strategy

An unstructured, three-dimensional computational grid representing the TBR column geometry has been created in GAMBIT. Unsteady state model is solved using Fluent (Figure 5.3) until steady state is reached. Mueller, 1991 correlation and CT data were used to calculate the values of sectional porosity using the codes written in Matlab. Values of porosity were then patched into the solver using user defined functions (UDFs) written in C programming language. Phase interaction closures have been specified using UDFs. Capillary closure has been introduced as the source term in the momentum equations and specified using UDFs. Particle scale and interphase mass transfer models were specified using UDFs within species transport module of Fluent 6.2 Eulerian model.

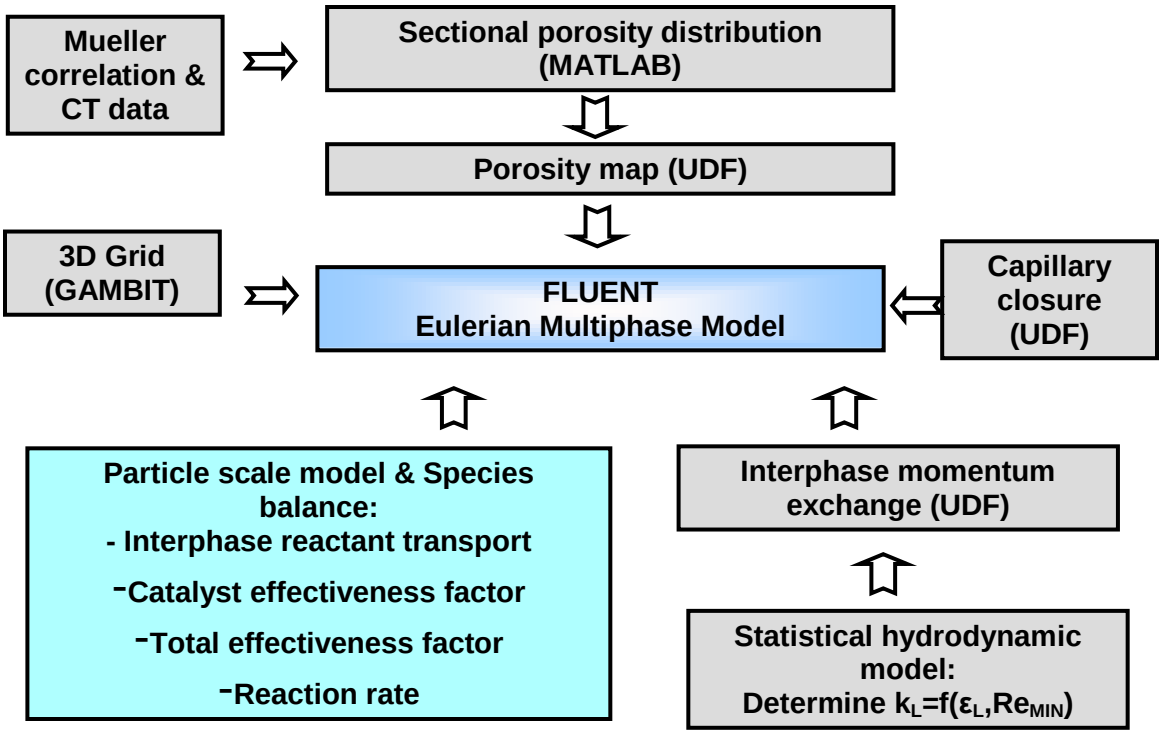

Figure 5.3. CFD model – solution strategy.

Initial conditions were as given in equation (5-39). On the cylindrical column wall the no-slip boundary condition is used. By using three different cell sizes in the computational grid it was verified that 40,000 cells on the domain are sufficient to achieve grid independent results.

$$\begin{aligned} \varepsilon_I &= \varepsilon_I^0 \\ \varepsilon_S &= 1-\varepsilon_B = const \\ u_G &= 10^{-6}\, m/s \\ u_I &= 10^{-6}\, m/s \\ u_S &= 0 = const. \end{aligned} \qquad (5\text{-}39)$$

Inlet boundary condition is set to mimic the top liquid distributor. The distributor is a 2.5 cm (1”) high box directly connected to the liquid injection tube. The liquid injected in

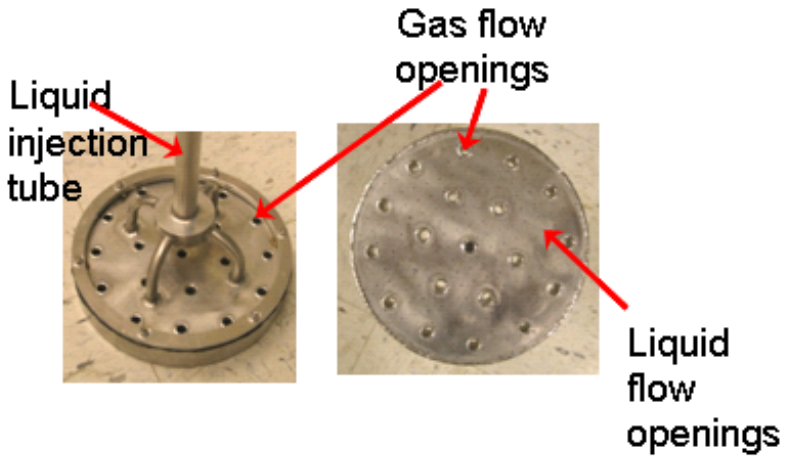

(a)

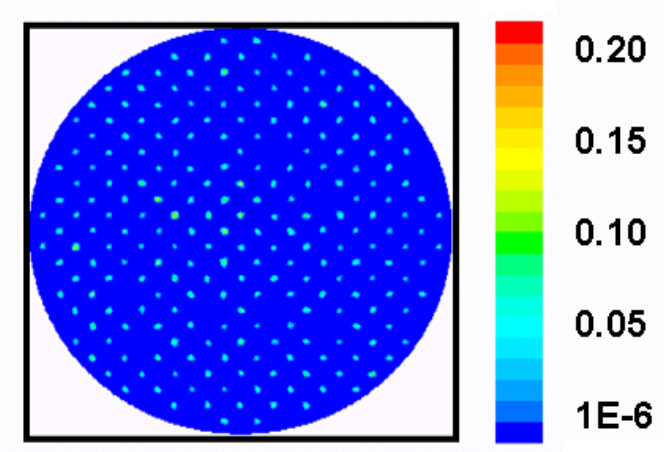

(b)

Figure 5.4. Inlet boundary condition: (a) Distributor geometry (see also Appendix A, Figure A-5), (b) Implementation of liquid velocity at the inlet boundary. Colorbars represent liquid velocity in m/s.

the distributor exits through 240 holes of 0.9 mm diameter. The air injected at the top of the column flows through 19 tubes (6.5 mm I.D) passed axially though the distributor (see Appendix A and Figure A-5). Hence, the inlet BC is set as shown in Figure 5.4.

5.4 Results and Discussion

5.4.1 Packing wetting characteristics – Re_{min} value

As discussed, Re_{min} is the minimum value of local Reynolds number that ensures the compete wetting of the external catalyst surface as per model of Wijffels et al., 1974. It is dependent on both packing particles' (ε_B, E_1) and liquid phase (Ga_L) properties (equation (5-11)). Figure 5.5 is an example of the distribution of the Re_{min} values on the CFD computational grid. As shown, Re_{min} is drastically affected by the values of contact angle ($\theta=30^0$ and $\theta=43.5^0$ in Figure 5.5 (a) and (b), respectively). It should be noted that value of θ is here a model parameter that is not strictly related to the exact definition of contact angle (Chapter 2.4.2). Wijffels et al., 1974 and later Crine et al., 1992, have used θ to indicate the likelihood of occurrence of film flow on the mesoscale and we adopt the same approach here. Unless otherwise indicated, for the simulation of the results presented below, value of $\theta=30^0$ is used (see Wijffels et al., 1974 and Crine et al., 1992).

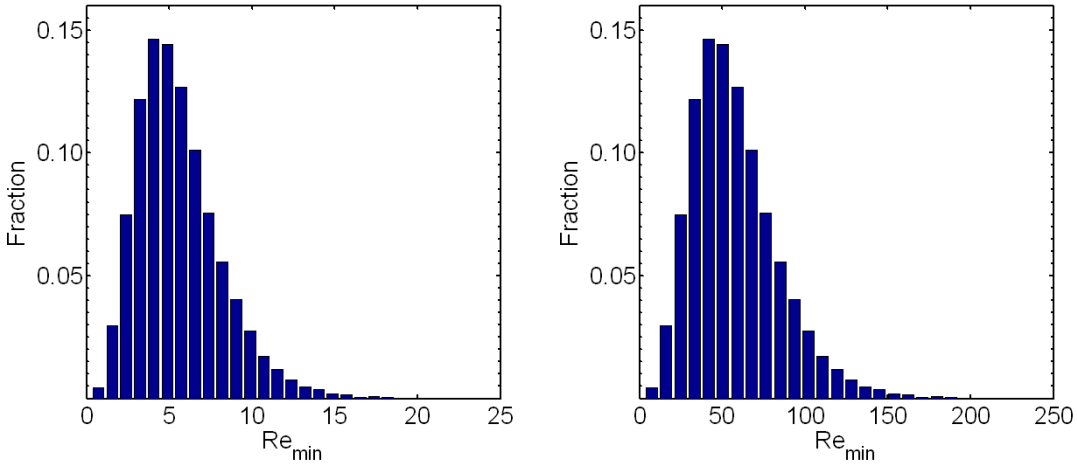

Figure 5.5. Wijffels et al., 1974 wetting criteria (Re_{min}) on the CFD computational grid. (a) $\theta=30^0$, (b) $\theta=43.5^0$. Ordinate indicates the fraction of cells on the CFD grid with value of Re_{min} indicated on the abscissa.

5.4.2 Prediction of liquid holdup and wetting efficiency

In Figure 5.6, the experimental (this study) and calculated values of liquid holdup are shown. In Figure 5.7, the experimental (Al-Dahhan and Dudukovic, 1995) and calculated values of overall liquid holdup and wetting efficiency are shown. As discussed, wetting efficiency on the CFD domain is estimated utilizing correlations; in this case, correlation of Al-Dahhan and Dudukovic, 1995, equation (5-38), is used. The results indicate satisfactory agreement between experimental and model values with average absolute percentage error of about 15%.

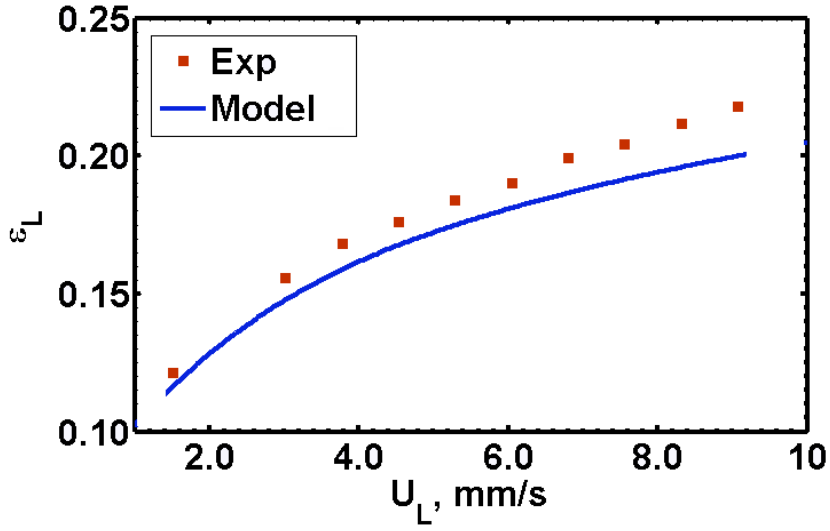

(a)

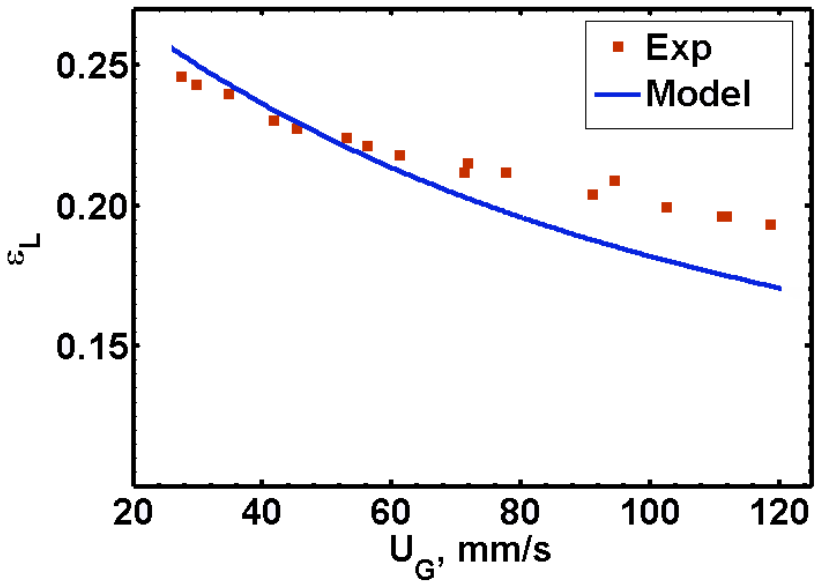

(b)

Figure 5.6. Simulated and experimental values of liquid holdup in the bed of extrudates. (a) P=4 barg, U_G = 70 mm/s, (b) P = 1 barg, U_L = 4.53 mm/s.

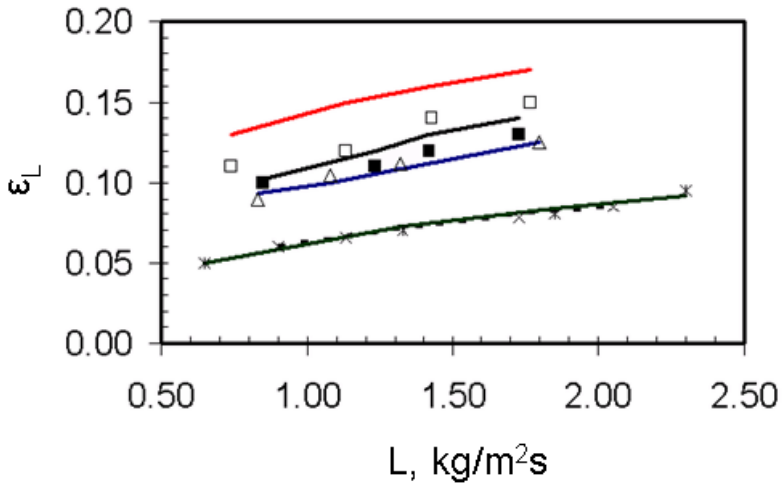

(a)

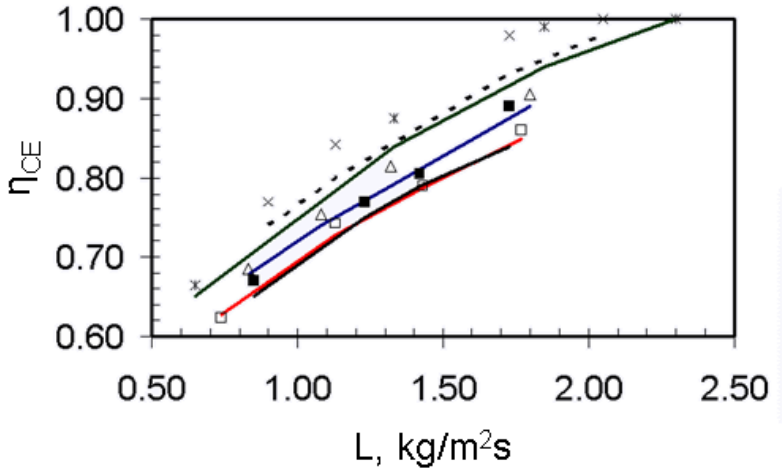

(b)

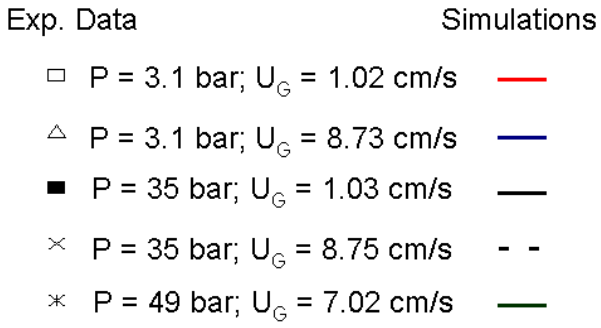

Figure 5.7. Simulated and experimental values (Al-Dahhan and Dudukovic, 1995) of (a) liquid holdup and (b) wetting efficiency in the bed of extrudates.

5.4.3 Prediction of hysteresis

As discussed in Chapter 4, the basic design and operating parameters for trickle beds (pressure drop, liquid holdup) exhibit dependence on the flow history of the bed. This is termed *hysteresis* or *the multiplicity of hydrodynamic states* in trickle beds. The existence of hysteresis has been attributed to the fact that predominant flow structures, for example, film flow or rivulet flow, are different for the upper and lower branches (Christensen et al., 1986, and Lutran et al., 1991). The flow structure determines the extent of the interaction between the phases and thus each leads to distinct values of hydrodynamic parameters, such as the pressure drop and liquid holdup.

CFD model described above enables the prediction of hysteresis loops since it accounts for the dependence of the extent of phase interactions on the predominant flow pattern. In Figure 5.8, the calculated hysteresis loops are shown together with the experimental ones. In Figure 5.9, the comparison of hysteresis factors (see Chapter 4) is given. The average absolute percentage error for the data shown in Figure 5.8 is 30% for the lower branch and about 14% for the upper branch of the hysteresis loop. In principle, the predictions could be significantly improved if contact angle (θ, equation (5-11)) is treated as fitting parameter either for each branch as a whole or each individual experimental point. However, we used the values obtained by fitting the large database of literature TBR data (Crine et al., 1992) for systems similar to our HPTBR to avoid loss of generality of model predictions.

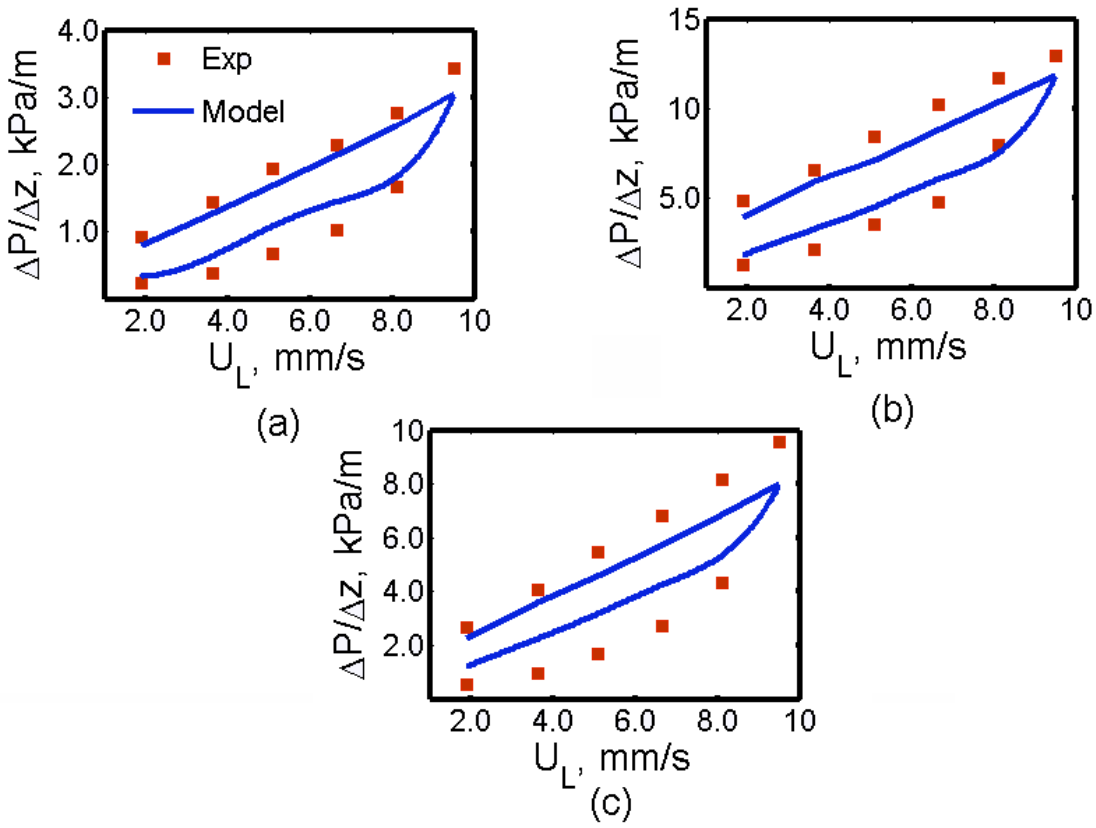

Figure 5.8. Simulated vs experimental values of pressure drop in hysteresis loop: (a) U_G=27 mm/s, P=1 barg, (b) U_G=90 mm/s, P=1 barg, (c) U_G=27 mm/s, P=8 barg. θ=30^0 for upper branch and θ=43^0 for lower branch.

As discussed in Chapter 4, in order to quantify the effect of operating flow rates and pressure on the extent of hysteresis, the *hysteresis factor* was previously introduced and is presented here:

$$f_H = 1 - \frac{(\Delta P / L)_{\text{Lower branch}}}{(\Delta P / L)_{\text{Upper branch}}} \tag{5-40}$$

The no hysteresis case is thus defined by $f_H=0$, while increased values of the hysteresis factor indicate progressively higher extents of hysteresis. The increased liquid and gas flow rate enhance the liquid spreading and wetting efficiency. Increasing the operating pressure has a similar, but less pronounced effect. The experimental and predicted values of hysteresis factor are shown in Figure 5.9. The hysteresis factor values are invariably under-predicted and show a less pronounced dependence on the value of liquid velocity than the experimental data. This indicates that model does not fully capture the channeling occurring at lower values of liquid velocity.

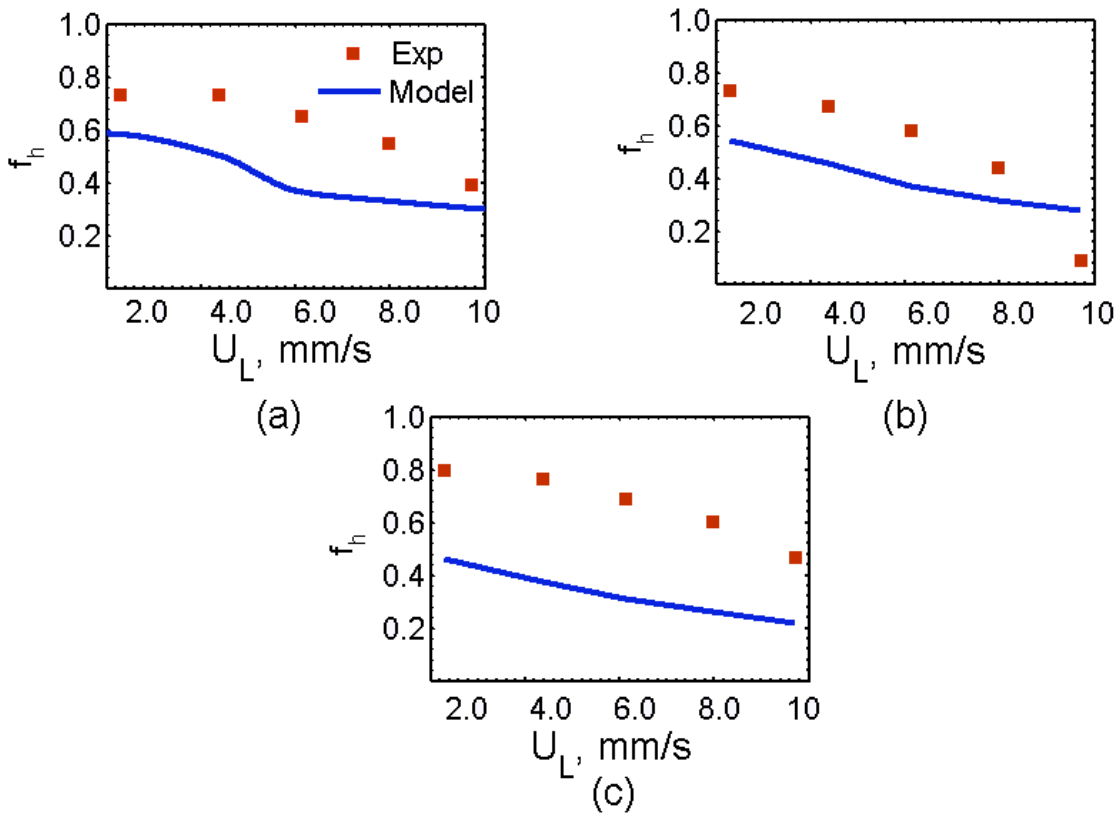

Figure 5.9. Simulated vs experimental values of hysteresis factor: (a) U_G=27 mm/s, P=1 barg, (b) U_G=90 mm/s, P=1 barg, (c) U_G=27 mm/s, P=8 barg. $\theta=30^0$ for upper branch and $\theta=43^0$ for lower branch.

In Figure 5.10 the predicted values of wetting efficiency for the lower and upper branch of the hysteresis loops are shown. As expected, the upper branch is characterized by the higher value of wetting efficiency due to better liquid spreading and these trends are properly captured in predictions (Figure 5.10).

In Chapter 4, it was shown that the extent of hysteresis in trickle flow is uniquely determined by the value of pressure drop obtained when the Levec prewetting mode is used (see Figure 5.11-a). All the data for f_H fall on one line despite the fact that they correspond to

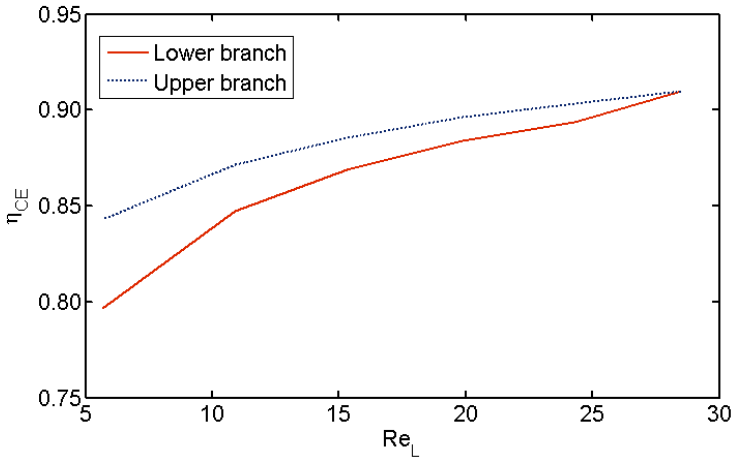

Figure 5.10. Simulated volume averaged value of wetting efficiency for the lower and upper branch of hysteresis loop. U_G=27 mm/s, P=1 barg. $\theta=30^0$ for upper branch and $\theta=43^0$ for lower branch.

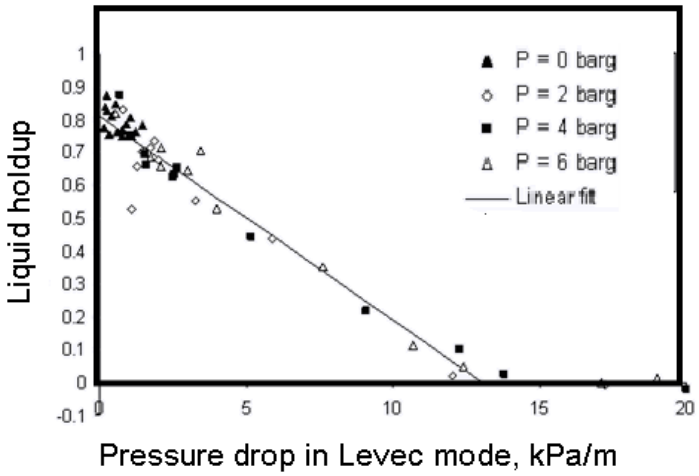

(a)

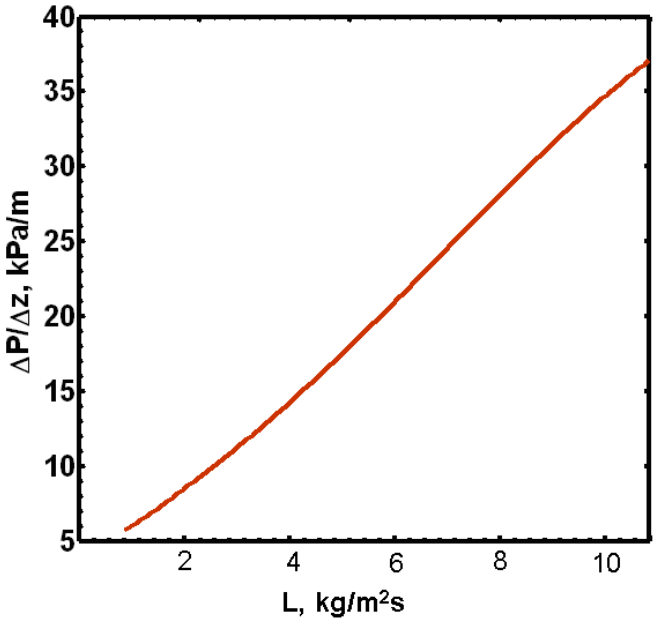

(b)

Figure 5.11. (a) Experimental results for dependence of hysteresis factor on pressure drop gradient in Levec mode. (b) Simulated pressure drop gradient for the Levec mode for the conditions typically encountered in industrial TBRs: d_p=1.9 mm, ρ_{oil}=850 kg/m^3, ρ_{gas}=3.5 kg/m^3, μ_{oil}=0.01Pa.s, μ_{gas}=1.5.10^{-5} Pa.s, 0.1 kg of gas per kg of oil introduced at the inlet of the reactor.

vastly different operating conditions (pressure, gas and liquid velocity) when plotted against pressure drop in Levec mode. Pressure drop data for the other prewetting modes do not show this trend.

The Levec prewetting mode is achieved by thoroughly prewetting the bed, draining it and then setting the operating values of gas and liquid flow rates. Hence, the pressure drop in the Levec mode is closely related to the values of the lower hysteresis branch. (Lower branch is obtained by first prewetting the bed, draining it and then gradually increasing liquid velocity until preset maximum liquid velocity is reached).

Therefore, the developed CFD model is used to predict values of pressure drop in a Levec prewetted bed by using the value of $\theta=43^0$ similarly to the simulation of lower hysteresis branch above. Then, the corresponding extent of hysteresis is read of the Figure 5.11-a. It is instructive to use this methodology to deduce the values of liquid flux that lead to negligible values of extent of hysteresis. As discussed, TBR are commonly used in oil processing for various operations generally termed as hydrotreating (hydrogenation, hydrodesulphurization, hydrodenitrogenation, hydrocracking etc.). Typical operating conditions for industrial TBR are given in Table 5.6 and used to simulate values of Levec pressure drop.

Table 5.6 Simulation parameters for results in Figure 5.11

Particle diameter, mm	1.9
Oil density, kg/m^3	850
Oil viscosity, Pa.s	0.01
Hydrogen density, kg/m^3	3.5
Hydrogen viscosity, Pa.s	$1.5 \cdot 10^{-5}$
kgH_2 per kg oil introduced	0.1

In Figure 5.11 gives the predictions as a function of liquid mass flux. Based on Figure 5.11-a, the negligible values of the extent of hysteresis are achieved if the pressure drop gradient is at least about 15 kPa/m. For the conditions of simulation (Table 5.6) this is achieved for the $L>3.5$ $kg/m^2/s$. If liquid mass flux is higher than 3.5 kg/m^2s, the startup mode will not significantly affect the resulting hydrodynamic parameters (e.g., pressure drop and liquid holdup). However, if liquid mass flux is lower than 3.5 kg/m^2s the performance can be influenced by the start-up mode.

5.4.4 Conversion for gas and liquid limited reactions

In this section, we demonstrate the use of developed reactive flow CFD model for the TBR performance assessment. We examine the application of the model for two classes

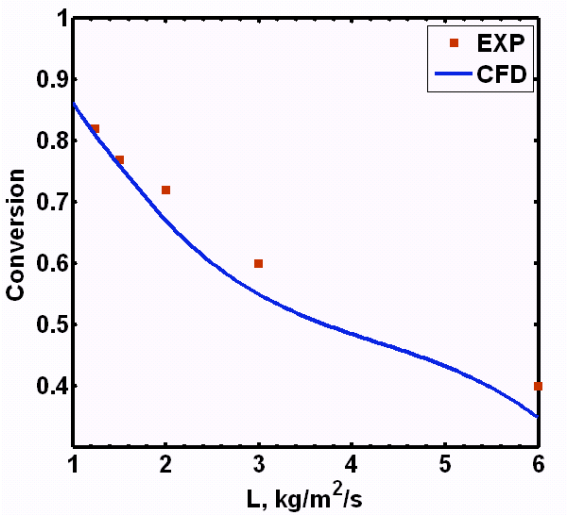

(a)

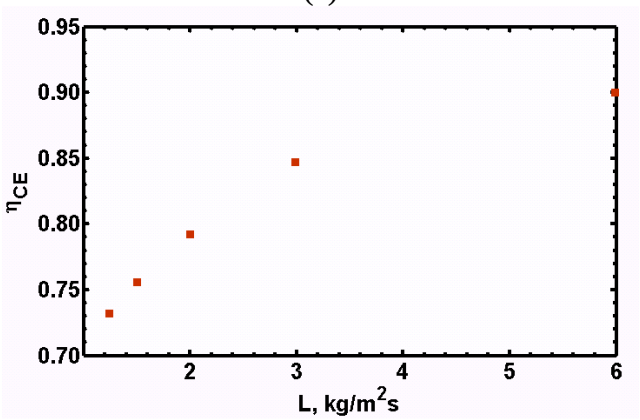

(b)

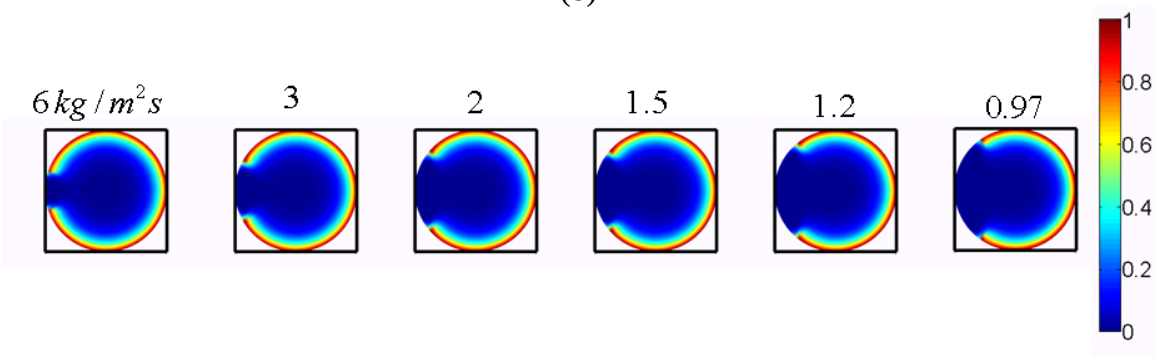

(c)

Figure 5.12. Assessment of CFD model for liquid limited reaction: (a) conversion, (b) wetting efficiency, (c) dimensionless particle scale concentration. Experimental data of Wu et al., 1996 for decomposition of hydrogen peroxide.

of reactions: (i) liquid limited, and (ii) gas limited reactions (Mills and Dudukovic, 1979; Mills et al., 1981; Beaudry et al., 1987, and Wu et al., 1996).

As an example of liquid limited reaction, we use the experimental study performed by Wu et al., 1996. The authors examined the decomposition of hydrogen peroxide on 1/16" copper chromite catalyst and reported dependence of conversion on liquid mass flux. In Figure 5.12-a the calculated and experimental values of conversion are shown. The predicted wetting efficiency is shown in Figure 5.12-b. Dimensionless particle scale concentration profiles for different values of liquid mass flux are given in Figure 5.12-c. As expected, the wetting efficiency increases with the increase in liquid mass flux (Figure 5.12-b). However, due to significant intraparticle diffusion limitations, the increase in wetting efficiency, even though evident in Figure 5.12-c, does not improve catalyst utilization. The value of catalyst effectiveness factor remains close to 0.2 for all cases in Figure 5.12-c. The error in predictions involves uncertainty in predicted flow field and liquid distribution; this contribution to the error decreases with increase in liquid flux. The prediction of wetting efficiency is subject to errors in flow field prediction and the uncertainty in used correlation (Al-Dahhan and Dudukovic, 1995, Table 5.5). Mass transfer parameters (Table 5.5) are also sources of errors. However, it can be stated that agreement is satisfactory and that developed method of coupling hydrodynamic solution with exact particle scale solution yields reasonable prediction for the case of liquid limited reaction.

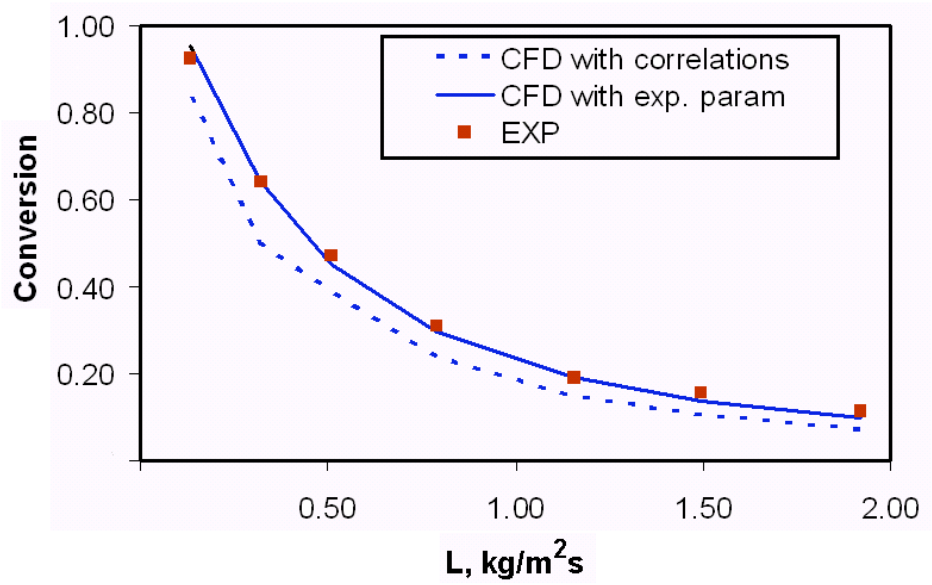

Figure 5.13. Assessment of CFD model for gas limited reaction – comparison of experimental and calculated conversion. Experimental data of Mills et al., 1984 for hydrogenation of α-methylstyrene. Dashed line represents CFD results obtained using correlations in Table 5.5 for mass transfer parameters. Solid line represents CFD results obtained using experimental value of effective and molecular diffusivity.

As an example of gas limited reaction, we use the experimental study on hydrogenation of α-methylstyrene performed by Mills et al., 1984. In Figure 5.13, the calculated and experimental values of conversion are shown. The dashed line represents the CFD results obtained using correlations in Table 5.5 for mass transfer parameters. The solid line represents the CFD results obtained using experimental value of effective and molecular diffusivity. Both lines show satisfactory agreement with predictions, but, as expected, use of experimental values significantly improves the model predictions.

5.5 Summary

Three-dimensional Eulerian CFD model is developed and setup in Fluent. Porosity distribution in a bed of extrudates has been experimentally characterized and used to implement the local porosity values in the CFD grid. Phase interaction closures are based on the model of Attou et al., 1999, and the principles of statistical hydrodynamics (Crine et al., 1992). In this way, a conceptualized picture of the two phase flow through packed beds as the combination of rivulet and film flow is introduced into the CFD framework. The contribution of each flow pattern depends on the operating conditions, packing wetting characteristics and the flow history of the bed. Model has been assessed against experimental data for liquid holdup, wetting efficiency and pressure drop hysteresis and, in general, satisfactory agreement is achieved. Further improvement should be directed towards more accurate capturing of the liquid channeling present at lower values of liquid mass velocity.

Our hydrodynamic Eulerian CFD model is then used together with species balance to yield TBR performance assessment. This reactive flow study addressed gas and liquid limited systems and for each case a closed form approach of coupling bed and particle scale solution within CFD framework was presented. Model predictions have been assessed against experimental data for conversion and show correct trends with operating variables and satisfactory agreement with conversion data.

Chapter 6
Overall Conclusions and Recommendations

In this work, the hydrodynamics of two phase flow in packed bed was investigated both experimentally and theoretically. The hydrodynamic model was then extended into a reactive flow model and its applicability for reactor design was demonstrated. The main points of this research and its possible extensions are summarized in this section.

6.1 Flow Distribution Studies

The flow distribution in a high pressure TBR has been experimentally investigated with a two fold objective: (i) to examine the quality of liquid phase distribution in a high pressure system and to provide results in terms of two criteria: distribution of the effluent liquid fluxes and cross-sectional liquid holdups; (ii) to examine the individual trends in these distributions and their relation with respect to the operating conditions of the high pressure system. A high pressure TBR was designed and installed together with the system for collection of the effluent liquid fluxes. The flow system was also imaged using computed tomography (CT) unit to provide characterization of bed porosity and the distribution of the flowing phases.

The experimental results have shown that the porosity distribution in the bed of extrudates (used in this study) follows the Gaussian distribution. The standard deviation of about 14-15% was obtained. The data on porosity distribution is important as the input to the theoretical and computational models such as the Eulerian CFD model developed in this study.

Based on the general literature concerning high pressure trickle bed reactors it was expected that both liquid holdup and effluent liquid fluxes would become more uniform with the increase in pressure, and gas or liquid mass velocity. Such anticipated results have been obtained only for the effect concerning liquid velocity. No pronounced trend was observed with respect to operating pressure. This can be attributed to the lower span of operating pressures used in this study as compared with typical high pressure TBR uses. An interesting result has been obtained for the effect of increase in gas velocity in the region of lower liquid velocities. The results indicate the improvement in the effluent fluxes distribution and deterioration in the cross-sectional liquid holdup distribution with the increase in gas velocity. A possible explanation rests on the flow segregation that occurs for the lower values of liquid velocity. In this case, there are zones of high and low liquid holdup in the reactor. In the regions of low liquid holdup there is less resistance to gas flow and hence these regions will have higher gas velocity and higher liquid velocity (induced by gas-liquid shear). The opposite holds for the regions of higher liquid holdup. This fact can explain the difference in the trends of the maldistribution factors defined based on liquid holdup and effluent liquid fluxes.

Further study is recommended to fully elucidate this phenomenon. It is evident that full characterization can only be performed if both holdups and liquid velocity distribution are obtained simultaneously (e.g., using MRI). Also, a phenomenological model is needed to account for the effect of flow segregation (in case of low liquid flux value) on the liquid distribution.

6.2 Extent of Hysteresis in Trickle Flow

A direct extension of the flow distribution study was the experimental study of pressure drop hysteresis in a high pressure TBR. Many studies have shown that increased operating pressure affects the flow distribution and wetting efficiency, and we extended such studies to encompass the effect of elevated operating pressure and other flow conditions on the extent of hysteresis. The extent of hysteresis was found to be a strong function of gas and liquid operating flow rates as well as the operating pressure. In the region of lower liquid velocities, hysteresis is present regardless of the operating pressure or gas velocity. In the region of higher liquid velocities, increases in both pressure and gas velocity lower the extent of hysteresis. For the range of conditions considered in this study the extent of hysteresis was uniquely determined by the pressure drop in bed subjected to the Levec prewetting mode. The experimental results indicate negligible extent of hysteresis when pressure drop in a bed subjected to Levec prewetting mode is higher than about 15 kPa/m. The developed CFD model (discussed below) was then used

to assess liquid fluxes that would lead to existence of hysteresis in a typical industrial use of TBR (i.e., hydrodesulphurization in oil processing). It was demonstrated that if L>3.5 kg/m^{2}s, the hysteresis effects will be negligible.

The future work in this area should be targeted at the development of models that account for hysteresis phenomena. It would be instructive to provide more elaborate analysis of the conditions leading to hysteresis free operation for the set of suitably chosen industrial processes. In principle, considering possible startup modes *in industrial reactors* and extending principles developed in this study can help improve industrial reactor performance.

6.3 Computational Fluid Dynamics Model of Trickle Flow

Three-dimensional Eulerian CFD model is developed and setup in Fluent. The experimental results for porosity distribution were used to implement porosity in the CFD grid. Phase interaction closures are based on the film model, and the principles of statistical hydrodynamics. Model has been assessed against experimental data for liquid holdup, wetting efficiency and pressure drop hysteresis and, in general, shows satisfactory agreement.

However, the model does not capture the occurrence of liquid channeling for the case of lower liquid flux (generally, $L<4$ kg/m^2/s). Further improvement can only be achieved by more elaborate closures.

Hydrodynamic Eulerian CFD model is then used together with species balance to yield TBR performance assessment. Reactive flow study addressed gas and liquid limited systems and for each case a closed form approach of coupling bed and particle scale solution within CFD framework was presented. Model predictions have been assessed against experimental data for conversion and show satisfactory agreement.

Further studies should lead to development of numerical techniques for the coupling of hydrodynamics and reaction terms for the case of non-linear kinetics and noisothemral conditions. The model should be applied to other industrially relevant systems such as use in oil fraction processing.

Appendix A
From Laboratory to Field Tomography: Data Collection and Performance Assessment

1. Introduction

Tomographic measurements enable a better understanding of the hydrodynamics of a given two-phase or multi-phase system and allow visualization of phase distributions in such a system. Transmission tomography uses measured signals emitted from a point source and attenuated through a domain to computationally determine a sectional image of the phase distribution in the system. Particularly appealing is that these techniques are not hindered by the opaque character of the process equipment and, in effect, are able to provide ‘an eye’ in an opaque flow. Tomographic techniques are now being widely used as laboratory investigative tools for the study of multiphase flow reactors. They enable a high quality, high spatial and/or temporal resolution of the flow and phase patterns and help improve the existing theoretical insights as well as lead to new ones (Barigou, 2004; Chaouki et al., 1997b; Boyer et al., 2002; Reinecke et al., 1998; Gladden and Alexander, 1996, and Kumar and Dudukovic, 1997).

A natural extension to these studies is the use of non-invasive imaging techniques in industrial systems. Reactor performance is critically dependent on mixing (e.g., stirred tanks and other back-mixed systems) or the lack of longitudinal mixing (plug flow reactors). In general, mixing problems are exacerbated at larger (production) scale, and this affects production rates and selectivity. Production and manufacturing equipment does malfunction, and such occurrences can be difficult to detect without good diagnostic measurements. For example, flow maldistribution in a separation column or reactor can severely and adversely affect plant performance (technical and economic) unless it is promptly diagnosed and corrected. There is therefore interest in utilizing non-invasive imaging techniques for diagnosis of operating units on manufacturing sites. This places demands on the technique regarding portability and resolution that are different to those encountered in research (Stitt and James, 2003).

Tomographic techniques can be broadly classified based on the type of signal used as electrical and radiation based tomography methods. The electrical methods include electrical resistance (ERT), electrical impedance (EIT) and electrical capacitance (ECT) tomography. Electrical tomography techniques recently have gained prominence as they offer a high temporal resolution (at the cost of spatial resolution) in the images and have been applied to industrial-scale vessels (Mann et al., 1997). However, the technique has field limitations. Although the technique is non-invasive to the flow in the domain all of resistance, capacitance and impedance tomography require that sensors to be in direct contact with the process fluid and is therefore invasive.

Sensors associated with X-ray and gamma-ray tomography methods do not require contact with the flow in any form and therefore present an attractive choice. The radiation source required for X-ray tomography needs electrical power for operations. These usually emit photons of low energy (soft source) which is not favorable when dealing with large cross sections of field vessels and the metal components associated with it. High energy X-ray sources used on pilot scale laboratory applications (Toye and Marchot, 2005) might not be suitable for field applications due to portability issues.

Gamma ray sources, a key component to gamma ray tomography, are prevailing in the field and industrial applications as a signal source. They are used as a level gauge in large opaque vessels to track the liquid level, for densitometry measurements, for diagnosing obstructions in flow, and in radiography applications (to determine the integrity of joints, wields, and metal structures). Gamma ray tomography is favorable for field applications as the source produces high energy photons that can be used for large cross sections, and it does not require electrical power for operation of the gamma photon source. The prevalent practice of using gamma ray sources for other applications in the field makes it more readily available for tomography applications.

The discussion above is summarized in Table A.1, where the basic requirements of laboratory and field tomography are compared. As shown, the requirements of portability and applicability to vessels with thick metal walls restrict the choice of the modality to

gamma-ray computed tomography (CT) which is suitable for opaque, high attenuation media, large cross sections, and steady state flow conditions.

Table A.1. Laboratory and field tomography priorities

Tomography Technique	Laboratory priorities		Field tomography priorities	
	Resolution		Transportable?	Applicable to thick metal wall vessels?
	Spatial	Temporal		
Gamma-ray	Good	Some	Yes	Yes
Positron emission	Good	Moderate	No	Yes
X-ray	Good	Some	Moderate	Moderate
Electrical capacitance	Moderate	Excellent	Yes	No
Optical	Good	Good	Yes	No
MRI	Good	Good	No	No

The use of this technique in the laboratory setting is well established (see for example, Kumar et al., 1997b; Boyer et al., 2005; Roy et al., 2004; Kumar et al., 1997a; Khopkar et al., 2005, and Bhusarapu et al., 2006). Tomography and velocimetry have been widely applied to the study of multiphase reactor systems. There are numerous reports of tomography using various techniques such as γ-ray fan beam tomography (Chen et al., 1998), γ-ray densitometry (Shollenberger et al., 1997) and electrical capacitance tomography (Benneet et al., 1999) and radioactive particle tracking (Chen et al., 1999) for slurry bubble columns as well as γ-ray tomography of a monolith reactor (Cartolano, 2002) and trickle beds (Boyer and Fanget, 2002), all applied to "large vessels" (up to 0.6

m diameter) in controlled, laboratory-type or cold-flow pilot scale environments. These studies yield fundamental data and knowledge that can be used to develop and validate reactor models.

Darwood et al., 2003 describe the development and set up for a field γ-ray tomograpic system. The data demonstrate the benefits of a fan-beam approach over a parallel path method. The described preferred approach is to position the source of gamma-radiation on one side of the vessel and a set of radiation sensors horizontally opposite in a fan arrangement. These source and sensors are moved around the vessel and the intensity of radiation transmitted through the vessel is recorded by the sensors for each source location. The sensors are not collimated, and peak counting is shown to have negligible effect on the quality of the tomogram.

Typically, when carrying out tomographic studies in the field, the conditions are considerably different to those encountered in the laboratory research environment. The access to the vessel is frequently restricted, there is a need to adjust the tomography set up to accommodate the column external piping and instrumentation and to carry out studies at significant heights on a large diameter column with high density (high attenuation) media (Darwood et al., 2003). The key driver in field tomography is commonly diagnostic in nature; the need is to obtain the data with sufficient resolution to establish any severe mal-operation at minimum cost.

It is important to assess what level of information is required. Diagnosis of good, adequate or poor operation can often be done with little measurement and information, provided you know what data to measure and how to interpret them. Detailed measurement will only be done in the field where it is essential, or more to the point where it adds significant value.

The 80:20 rule states that 80% of the information is only 20% of the cost of the full information, and that the 80% is normally sufficient to make an educated decision or diagnosis. A corollary to this is that 80% of the information and learning is achievable with only 20% of the full data set. This may be approximated by saying that adding an extra physical dimension, or increasing accuracy by one significant figure has nearly an order of magnitude effect on the cost. This begs the essential questions of what degree of resolution is required and how many measurements are required to achieve a tomogram that is adequate and sufficient.

There is little information in the process literature on the reliability of tomographic measurements at low measurement densities. Murphy and York, 2006 present an interesting discussion of this for the more complex situation of soft field techniques where data density is inherently a function of radial location. Attempts are also reported on how to cope with conditions of “sparse” or incomplete data, largely using sinogram techniques, to extrapolate into the data sparse regions (Constantino and Ozanyan, 2008, and Bertram et al., 2009). In the present context, the latter does not seem a satisfactory

approach as a key consideration is whether, by misfortune, the particular feature for diagnosis lies within the data sparse region and model based extrapolation of data external to that region may inherently not be successful. Darwood et al., 2003 report qualitatively findings from and empirical study with γ-ray tomography, using a relatively simple least squares based reconstruction technique, on the minimum requirements to observe certain features represented by phantoms.

The key difference between the set up described by Darwood et al., 2003 and the various tomographic systems described for laboratory scale work is in the number of line density measurements taken. Taking Roy et al., 2004 as representative of a laboratory system, the total number of scans completed for a planar tomogram is about 17,000. Contrast this with Darwood et al., 2003, who refer explicitly to completing a tomogram on a 6.2 m diameter distillation column with only 6 line density measurements from each of 32 detector positions; a mere 192 line densities. While the full study has clearly been invaluable in developing a methodology for the commercial tomography product, there is clearly a need and opportunity for a more detailed and fundamental study to better understand the relationship between measurement density and available information, and the impact of the reconstruction algorithm.

In this study, we use a research gamma ray tomography system to better understand the field diagnostics systems. A large set of gamma photons transmission (projection) data through a known phantom is gathered using the research tomography system. This set is

processed into small segments that represent the typical amount of projection data gathered in the field tomography system. The aim is to assess what level of information is required for the purpose of field diagnostics and which methodology of data collection would help minimize the needed projection data. We also discuss the theoretical framework for such assessment and substantiate our findings with the experimental section of the work.

This chapter is organized as follows. We first describe basic process of projection data collection for our research gamma-ray tomography unit and typical field use. Next, we review the employed image reconstruction procedures, and projection data processing followed by the details of the theoretical methodology for the assessment of scanner performance. Lastly, the results of the image reconstruction are presented, and it is demonstrated how the theoretical framework can be used to guide the projection data collection methodology in a field scanner.

2. Background

Laboratory gamma-ray CT scanner

The principal schematic of the gamma-ray CT source-detector arrangement used in this work is given in Figure A.1. The imaged object is positioned between the source and an array of seven NaI (2’ diameter) detectors. A 100mCi ^{137}Cs point gamma-ray source

provides a 40^0 fan beam in the horizontal plane. In order to obtain line (projection) attenuation measurements the detectors are shielded and equipped with the 2 mm x 2 mm collimators. During the experiment, the source and detectors take different positions relative to each other and to the column, and at each of these positions attenuation of the incident radiation is recorded. Within one fixed source position (view) any given detector takes 25 different positions (projections) in increment of 0.2^0. Hence, there are 175 projections per each view. The source makes a full circle around the scanned object in increment of 3.6^0, i.e., there are 100 views in one scan. Thus, the total number of projections that are being considered is 17,500. For more details about the hardware and the data acquisition system the reader is referred to Kumar, 1994, Kumar and Dudukovic, 1997, and Roy, 2006. Also, more details are available in the Appendix C below.

Both scanning and reconstruction are the essential parts of the process of image formation. The development and use of the reconstruction algorithms is a broadly studied topic. We only provide a brief review of various approaches and give more details for the reconstruction algorithms employed here.

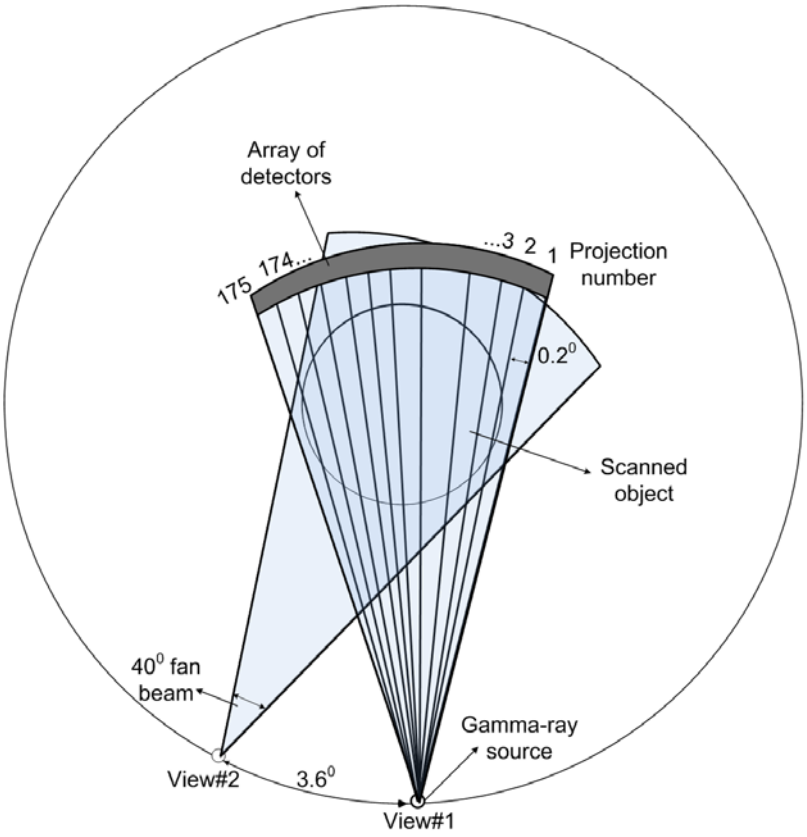

Figure A.1. Principal schematic of laboratory gamma-ray computed tomography scanner

Reconstruction algorithms

The expectation maximization (EM) (Dempster et al., 1977, and Lange and Carson, 1984) and the alternating minimization algorithm (AM) (O'Sullivan and Benac, 2007) are both reconstruction methods that model the stochastic nature of gamma-ray emission. They are expected to yield improvement in the reconstruction quality as compared to the Fourier techniques (Patel et al., 2007, and Varma et al., 2008) and iterative algebraic methods such as the incorporation of non-negativity constraints, and objective measure of

quality of reconstruction (Lange and Carson, 1984). The EM algorithm is discussed in details in Appendix C. Hence, here, only AM algorithm is described.

AM algorithm

AM algorithm (O'Sullivan and Benac, 2007) is an iterative procedure that utilizes the concept of I-divergence (Csiszar, 1991) to obtain a maximum-likelihood (ML) estimate. I – divergence is a measure of entropy, or discrepancy between two stochastic entities. As in the case of the EM algorithm, discussed in Appendix C, the Beer-Lambert's law, equation (1), is used to model the transmission of photons through the domain

$$q_i^{(n)} = \lambda_i \exp(-\sum_{j \in I_i} l_{ij} \mu_j^{(n)}). \tag{1}$$

The relative entropy between the model and the measured signal is minimized when the model accurately represents transmission of the gamma ray photons (measured signal) through the domain. In the AM algorithm I-divergence is used to assess the discrepancy between the model vector ($\mathbf{q}$) and the observation vector ($\mathbf{d}$) and, for iteration *n*, it is given by equation (2).

$$\mathrm{I}^{(n)}\left(\mathbf{d} \,\|\, \mathbf{q}^{(n)}\right) = \sum_i \left\{ d_i \ln \frac{d_i}{q_i^{(n)}} - \left(d_i - q_i^{(n)}\right) \right\} \tag{2}$$

The objective of the reconstruction is to find $\boldsymbol{\mu}$ such that that it minimizes the value of the I-divergence. As shown in O'Sullivan and Benac, 2007, the minimization of the equation (2) yields the following update function for $\boldsymbol{\mu}$:

$$\mu_j^{(n+1)} = \mu_j^{(n)} - \frac{1}{z_j} \ln \frac{\sum_i l_{ij} d_i}{\sum_i l_{ij} q^{(n)}}, \tag{3}$$

where z_j represents the scaling factor that is chosen such that equation (4) is satisfied for each pixel.

$$\sum_{j \in I_i} \left(\frac{l_{ij}}{z_j} \right) \leq 1 \tag{4}$$

The numerator and denominator terms within logarithmic term of the update function in equation (3) represent the back projections of the photon counts measured by the sensors, and the model vector $\mathbf{q}$ based on the current estimate of $\boldsymbol{\mu}^{(n)}$. The value of the scaling factor chosen for every pixel j, as long as equation (4) is satisfied, does not affect the rate of convergence or the final value of the vector $\boldsymbol{\mu}^{(n)}$ (Benac, 2005).

Two advantages of the AM algorithm over the EM algorithm (Appendix C) are evident. First, the derivation of the update function does not involve Taylor series approximation as introduced in the EM algorithm (Lange and Carson, 1984). The effects of the approximation are more pronounced when high attenuating materials (metal internals) are preset in the domain. This could lead to beam hardening and other image artifacts. Secondly, the I – divergence function has a non-negative property, and has a unique minima at zero. If the two functions described in equation (2) are equal the relative entropy reaches zero. This lower bound of the function at which the solution converges is

predefined regardless of the attenuation values and the strength of signals detected by the sensors (gamma counts). Hence the function is guaranteed to monotonically decrease and converge to a unique minimum. The upper bound of the maximum likelihood function used in the EM algorithm is not know a priori and is not uniquely defined. The upper bound represents the maximum value of the log likelihood at which the solution converges. It is dependant to attenuation properties of the flow which are not known a prior. This could lead to false convergence in ill conditioned applications.

3. Data collection and processing

Experiments are performed to obtain the full scan data set (17,500 projections using 100 views and 175 projections per view, as discussed in Appendix C) for phantom shown in Figure A.2. Phantom is designed to mimic rather typical diagnostics task in field tomography, namely, detection of maldistribution. In such a scenario, a zone of low density, and hence attenuation, is present within the otherwise high attenuation domain. Therefore, we designed our phantom with similar configuration. It consists of 6" outer diameter tube with a concentrically placed 3.25" diameter tube. Annular region between the tubes is filled with water. Inside the 3.25" tube a 1.25" diameter tube is placed 0.2" off-center and filled with water. All tubes are made of Plexiglas. Table A.2 gives the theoretical values of the linear attenuation coefficient for the regions indicated in Figure A.2. These values are used in the process of the calculation of the reconstruction error as per the procedure described below.

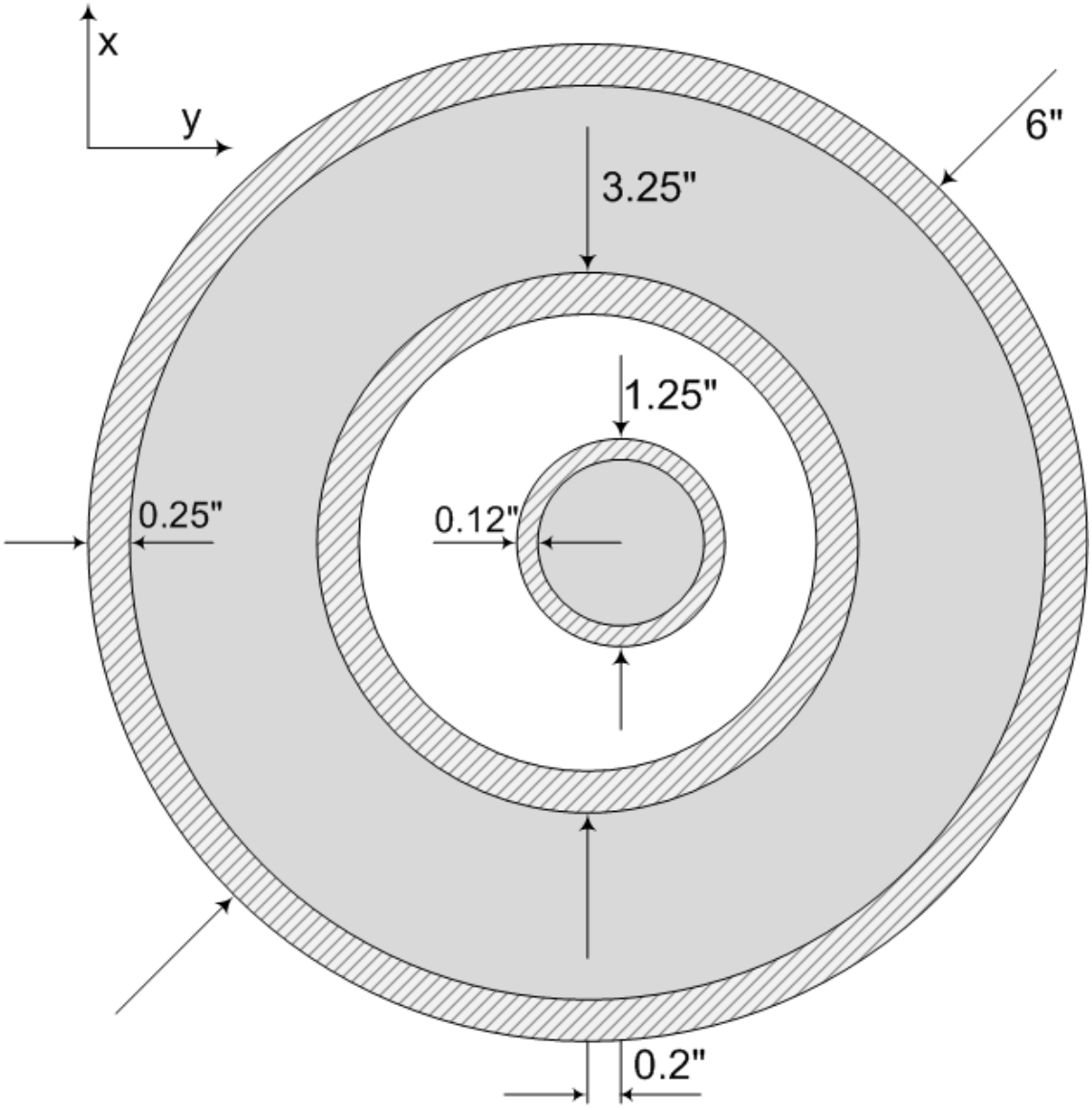

Figure A.2. Phantom object: Gray (A and C) regions are filled with water; white (B) region is empty. 1” diameter tube is positioned 0.2” off-center in the *y* direction. Theoretical values of the attenuation coefficients for regions A, B, and C are given in Table A.2.

TableA.2. Theoretical values of attenuation coefficient for the phantom object

Region of phantom	Medium	μ_{theor}, cm^{-1}
A	Water	0.086
B	Air	0.0001
C	Water	0.086

The data processing was designed to address the error behavior with the change in the pixel size, number of scan lines used, and the data collection procedure. Table A.3 shows the cases that are being considered. We consider the range of pixel sizes (ξ) from 1.7 to 7.6 mm. The number of scan lines was chosen to correspond to 5, 10, 25, 50% or 100% of the full scan. Hence, the corresponding total number of scan lines was 875, 1750, 4375 and 8750, respectively. We shall refer to the number of scan lines by its percentage value and use the symbol δ for it. For the prescribed value of δ, the influence of the data collection procedure was addressed by varying the number of projections per view $\tau \in \{49, 63, 91, 175\}$. Note that each case is uniquely identified by specifying the pixel size (ξ), the number of scan lines (δ) and the number of projections per view (τ). Naturally, for a fixed value of δ, the number of views decreases as τ increases. For example (Table A.3) one of the cases is given as follows. We consider the total of 875 scan lines and designate it as δ = 5% (0.05*17500=875). We choose τ = 175 which represents the number of projections for each view. Then, as shown in Table A.3 the corresponding number of views for this case is 5. Hence, we can retrieve δ as 5*175=875 total scan lines. Note that the case will be fully specified once the pixel size $\xi \in \{1.70, 1.90, 2.18, 2.54, 3.05, 3.81, 5.08, 7.62\}$ is designated. The number of views for

each case is given in Table A.3, however all the trends will only be reported with respect to the number of projections per view.

Table A.3. Cases considered in the image reconstruction

Pixels size (ξ), mm	Total number of scan lines considered (δ) , % of full scan	Number of views	Number of projections per view (τ)
1.70 1.90 2.18 2.54 3.05 3.81 5.08 7.62	5	5	175
		10	91
		14	63
		18	49
	10	10	175
		20	91
		28	63
		36	49
	25	25	175
		48	91
		69	63
		89	49
	50	50	175
		96	91

4. Characterizing scanner performance

Very important issue for tomographic scanner is the assessment of the image quality and scanner performance for a given method of image formation (Barrett, 1990). The image quality is defined as the measure of deviation of the estimate to the true object and is generally influenced by the object properties, imaging technique (e.g., x-ray, gamma-ray tomography, etc.), geometry and data collection method, sensors used, and reconstruction procedure employed.

The reconstruction performance can be assessed (and in principle, predicted) using the Fisher information (FI) concept. FI is a measure of information that an observable random variable **Y**, characterized by likelihood $\mathrm{p}(\mathbf{Y},\boldsymbol{\mu})$, carries about an unknown parameter vector $\boldsymbol{\mu}=\{\mu_1,\mu_2,...,\mu_N\}$ (van Trees, 1968):

$$\mathbf{F}_{\boldsymbol{\mu}}=\mathrm{cov}_{\boldsymbol{\mu}}\left\{\mathbf{S}\mathbf{S}^{\mathrm{T}}\right\}=\mathrm{E}\left\{\mathbf{S}\mathbf{S}^{\mathrm{T}}\right\}. \tag{5}$$

In equation (5), T denotes the transpose operation, cov is a covariance, and **S** is a score statistics:

$$\mathbf{S}=\frac{\partial \ln \mathrm{p}(\mathbf{Y},\boldsymbol{\mu})}{\partial \boldsymbol{\mu}}. \tag{6}$$

FI can be also calculated as (Lehmann and Casella, 1998):

$$\mathbf{F}_{\boldsymbol{\mu}}=-\mathrm{E}\left\{\frac{\partial^2}{\partial \boldsymbol{\mu}^2}\ln \mathrm{p}(\mathbf{Y},\boldsymbol{\mu})\right\}. \tag{7}$$

Hence, FI is an NxN matrix with the *km* element given by:

$$F_{km}=-\mathrm{E}\left\{\frac{\partial^2}{\partial \mu_k \partial \mu_m}\ln \mathrm{p}(Y_i,\boldsymbol{\mu})\right\} k,m=\{1,2,...,N\} \tag{8}$$

Here, we utilize equation (7) to define the content of information that the measured (projection) data (**Y**) carries about the values of attenuation coefficient ($\boldsymbol{\mu}$). Hence, we obtain the expected FI as

$$F_{km}=\sum_{i\in(J_k\cap J_m)} l_{ik}l_{im}\,\mathrm{E}\{Y_i\}, \tag{9}$$

where $i \in (J_k \cap J_m)$ designates all projections to which both pixels *k* and *m* contribute. To simplify the calculation of the elements of $\mathbf{F}_{\boldsymbol{\mu}}$, we utilize the experimental projection data (d_i) in place of the expected values $\mathrm{E}\{Y_i\}$ thus arriving at the *observed FI matrix* with the *km* element:

$$F_{km}^{obs} = \left(\sum_{i \in (J_k \cap J_m)} l_{ik} l_{im} \, \mathrm{E}\{Y_i\} \right)_{\mathrm{E}\{Y_i\} \to d_i} = \sum_{i \in (J_k \cap J_m)} l_{ik} l_{im} d_i \,. \tag{10}$$

For more details on distinction between FI, expected FI and observed FI see McLachlan and Krishnan, 2008. Further, we can describe the information content via Cramer-Rao bound (CRB), defined by equation (11), which gives a lower bound on the covariance matrix of any unbiased estimate for a vector of non-random parameters (Lehmann and Casella, 1998).

$$\mathbf{C}_{\boldsymbol{\mu}} = \mathbf{F}_{\boldsymbol{\mu}}^{-1} \tag{11}$$

The total information content (for the entire $\boldsymbol{\mu}$ vector) can be generalized as $\mathrm{tr}\{\mathbf{C}_{\boldsymbol{\mu}}\}$, where tr designates the trace operator (for example, see Gupta and Kundu, 2006). Lower values of $\mathrm{tr}\{\mathbf{C}_{\boldsymbol{\mu}}\}$ indicate that it is possible to achieve lower variances in the $\boldsymbol{\mu}$ estimate and thus designate better performance.

5. Results and discussion

Reconstructed images

As discussed, the objective of our case study is the detection of the low attenuation region embedded between two higher attenuation regions mimicking the typical case of

the maldistribution diagnostics. The reconstructed values of the linear attenuation coefficient are shown in Figure A.3 (EM algorithm) and Figure A.4 (AM algorithm). The images are given for the range of ξ (pixel size), δ (total number of scan lines used given as percentage of the full scan), and τ (number of projections per view) values. In the resulting images of the full set data, i.e., δ=100%, (Figure A.3-a and Figure A.4-a) higher and lower attenuation regions are clearly captured and separated. As δ decreases, the images deteriorate, and eventually become corrupted with artifacts. Further, for a fixed value of δ, the images clearly exhibit the dependence on τ. This can be verified by comparison of cases (b) and (c), (d) and (e), (f) and (g), and (h) and (i) in Figure A.3 and Figure A.4. We discuss these differences in more detail below.

Reconstruction error

The mean absolute percentage error is used to quantify the reconstruction error:

$$Error = \frac{100}{N}\sum_{i=1}^{N}\frac{\mathrm{abs}(\mu - \mu_{theor})}{\mu_{theor}}, \tag{12}$$

where N is the total number of pixels in the reconstructed image and μ_{theor} is the theoretical value of the attenuation coefficient (Table A.2). To compare the results obtained by the two algorithms it is necessary to have a common basis. For example, it is a known fact that with a higher number of iterations the image tends to get noisy and grains tend to appear (Snyder et al., 1992). Here, we adopted the following approach to exclude the effect of number of iterations from the analysis. The reconstructions are

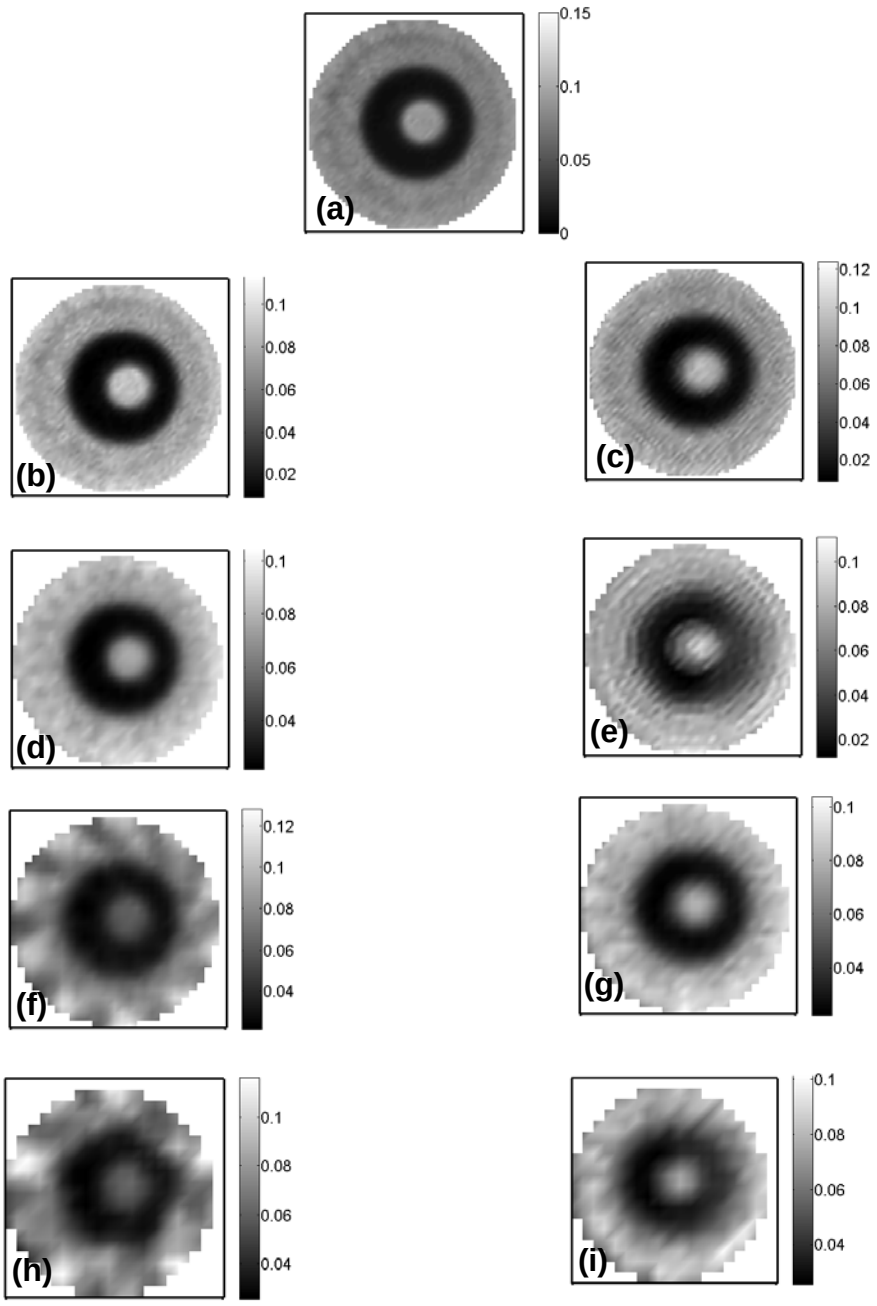

Figure A.3. Reconstructed images (EM algorithm). Colorbars indicate values of linear attenuation coefficient (cm^{-1}). (a) ξ=2.54mm, δ=100%, τ=175 projections per view (b) ξ=2.54, δ=50, τ=175 (c) ξ=2.54, δ=50, τ=91 (d) ξ=3.81, δ=25, τ=175 (e) ξ=3.81, δ=25, τ=49 (f) ξ=5.08, δ=10, τ=175 (g) ξ=5.08, δ=10, τ=91 (h) ξ=7.62, δ=5, τ=175 (i) ξ=7.62, δ=5, τ=49. See also Table A.3.

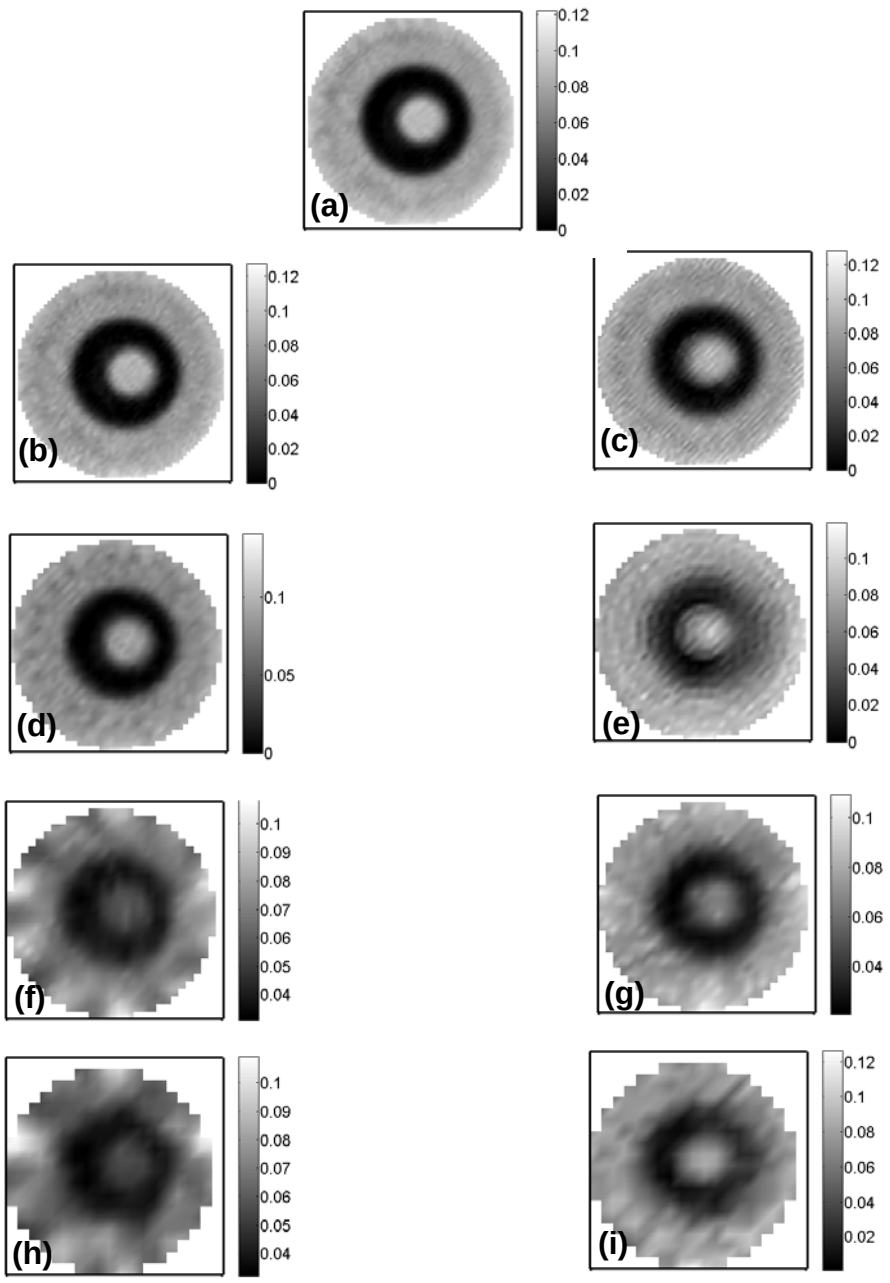

Figure A.4. Reconstructed images (AM algorithm). Colorbars indicate values of linear attenuation coefficient (cm^{-1}). (a) ξ=2.54mm, δ=100%, τ=175 projections per view (b) ξ=2.54, δ=50, τ=175 (c) ξ=2.54, δ=50, τ=91 (d) ξ=3.81, δ=25, τ=175 (e) ξ=3.81, δ=25, τ=49 (f) ξ=5.08, δ=10, τ=175 (g) ξ=5.08, δ=10, τ=91 (h) ξ=7.62, δ=5, τ=175 (i) ξ=7.62, δ=5, τ=49. See also Table A.3.

performed over a large span of iterations and, for each case, the error is taken as the minimal error within all the error values. This implies that the results presented here correspond to the ones obtained by the use of the optimal stopping criteria.

In Figure A.5, the reconstruction error is shown as a function of the number of total scan lines. All data points are for $\tau = 175$. The results indicate potential for significant reduction of the number of scan lines since the reconstruction error levels off at values of δ of about 25 to 50%. Hence, for the diagnostics purposes, increase in the number of scan lines above 50% (8750) or 25% (4375) does not bring any additional gain in the reconstruction process. Such decrease in the number of needed scan lines also gives the potential for the reduction of scan time.

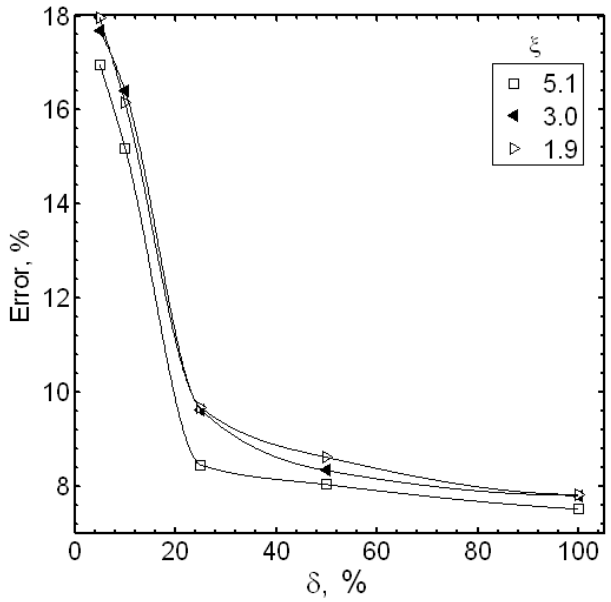

(a)

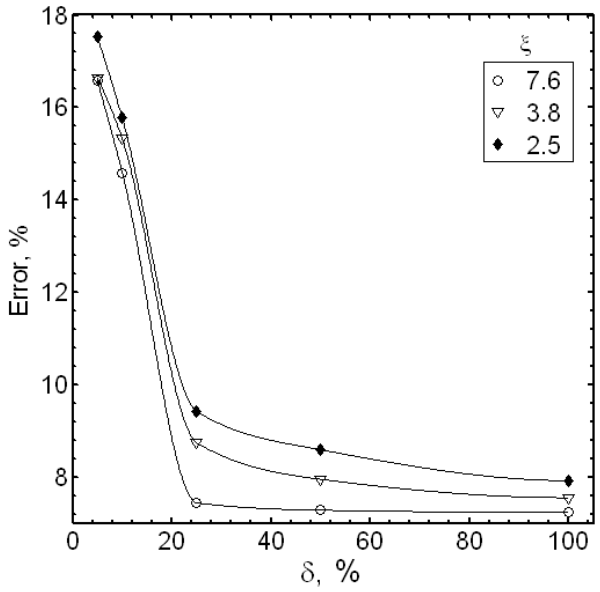

(b)

Figure A.5. Reconstruction error as a function of percentage of data used and pixel size (all data points are for τ=175, EM algorithm)

As shown in Figure A.6, the reconstruction error is a very complex function of parameters ξ, δ, and τ (Table A.3) and the algorithm employed. The results indicate the reduction of error with the increase in pixel size. Also, the error is very sensitive to the method of data collection, i.e., value of τ. However, no definite trends can be identified. For example, in Figure A.6 (e) and (f) (δ=25%), and (g) and (h) (δ=50%), error is a decreasing function of τ. In Figure A.6 (a) and (b) (δ=5%), most cases exhibit minimum error at τ = 63 with the exception of ξ=2.5 mm for which minimum error occurs for τ = 175. On the other hand, in Figure A.6 (c) and (d), τ = 91 yields the minimal

reconstruction error. We see these trends correctly reflected in Figures A.3 and A.4; images (b), (d), (g) and (i) better capture the phantom than images (c), (e), (f) and (h), respectively.

Generally, the AM algorithm outperforms the EM algorithm when reconstruction error is considered (Figure A.6). The differences are due to the approximation used in the derivation of the update function as discussed above. On the other hand, cross examination of the images shown in Figures A.3 and A.4, reveals that both the algorithms have a comparable capability of performing the objective of detecting low attenuation region.

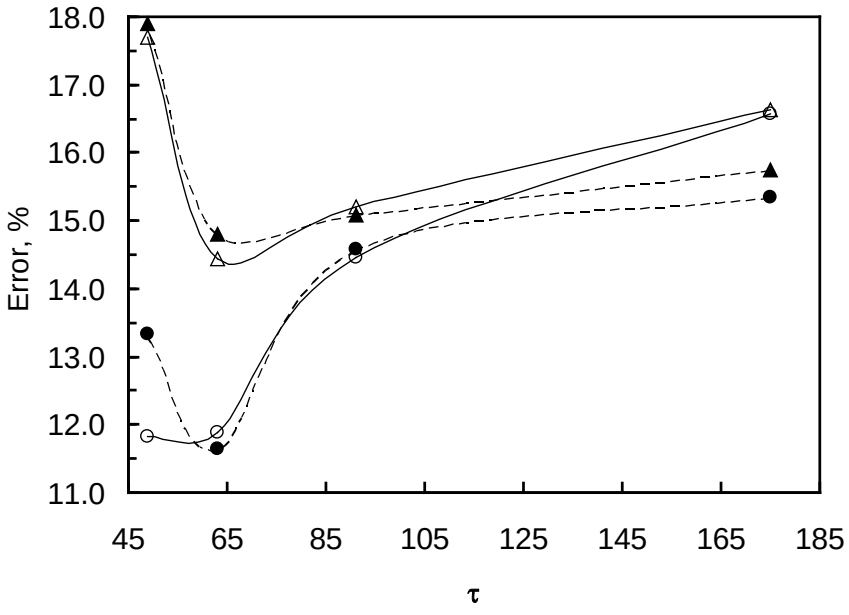

(a)

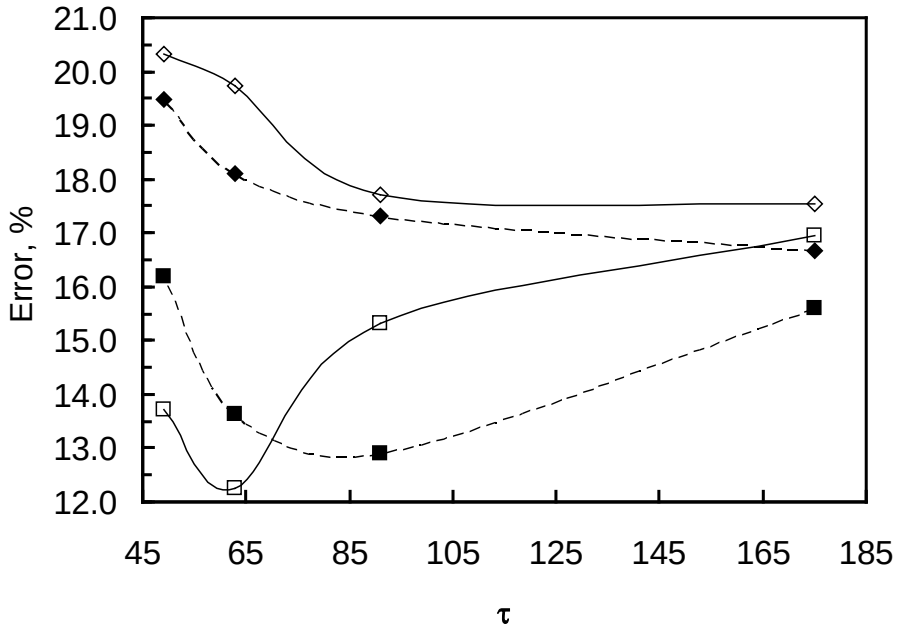
21.0
20.0
19.0
18.0
17.0
16.0
15.0
14.0
13.0
12.0
Error, %
45
65
85
105
125
145
165
185
τ

(b)

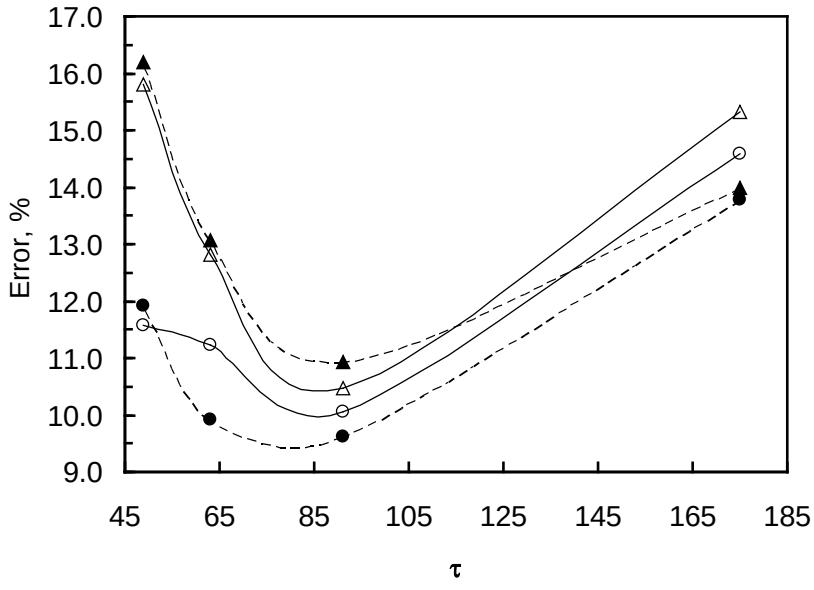
17.0
16.0
15.0
14.0
13.0
12.0
11.0
10.0
9.0
Error, %
45
65
85
105
125
145
165
185
τ

(c)

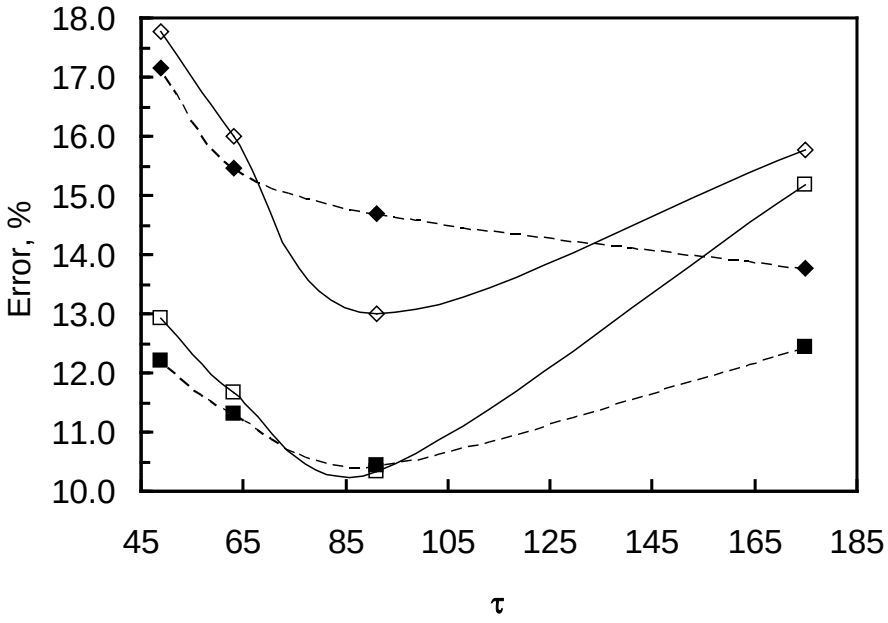
18.0
17.0
16.0
15.0
14.0
13.0
12.0
11.0
10.0
Error, %
45
65
85
105
125
145
165
185
τ

(d)

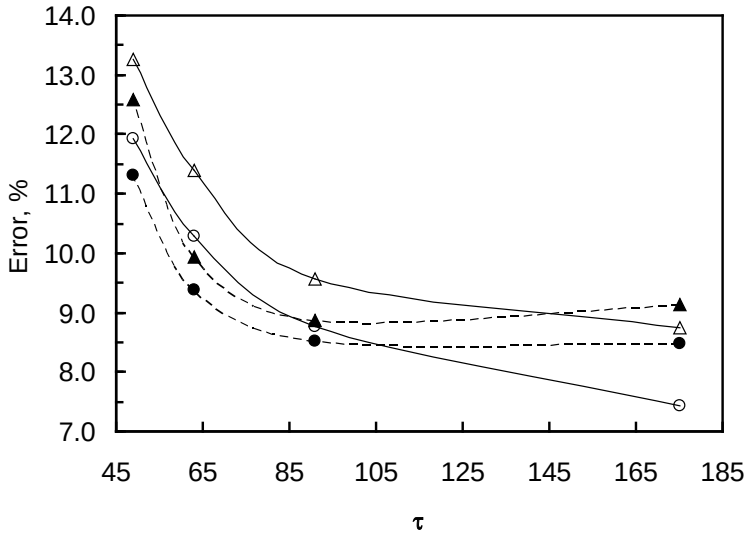
14.0
13.0
12.0
11.0
10.0
9.0
8.0
7.0
Error, %
45
65
85
105
125
145
165
185
τ

(e)

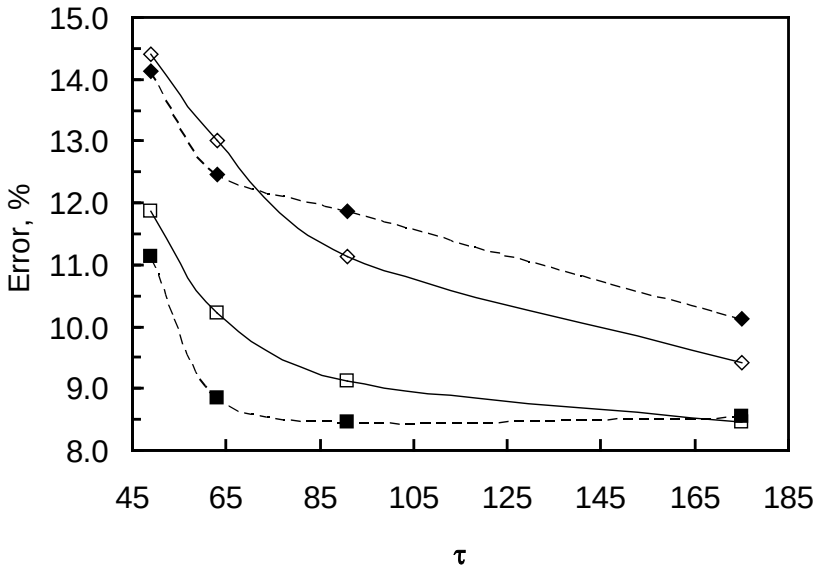
15.0
14.0
13.0
12.0
11.0
10.0
9.0
8.0
Error, %
45
65
85
105
125
145
165
185
τ

(f)

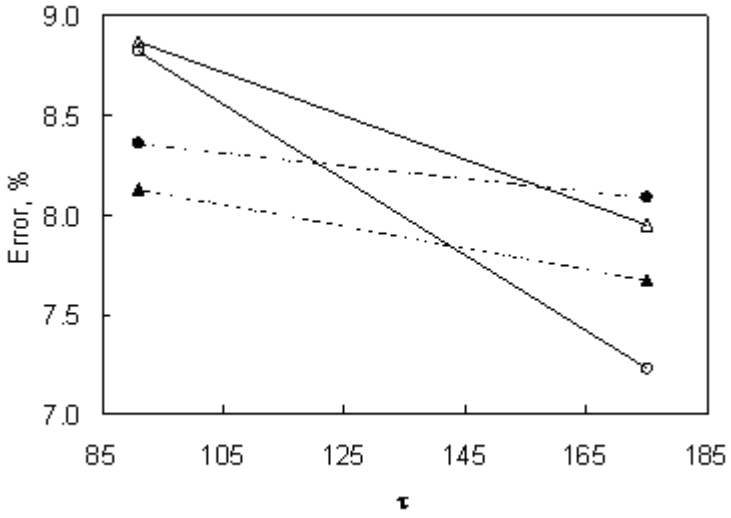
9.0
8.5
8.0
7.5
7.0
Error, %
85
105
125
145
165
185
τ

(g)

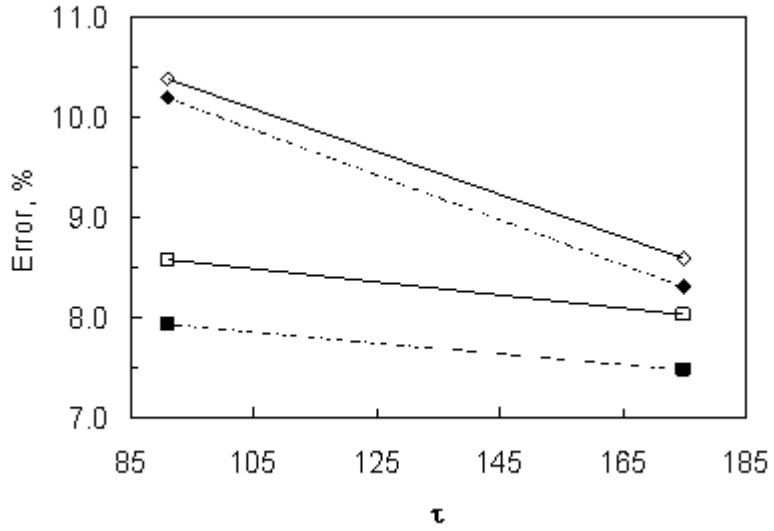

(h)

EM: ξ=7.6 mm, ξ=5.1, ξ=3.8, ξ=2.5

AM: ξ=7.6 mm, ξ=5.1, ξ=3.8, ξ=2.5

Figure A.6. Error of reconstruction for different total number of scan lines (δ). (a) and (b) δ=5%, (c) and (d) δ=10%, (e) and (f) δ=25%, (g) and (h) δ=50%.

Performance prediction

We first verify the developed total information content criteria $\mathrm{tr}\{\mathbf{C}_\mu\}$ (see also equations (10) and (11)) against the known resolution limit of the scanner. Roy, 2006, utilized the expression proposed by Yester and Barnes, 1977, and showed that for the scanner used in our study its value is about 2 mm. In Figure A.7, the quantity $\mathrm{tr}\{\mathbf{C}_\mu\}$ is shown as a function of pixel size. The sharp increase in $\mathrm{tr}\{\mathbf{C}_\mu\}$ at about ξ=2 mm is

evident and is coinciding with the resolution limit of the scanner. Hence, $\mathrm{tr}\{\mathbf{C}_{\mu}\}$ can properly capture the basic performance parameters of the scanner.

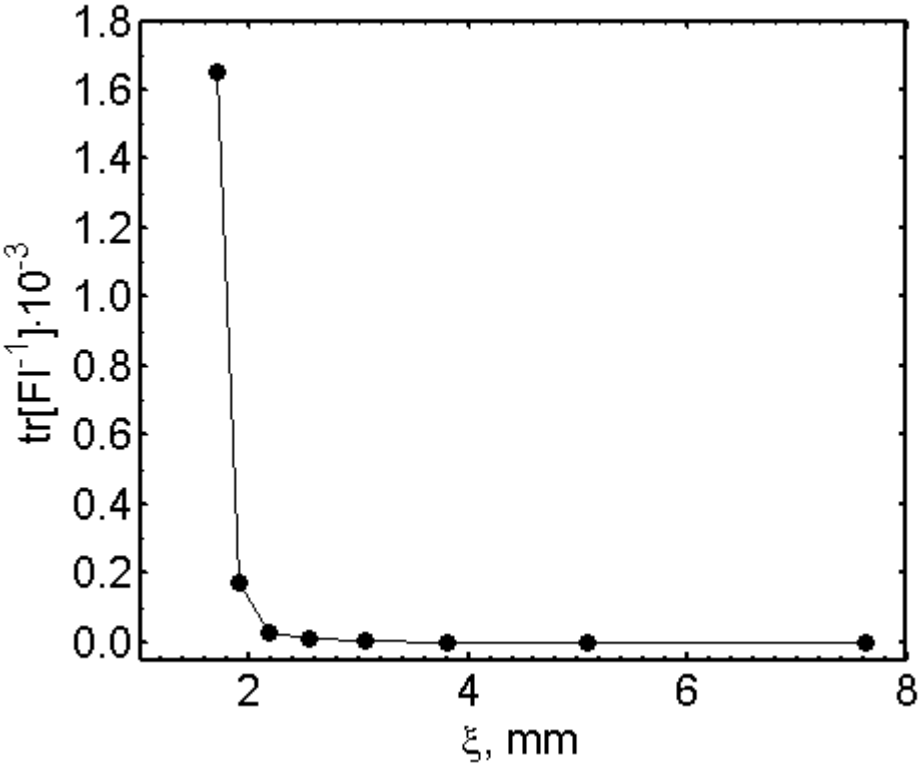

Figure A.7. Change in the information content with the pixel size. Full scan data (δ=100%, τ=175).

Similar analysis can be extended to clarify the intricate trends of the reconstruction error. As given by equations (10) and (11) the information content depends on the number of photons at detectors (i.e., scanned object properties) and the scanner geometry. Values of l_{ik} and l_{im} are a complex function of the pixels size, and the data collection arrangement (i.e, the values of ξ, δ and τ). Note that the calculation of $\mathrm{tr}\{\mathbf{C}_{\mu}\}$ involves the inversion of the NxN FI matrix (equation (11)) which becomes computationally intensive

for smaller pixel sizes. Even though there are iterative procedures designed to calculate $\mathrm{tr}\{\mathbf{C}_{\mu}\}$ for a specific region of interest (certain range of pixels in the image) at much lower computational cost (Hero et al., 1997), for simplicity sake, we limit our discussion to the lower resolution cases. This is reasonable as such cases are more relevant to the field diagnostics.

EM and AM algorithm are essentially characterized by the same information content since the model equation for AM is the same as incomplete data likelihood for EM. Note that this is also properly reflected in the similar trends of EM and AM reconstruction error. To simplify plot, we limit our remaining discussion to the use of EM reconstruction error.

Comparative plot of reconstruction error and $\mathrm{tr}\{\mathbf{C}_{\mu}\}$ is given in Figure A.8. Similarly to the trends exhibited in Figure A.7, $\mathrm{tr}\{\mathbf{C}_{\mu}\}$ progressively increases with the decrease in pixel size. The trends of reconstruction error are well reflected in the value of $\mathrm{tr}\{\mathbf{C}_{\mu}\}$ and it is possible to predict minimum of the reconstruction error using it. For example, for ξ = 7.6 mm and δ = 5%, $\mathrm{tr}\{\mathbf{C}_{\mu}\}$ takes values of about 10 and 700 for τ = 49

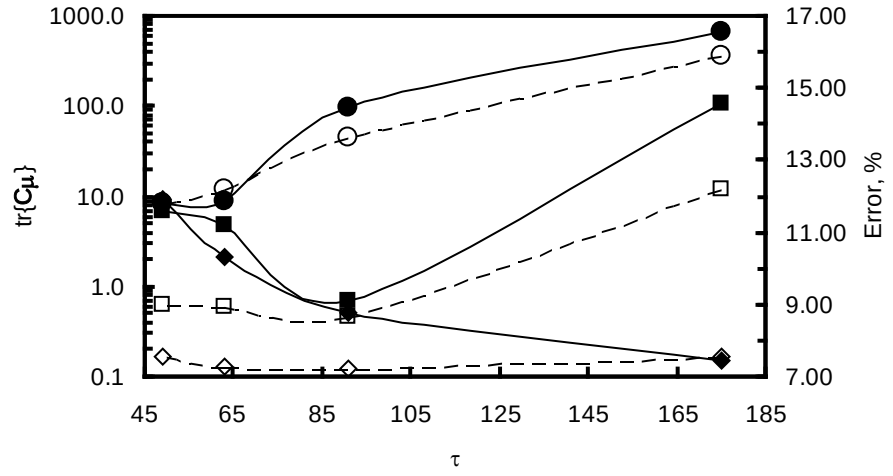

(a)

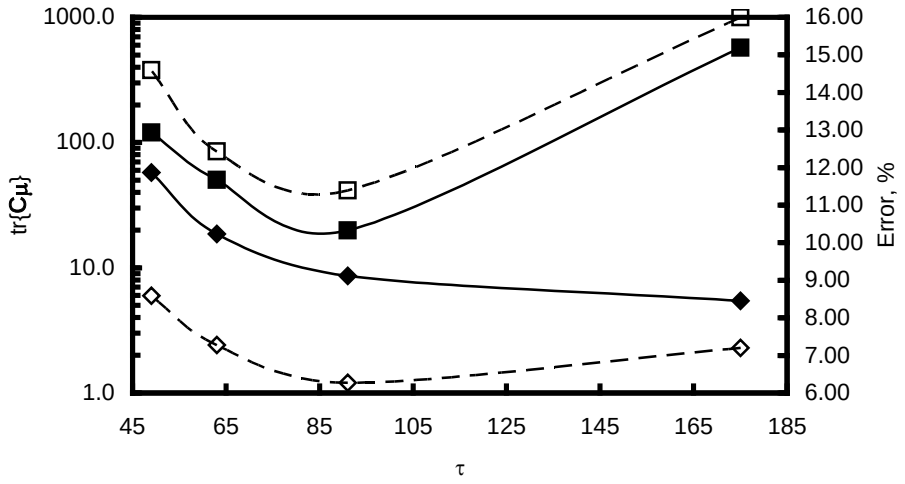

(b)

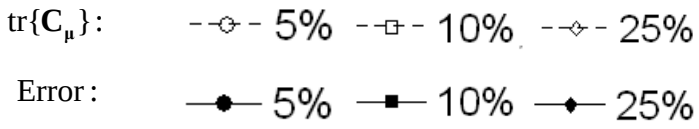

Figure A.8. Change in the information content and the reconstruction error with the number of projections per view (τ) for constant total number of scan lines (δ). (a) $\xi = 7.6$ mm (b) $\xi = 5.1$ mm.

and 175, respectively. For these cases, reconstruction error increases from 11.8 to 16.2%. $\mathrm{tr}\{\mathbf{C}_{\mu}\}$ is less sensitive to τ for higher values of δ.

In Figure A.8, the $\mathrm{tr}\{\mathbf{C}_{\mu}\}$ values also suggest that for a small number of line measurements (projections) (δ=5% and δ= 10%), lower values of $\mathrm{tr}\{\mathbf{C}_{\mu}\}$ are obtained when the number of views is increased and the number of projections per view (τ) is kept smaller. This observation is very pertinent to field tomography applications where there is a linear operating cost associated with the number of line measurements that can be made with a sensor array and a source. Information or images with greater accuracy could be obtained with fewer sensors and more views or source positions around the vessel to be scanned.

6. Summary

In this study, we examined the various aspects of gamma-ray tomography as a research and field diagnostics tool. Laboratory CT unit was used to gather high number of projection data which were then processed into smaller sets to mimic the field tomography conditions of low scan data. The aim was to assess what level of information is required for the purpose of field diagnostics and which methodology of data collection would help minimize the needed projection data. We presented theoretical framework, rooted in Fisher information concept, for the assessment of scanner performance. Such

framework was proven useful in capturing and predicting the behavior of reconstruction error.

It was further demonstrated that typical task of field diagnostics, i.e., detection of maldistribution, can be performed with the very limited set of projection data. In practice, the same number of projection data in field tomography can be obtained by either using the higher number of source positions around the object coupled with the lower number of scan lines for each source position, or vice versa. It was demonstrated that, in case of very low number of scan lines, the reconstruction performance was better for case of using higher number of sensor positions.

Appendix B
Operating Procedure for the High Pressure Trickle Bed Reactor

In this section, the design and the operating procedure for the high pressure trickle bed reactor are described. The additional aspects of the experimental procedure are discussed in Appendix C, i.e., the use of computed tomography unit for the phase holdups measurements.

1. Experimental Setup

High pressure trickle bed reactor (HP TBR) is designed to operate at pressures up to 10 barg (~ 150 PSI). It consists of a reactor column, gas and liquid delivery system, gas-liquid separator, and the system for the measurement of the effluent liquid fluxes distribution (Figures B1, B2 and B3). With the aid of gamma-ray CT (Appendix C), the cross-sectional distribution of gas, solid and liquid phase holdups can be obtained at the designated axial positions.

1.1. TBR Column

The reactor column is a stainless steel flanged tube of a 1.5 m (5') height and 16.3 cm (6.4") inner diameter. At the top a pressure gauge with 0-200 psig range and a 1% full scale accuracy displays the pressure inside the column. Three pressure taps have been

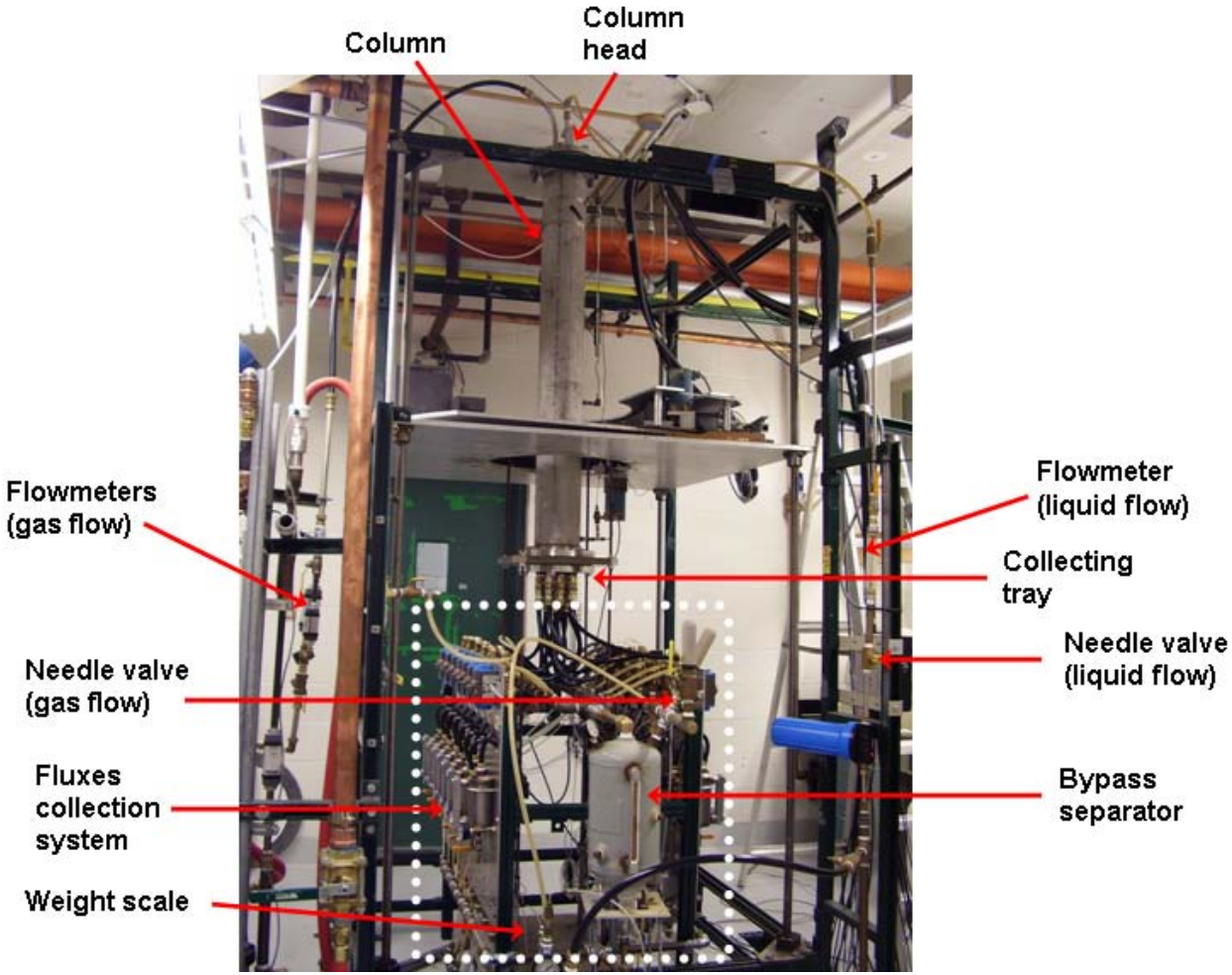

Figure B1: High pressure trickle bed reactor with the computed tomography unit

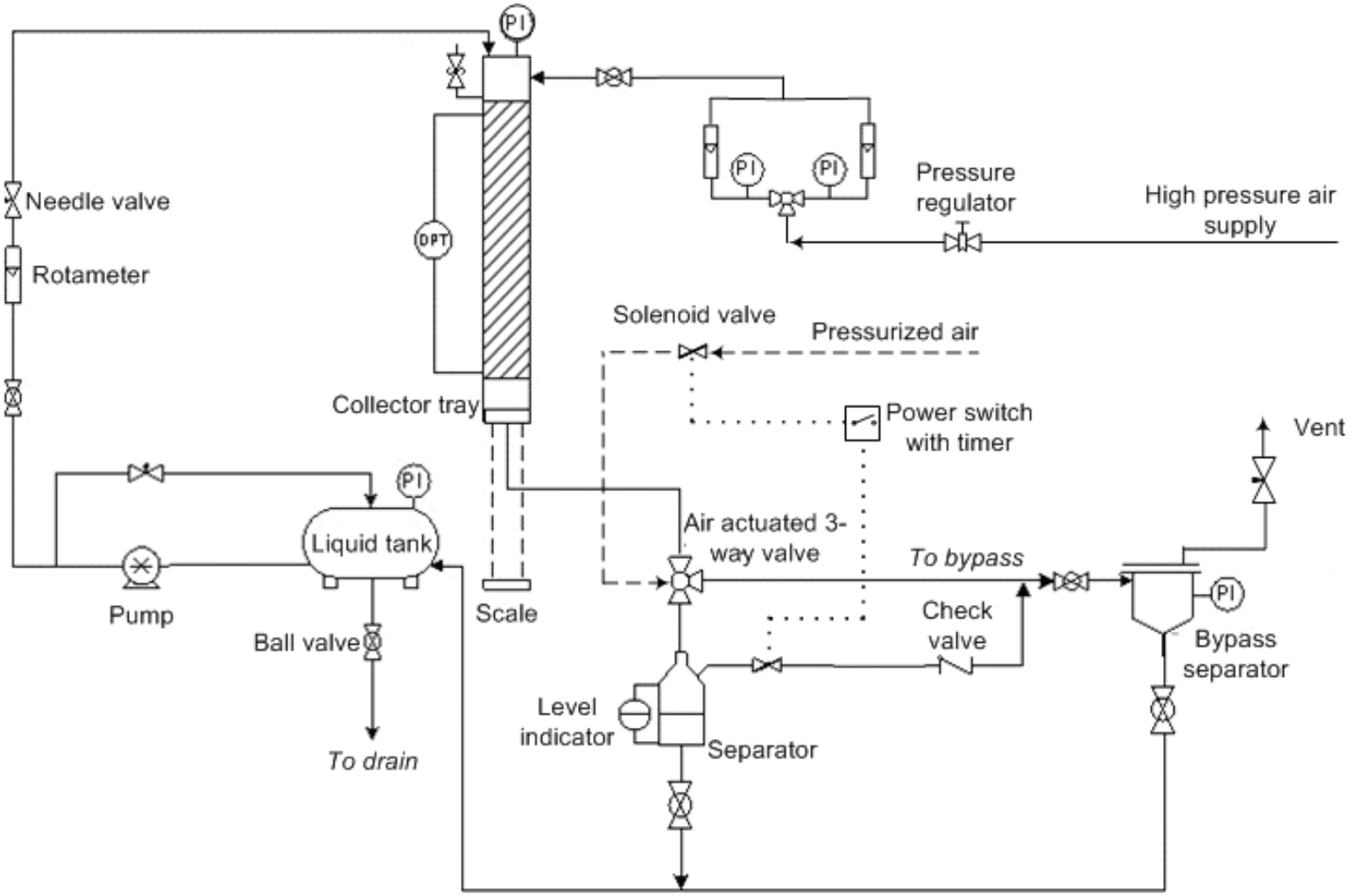

Figure B2: Schematic of the HP TBR.

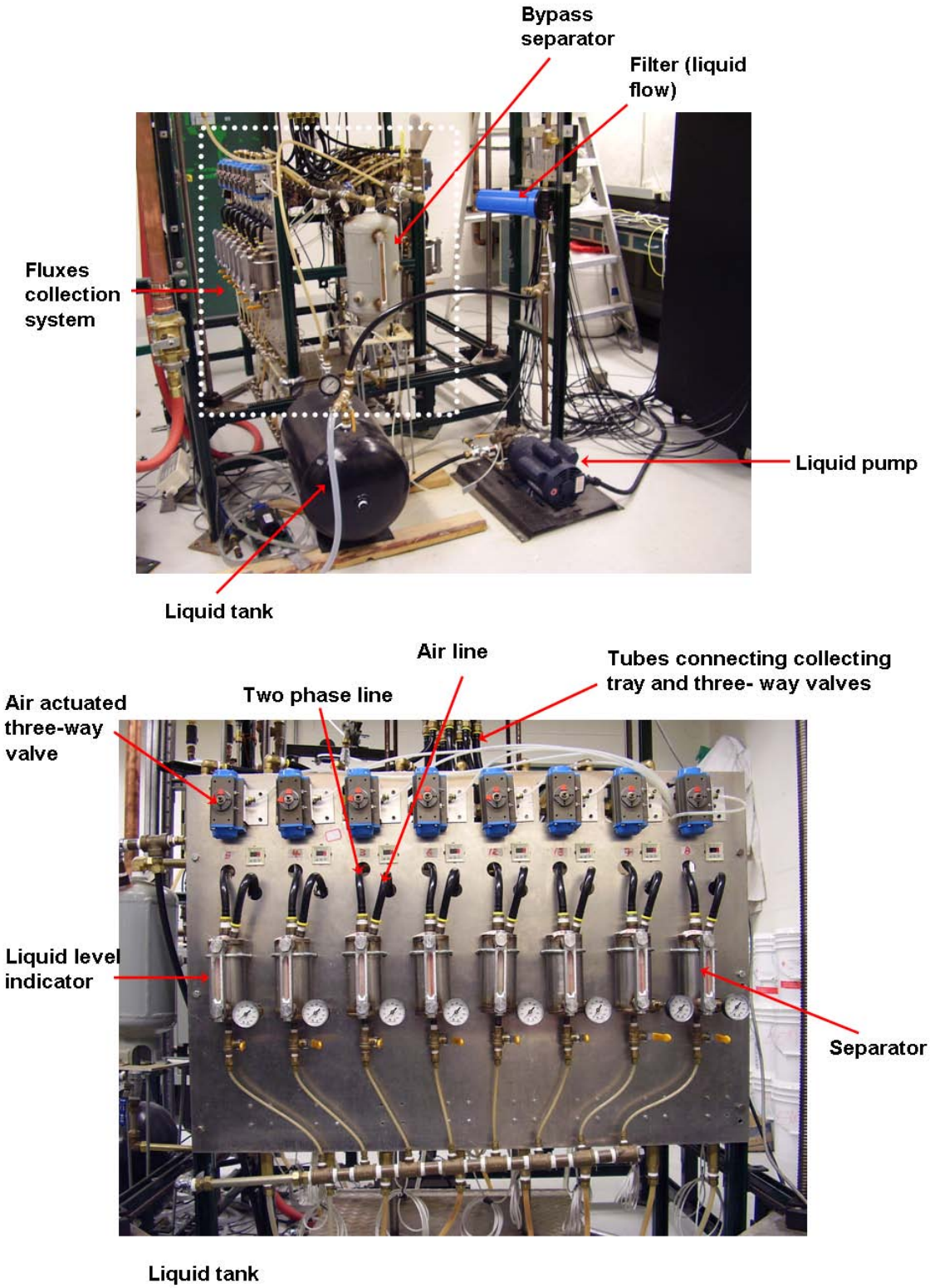

Figure B3: Details of the gas and liquid delivery system and liquid fluxes collection system.

drilled in the column (at the top, 50 cm below the top and at the bottom of the column) to enable pressure drop measurements.

1.2. Liquid delivery system

Liquid is stored in epoxy-lined horizontal tank of 15.2 gallons capacity (Figure B3). A cast bronze positive displacement pump (Grainger 6NY43) is used to supply the liquid to the column head. Liquid flow rate is controlled using the needle valve and measured using the flow meter (Omega FL-6305ABR, 0.5-5 GPM range) placed in the inlet line. After the gas-liquid separation in a bypass separator liquid is directed back to the storage tank.

1.3. Gas delivery system

The air injection system is connected to the high pressure air supply (180 psig). Air is directed to the top of the column through a ¾" tube. The air flow is controlled by a pressure regulator (Wilkerson R30-06-H00) and a series of ball valves in the inlet line and needle valve in the outlet line (Figures B1-B3). The air flow rate is measured using two (low and high range) Omega rotameters calibrated at 100 psig (7 barg).

1.4. Column head and liquid distributor

The column head is a stainless steel flange (Figure B4). A 5/8" liquid injection tube is passed through the central hole in a column head to allow injection of liquid into the liquid distributor. The liquid injection tube consists of several threaded pieces of 1 ft

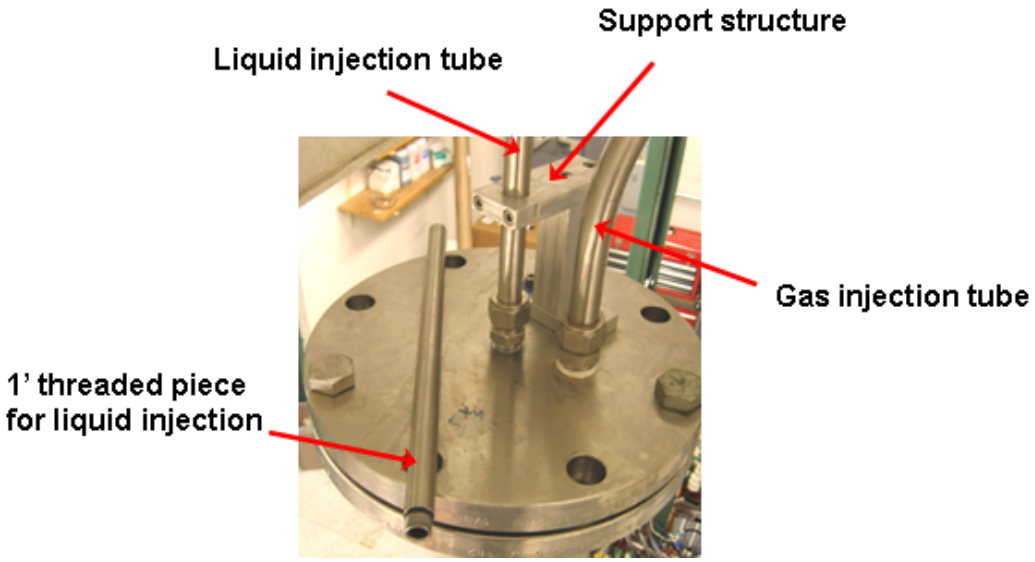

Figure B4: Column head

(30.5 cm) length. The pieces are added one by one and slide into the column through the sealed central hole. The last piece of the liquid injection tube is connected to the liquid distributor (Figure B5). Support structure maintains the liquid inlet tube aligned in the center. Additional tube is passed through the column head as the air inlet line.

The distributor (Figure B5) is a 2.5 cm (1") high box directly connected to the liquid injection tube. The liquid injected in the distributor exits through 240 holes of 0.9 mm diameter. The air injected at the top of the column flows through 19 tubes (6.5 mm I.D) passed axially though the distributor.

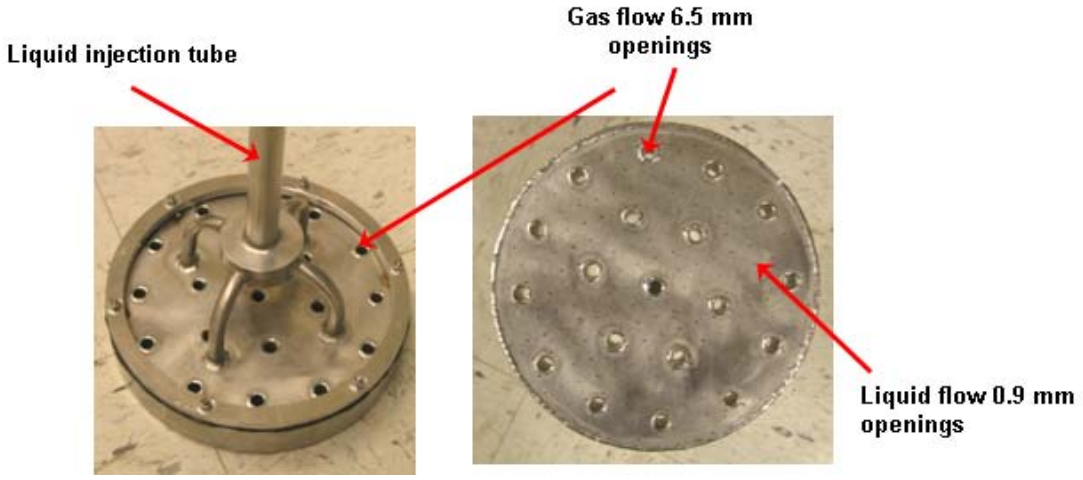

Figure B5: Liquid distributor

1.5. Collecting system for liquid fluxes distribution measurements

A collecting system attached to the bottom of the column enables the measurement of the spatially distributed liquid phase effluent fluxes (Figures B1-B3). A collecting tray (Figure B6) is positioned below the packing support mesh. The tray is a modified stainless steel flange which fits the bottom of the column. It is used to split gas-liquid stream into 15 streams and direct each of them to its own gas-liquid separator. Collecting tray has one central sector, a first ring with 5 sectors and a second ring with 9 sectors. The sectors are separated by welded walls of 3" (76 mm) height and about 1 mm thickness. The outlet of each sector is a ½" threaded pipe. Packing support (1 mm mesh) is positioned on the collector in order to support the bed and prevent particles from clogging the outlets of the sectors. Gas-liquid separators are installed on two panels (Figure B3). The principle of liquid collection system is given in Figure B7. During the

flux measurements, two phase flow is directed to 15 separators instead into the single bypass separator. To achieve this, an air actuated three-way valve is placed above each of

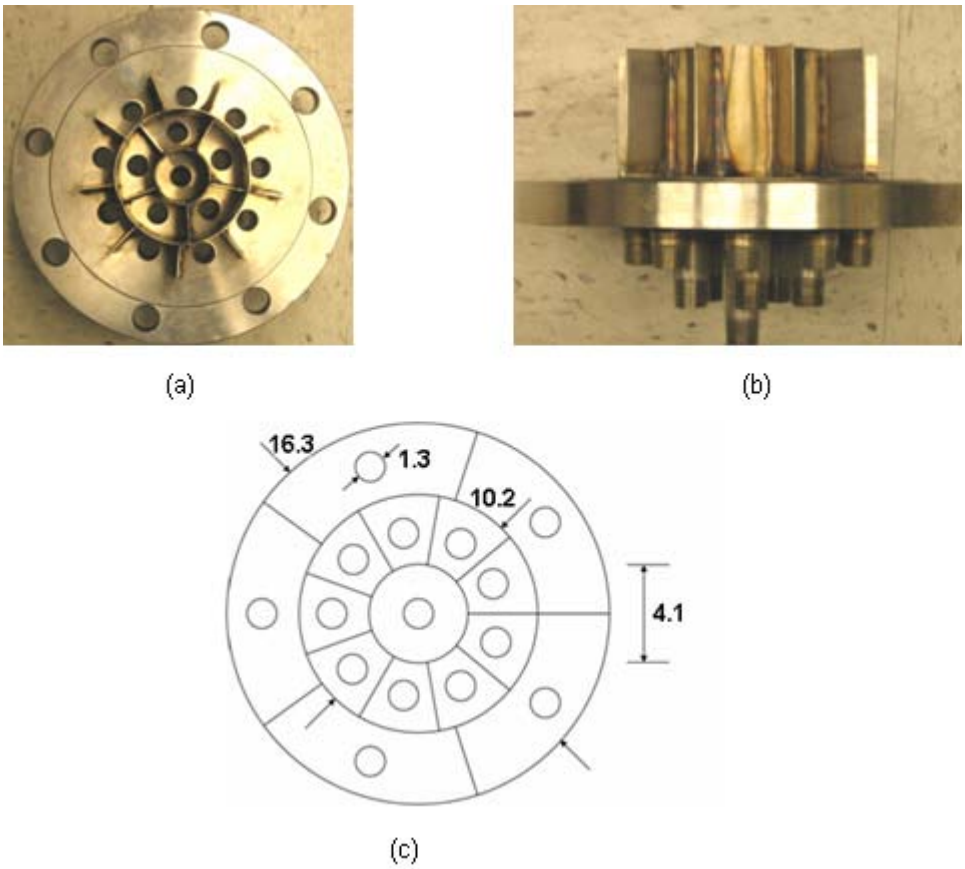

Figure B6: Collecting tray (a) top view, (b) side view, (c) schematics of the 15 compartments. All dimensions in centimeters.

the 15 liquid separators. The actuation of the three-way valve is controlled with the normally closed solenoid valve connected to the pressurized air. The solenoid valve, using power switch with timer, is energized only for a prescribed period of time determining collection time. During this time, solenoid valve is open and the pressurized air actuates the air actuated three-way valve. Once actuated, the three-way valve directs the flow into the liquid collectors instead into the main, bypass separator. Once the

collection time lapsed, the liquid volume collected in each separator is read of the liquid level indicator. Liquid flow rate at each compartment is calculated as the average value during the collection time.

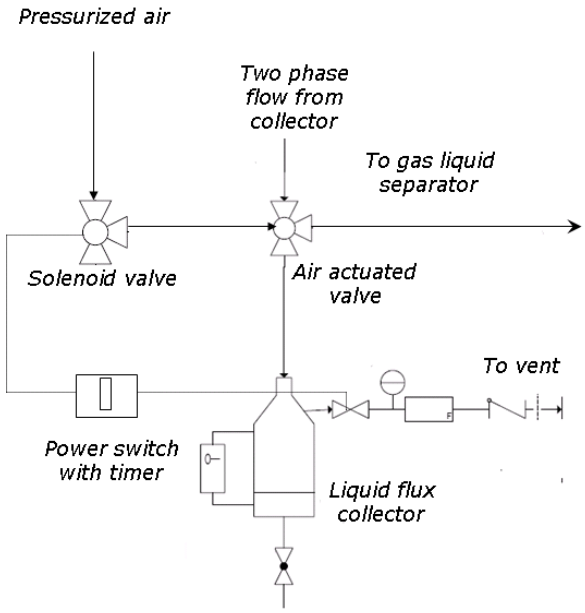

Figure B7: Schematics of the fluxes collection system

1.6. Bypass

Except for a period of fluxes collection, the two phase flow is at all times directed to a 1" pipe connected to a bypass separator (Figures B1-B3, and B7). The bypass separator is an 8" (20.3 cm) vertical tank. After separation, liquid phase is directed to the liquid tank and air is vented to atmosphere after it goes through the air flow control system (Section 1.3).

2. Measurements

2.1. Pressure drop

Two Validyne differential pressure transducers (low range 1.25 psid and high range 5 psid) are used for the pressure drop measurements. The pressure drop is read as a percentage of the full scale.

2.2. Liquid holdup

The column stands on a platform scale (Arlynscales 320D, Figure B1). The scale accepts a maximum load of 220 kg and has a resolution of 50g. The mass of the column can be monitored at all times. The scale is used to measure liquid holdups as per procedure ("weight method") described below.

2.3. Liquid fluxes

When collecting, the liquid levels in each gas-liquid separator rise and can be measured using liquid level indicators (Figure B3). The gas exits each separator and is directed to the solenoid valves which are opened as long as the 3 way ball valves are actuated. The air mass flow rates are measured by a hot-wire gas meter (SMC PF2A 551-N04-1). Once the collection is finished, the gas-liquid separators can be flushed into the liquid tank by opening a ball valve installed under the separators.

3. Operating Procedure

3.1. Packing the column

1.Close the ball valve upstream of the bypass separator

2. Start the liquid pump and set low liquid flow rate

3. Remove the column head

4. Power the weight scale

5. Install the collection tray with its gasket at the bottom of the column

6. Put the support mesh on the collector tray sliding it from the top of the column

7. Measure the height of the empty column (from the grid to the flanged end at the top) and record the reading of scale display

8. Pack the column with the packing particles. One possible procedure is as follows. Place the PVC tubing inside the column leaning the lower part on the support mesh. Fill the PVC tubing with packing particles and then introduce them into the column by lifting the tubing. Repeat until the desired packing height is achieved. If needed, settle (produce more dense arrangement)

9. Calculate the height of the bed: measure the distance between the bed top and the flanged end at the column top

10. Record the reading on the scale display and calculate the mass of particle composing the bed

11. Calculate the bed external voidage (weight method)

12. Install the distributor and the sealing switch lock on the column head. Position the head flange with its gasket on the column by introducing the distributor first. Slide the distributor inside the column to the desired height above the bed

13. Fix the head with 8 bolts

14. Connect the liquid and gas inlets to the liquid and gas inlet tubes; connect the quick-disconnect fittings to the collector tray.

3.2. Prewetting the bed

1. Close the ball valve upstream of the bypass separator
2. Start the liquid pump and set low liquid flow rate
3. Follow the liquid level (using the liquid level indicator next to the column) and stop liquid flow once liquid level inside the column is above the top of the packed bed. Leave overnight (fill the packing particles internal pores)
4. Open the ball valve upstream the bypass separator and allow the liquid to drain.

3.3. Two phase flow and measurements

1. Power the system (weight scale, pressure transducer, fluxes collector system)
2. Pressurize the system using pressure regulator. Record weight scale reading.
3. Switch on the timer controlling the 3-way ball valves and the solenoids so that the fluxes collection system is pressurized
4. Open the liquid inlet ball valve enabling the liquid flow to the column; use the needle valve and liquid flow meter to set the desired flow rate
5. Initiate gas flow and use needle valve and appropriate gas rotameter (i.e., high or low range) to set the desired gas flow rate. Make sure that column pressure is at the desired value (once flow is initiated it will decrease due to pressure drop) and use pressure regulator to adjust it as needed.
6. Wait until steady state (follow weight scale and pressure drop readings)
7. Record weight scale reading (use for liquid holdup calculation) and pressure transducer reading
8. If cross-sectional measurements of holdup are needed (computed tomography imaging) follow instructions given in Appendix C.

Appendix C
Use of Computed Tomography for Phase Distribution Studies in a HP TBR

1. Overview

This section gives the comprehensive manual for obtaining cross-sectional phase distribution in a high pressure trickle bed reactor (HPTBR). We first give brief description of CT hardware. Then, a step by step guide to process of scanning and use of expectation-maximization (EM) algorithm for reconstruction is given. All scan and reconstruction parameters are given for the use with HPTBR; however, we also give detailed instruction on how to customize the Fortran codes to any given system.

More details on HPTBR and its operating procedure are available in Appendix B. Details of the CT hardware and data acquisition system and additional aspects of CT operating procedure are given in Roy, 2006. Theoretical aspects of the gamma-ray scanner performance assessment are available in Appendix A.

2. Description of scanning procedure

TBR is positioned between gamma-ray source and array of gamma-ray detectors (Figure C.1). During experiment (scan), source and detectors are brought in a number of positions

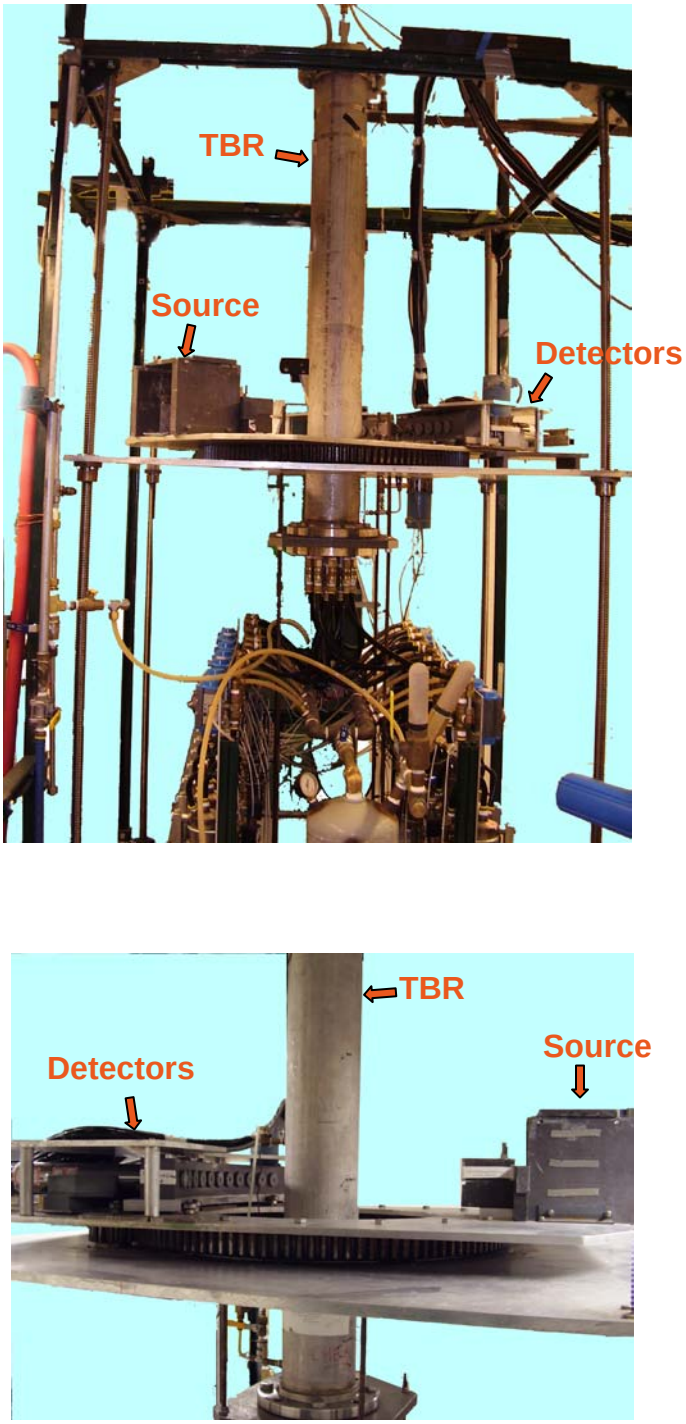

Figure C.1: High pressure trickle bed reactor and computed tomography unit

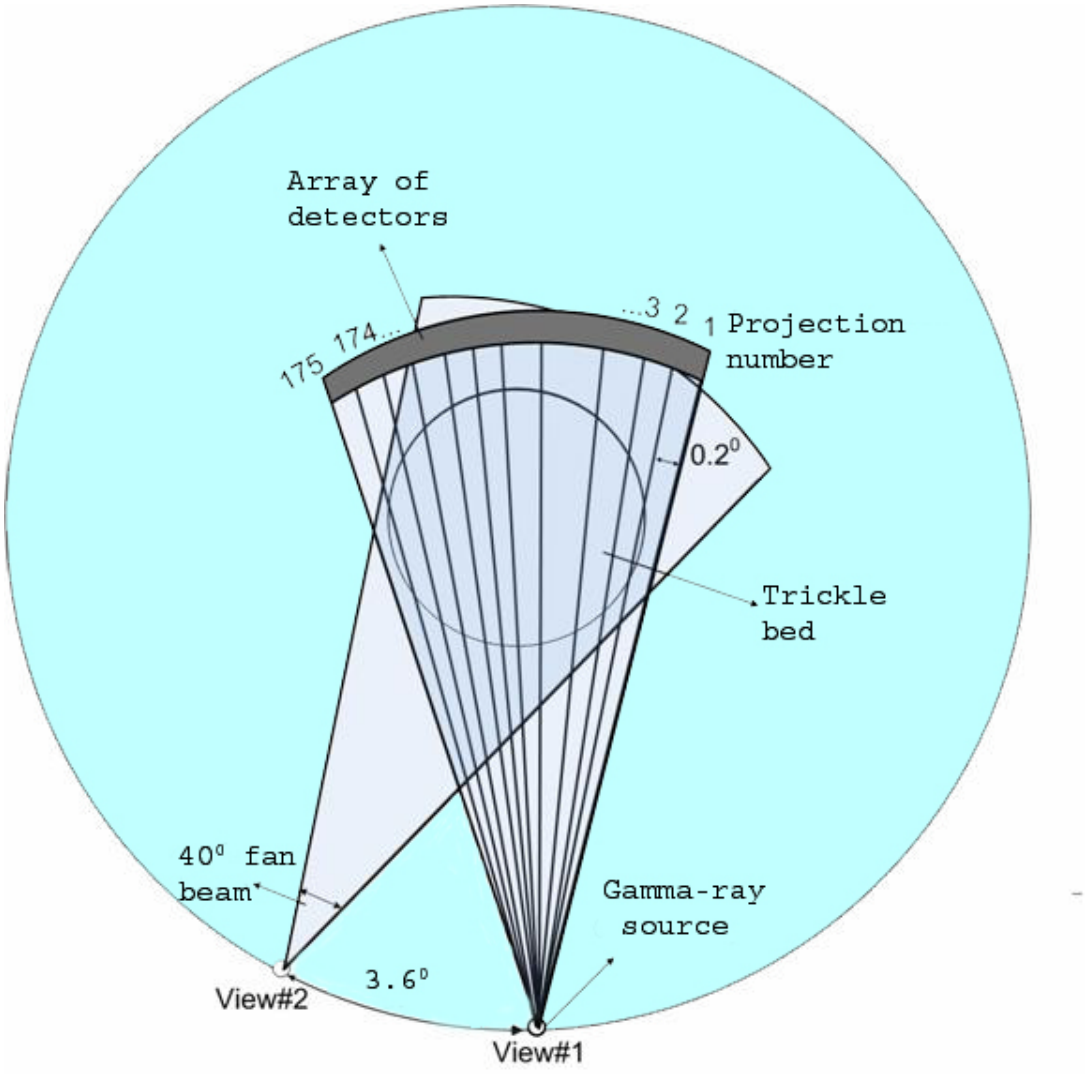

Figure C.2: Source-detectors arrangement in the gamma-ray computed tomography unit (Not drawn to scale).

relative to each other and the column. At each of these positions attenuation of the incident radiation is recorded at the gamma-ray detectors. CT setup enables two types

of source/detectors motions (see Figure C.2): (i) gamma-ray detectors and source can be (simultaneously) rotated around the axis of the column being scanned (via the view motor); (ii) the collimator and detector assembly can be moved (via the projection motor) relative to the source along the arc defined by the detector-array. In order to ease the description of the data collection process we define two terms: view and projection (Roy et al., 2004; Roy, 2006). *View* designates fixed source position. *Projections* are different positions of assembly of detectors towards source; in any given view, detectors take 25 different positions in increment of 0.2^0. The total number of projections considered in one view is then

$$(\#\,\text{Projections/view}) = (\#\,\text{Detectors}) \cdot 25 .$$

For a case of 9 detectors, which represents the maximum number of detectors that can be used in the portable CT unit, this gives 9*25 = 225 projections per view. Source makes full circle around the scanned object in increment of 3.6^0, i.e. there are 100 views in one scan (see Figure C.2). Thus, the total number of projections, i.e., particular pathways of gamma rays that are being considered in one scan are

$$(\#\,\text{Projections/scan}) = (\#\,\text{Projections/view}) \cdot 100 .$$

For the case of 9 detectors the total number of projections collected during one scan is 225*100 = 22500.

3. Data acquisition

For each of the projections, scan data is acquired and saved in a file. The data acquisition process is performed by running the code *C:\Carpt_CT\CT\acquire\Debug\CT.exe*. To start the code either:

i. Double-click the icon *Shortcut to CT.exe* located on the desktop, or

ii. Click START=>Run… and then type: *C:\Carpt_CT\CT\acquire\Debug\CT.exe* and press OK, or else

iii. Open the folder *C:\Carpt_CT\CT\acquire\Debug* and double-click the *CT.exe* icon.

3.1. User inputs and the format of CT Data

After starting CT.exe code, user is asked to choose the values for the following parameters:

1. Sampling mode
2. Sampling rate
3. Output file format
4. Threshold level
5. Number of data sets

The options chosen below are considered as *default values.* In Figure C.3, the command window of the *CT.exe* code is shown for the case of using the default values. Refer to Section 3.2 if non-default values are to be used.

3.1.1. Sampling mode

This option determines the number of threshold levels and sampling rates used. See Sections 3.1.4 and 3.1.2 to learn more about these quantities. User can choose between:

a. One threshold level, one sampling rate

b. Two threshold levels, one sampling rate

c. One threshold level, two sampling rates

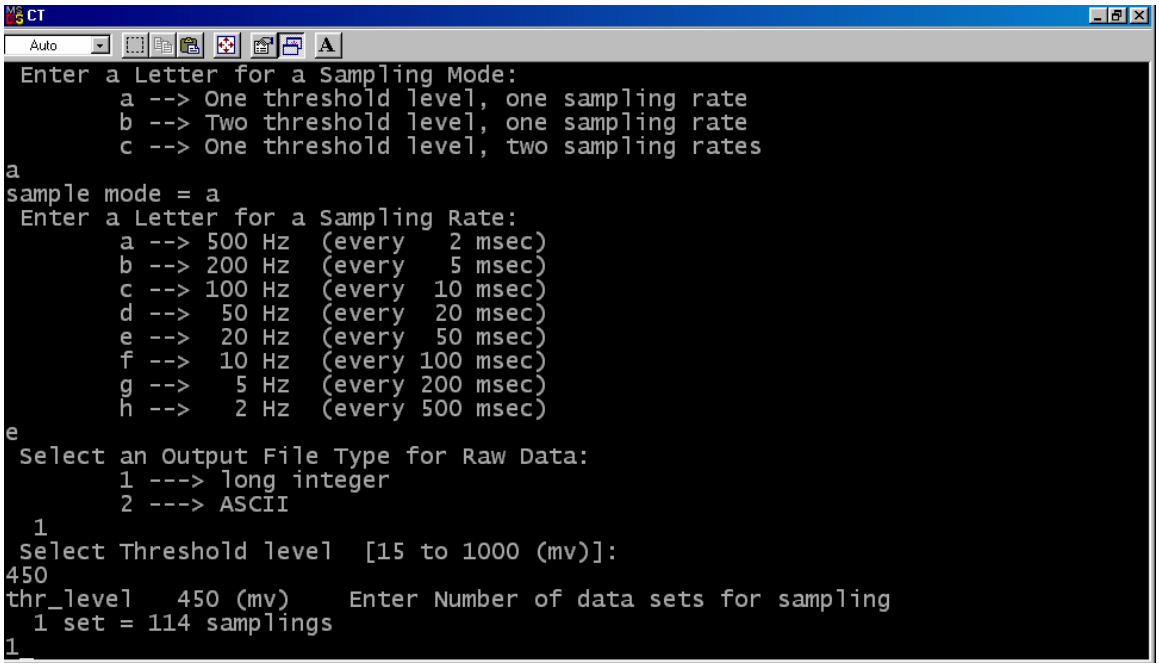

Figure C.3. Command window of *CT.exe* code

Typically, one threshold level and one sampling rate are employed (see Section 3.2 about using the non-default values). To do this, type *a* in a command window and press ENTER (Figure C.3).

3.1.2. Sampling rate

This quantity determines how fast the data sampling is performed. The program offers sampling frequencies in a range of 2-500 Hz (see Figure C.3). In general, the recommended values are 10-50 Hz. Depending on the size of the column and the materials used, for higher attenuation systems, lower sampling rate may be used. For the HPTBR value of 20 Hz is recommended. User sets the sampling rate by typing the latter

in front of the desired value and pressing ENTER. In that way, for a 20 Hz sampling rate, type *e* in a command window and press ENTER.

3.1.3. Output file format

These are the options:

1. long integer
2. ASCII

This option determines the number format of counts data in the output file. Most commonly, the first option is used by typing *1* in a command window and pressing ENTER.

3.1.4. Select threshold level

The process of synchronization of the detector peaks gives the threshold level. The counts with the photon energy below the threshold level are discarded (scatter). Input the value of threshold level and press ENTER.

3.1.5. Number of data sets for sampling

For each projection, not only a single value of photon counts, but a sample of values is taken. This is done to improve the accuracy of measurements since the emission of photons by gamma-ray source is a stochastic process. In the reconstruction, the sample average is used as the number of counts at each of the projections (See sections 3.1.6 and 4.3.1). Total number of data points for one projection is given as

(Number of data sets for sampling)*(Number of data points per data set).

Number of data points per data set has a fixed value of 114. However, user has the option to increase the total number of data points by choosing the *number of data sets for sampling.* For the high pressure TBR, use one data set by typing *1* and pressing ENTER. In this case:

(Total number of data points for one projection)=1*114=114.

See also Section 3.2.

3.1.6 *CT.exe* output file

After the parameters of *CT.exe* are set, the scan starts and runs automatically. The data are stored in a file *C:\Carpt_CT\CT\acquire\Debug\calcount.asc.* The first line of the output file states the number of data points (114 default value) for each projection (Section 3.1.5) and the sampling rate (Section 3.1.2). Then view and projection numbers are declared followed by data samples. Then, next projection is declared and the data for that projection are given. After 25 projections for the first view, the data for the next view follow and so on.

3.2. Using the non-default parameters in CT data acquisition

3.2.1 Number of detectors used

Number of detectors used depends on the diameter of the column that is being scanned. By default, 9 detectors are employed, but for some applications fewer detectors can be employed. The rule is that all detectors registering only counts of projections not crossing the TBR column need not be used. Since the column is centered, this means one can

choose among the following options: 9, 7, 5 or 3 detectors. For the high pressure TBR system use 9 detectors.

3.2.2 Number of projections

There is no explicit option in *CT.exe* that would allow the change of number of projections per view. Changing the number of projections represents advanced use of CT unnecessary for all the typical applications. However, the effect of changing of the number of projections per view on the scanner performance have been discussed in Appendix A.

3.2.3 Sampling mode

As stated in Section 3.1.1, the default sampling mode is to collect data for one threshold level at one sampling rate. In case of use of two threshold levels, the data (number of counts) will be collected for both of the levels. Similarly, if two sampling rates are used, the data will be collected for each of them. This means that if either option b) or c) from Section 3.1.1 are used there will be one additional output file with a default name *C:\Carpt_CT\CT\acquire\Debug\calcoun2.asc.* The format of this file will be analogous to the format of *C:\Carpt_CT\CT\acquire\Debug\calcount.asc* output file. Note that for high pressure TBR system considered here default sampling mode should be used.

3.2.4. Sampling rate

This parameter does not affect the way that data are stored or the way data are processed. User can change this value, but keep in mind the recommendations. Also, note that if option c) in Section 3.1.1 is used, i.e., if collecting mode is one threshold level and

two sampling rates, the user is asked to input two instead of one sampling rates in *C:\Carpt_CT\CT\acquire\Debug\CT.exe* command window.

3.2.5 Output file format

Use the default value.

3.2.6. Threshold level

This is not a value that can be changed arbitrarily. Use only the value that synchronizes the detector peaks.

3.2.7 Number of data sets

Any integer value can be used. Increasing number of data sets increases the scan time. For our case, one data set is sufficient. If more than one data set is needed, simply type the desired number and press ENTER.

4. Image reconstruction

4.1. EM algorithm

The EM algorithm is a general procedure for maximum likelihood (ML) estimation and is most commonly employed in the *incomplete data* problems (McLachlan and Krishnan, 2008). The formulation of the algorithm is due to Dempster et al., 1977 while its specific application for transmission tomography was given by Lange and Carson, 1984. In this section, we briefly summarize the main points of the EM algorithm, and of the Lange and Carson, 1984 derivation.

Suppose that $p(\mathbf{Y},\boldsymbol{\mu})$ is a known likelihood (density) function of the measured data ($\mathbf{Y}$) parameterized by the vector $\boldsymbol{\mu}$. The objective is to estimate the elements of $\boldsymbol{\mu}$. The standard ML method would involve the maximization of $\ln p(\mathbf{Y},\boldsymbol{\mu})$ with respect to the vector of parameters $\boldsymbol{\mu}$. However, in general, this maximization need not be a trivial issue. EM algorithm circumvents this problem by postulating *complete data set* ($\mathbf{X}$) and its conditional log-likelihood function given the measured (*incomplete*) data ($\ln f(\mathbf{X},\boldsymbol{\mu})\,|\,\mathbf{Y}$) to make the maximization problem more tractable. The ML estimate of the vector of parameters is then achieved by an iterative procedure consisting of two steps: expectation (E) and maximization (M).

In the E-step (equation (1)) the expectation of the complete data set given the measured data and the current estimate of the parameter vector $\boldsymbol{\mu}$ is calculated. In the M-step, the

$$E\{\mathbf{X}\,|\,\mathbf{Y},\boldsymbol{\mu}^{(n)}\} \tag{1}$$

complete data log-likelihood is maximized with respect to $\boldsymbol{\mu}$ thus providing new ($\boldsymbol{\mu}^{(n+1)}$) estimate of the vector of parameters. The outcome of the iteration procedure is the vector $\boldsymbol{\mu}$ corresponding to the maximum value of the complete data log-likelihood. At the same time, such vector maximizes the incomplete data log-likelihood (Dempster et al., 1977) and thus, indirectly, achieves the objective of the standard ML procedure.

In the Lange and Carson, 1984 implementation for transmission tomography, the incomplete data set (i.e., the number of photons registered by the detectors) likelihood function follows the Poisson distribution, equation (2):

$$p(Y_i, \boldsymbol{\mu}) = \prod_i \frac{[E(Y_i)]^{Y_i}}{Y_i!} \exp(-E(Y_i)). \tag{2}$$

with the expected value given by the Beer-Lambert's law (equation (3)).

$$E(Y_i) = \lambda_i \exp\left(-\sum_{j \in P_i} l_{ij} \mu_j \right) \tag{3}$$

In equations above, i and j are the projection and pixel index, respectively, Y_i is the random vector of the number of photons registered at the detectors, λ_i is the mean number of photons emitted by the source, E(.) designates the expectation operation, and P_i is a set of the pixels contributing to projection i. The ML estimation problem, i.e., the calculation of the vector of attenuation coefficients ($\boldsymbol{\mu}$), is then performed by introducing the number of photons leaving each pixel (X_{ij}) as the complete data set.

4.1.1. E step of the EM algorithm

In the E-step, the expectation of the *complete data set* conditional on the *measured (incomplete) data set* is estimated using the current values of the *set of parameters* (see also Figure C.5-a).

$$E(X_{i,j} \mid Y_i) = Y_i + E(X_{i,j}) - E(Y_i) \tag{3a}$$

$$E(X_{i,j}) = \gamma_{i,j} = d_i \exp\left(-\sum_{k=1}^{j-1} l_{ik} \mu_k \right) \tag{3b}$$

$$E(Y_i) = \gamma_{i,j} \exp\left(-\sum_{k=j}^{m-1} l_{ik} \mu_k \right) \tag{3c}$$

Note that Y_i are the actual experimental values of photon counts for each projection. d_i (number of photons emitted from the gamma-ray source) are not directly measured during experiment, but there is a procedure to circumvent this problem (see Section 4.1.3). Using equation (3a) the number of photons entering and leaving pixel *j-1*, $M_{i,j-1}$ and $N_{i,j-1}$, respectively, can be calculated as (Figure C.4):

$$\begin{aligned} N_{i,j-1} &= E(X_{i,j-1} \mid Y_i) \\ M_{i,j-1} &= E(X_{i,j} \mid Y_i) \end{aligned} . \tag{3d}$$

Knowing these values, we move onto M step of the EM algorithm.

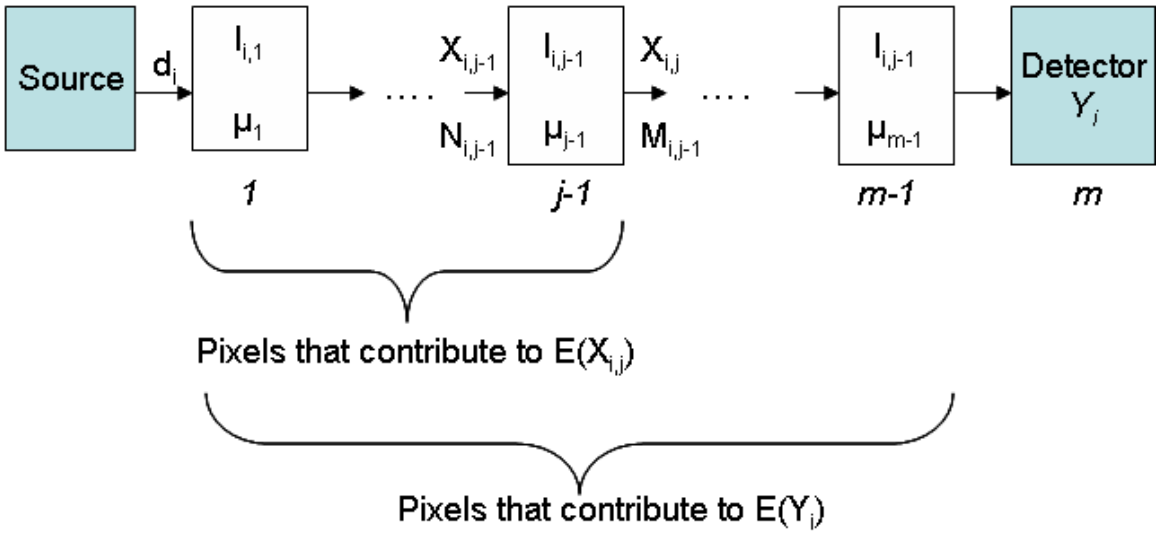

Figure C.4. EM algorithm – symbols used

4.1.2. M step of the EM algorithm

The number of photons leaving each pixel (i.e., the compete data set) is dependent only on the number of pixels that enter and the probability of the photon transmission given by the Beer-Lambert's law. Hence, the complete data set likelihood follows a binomial distribution and is given by equation (4)

$$\ln \mathrm{f}(\mathbf{X},\boldsymbol{\mu}) = \sum_{i}\sum_{j\in I_i}\left\{-X_{i,j+1}l_{ij}\mu_j + \left(X_{i,j}-X_{i,j+1}\right)\ln\left(1-\exp\left[-l_{ij}\mu_j\right]\right)\right\} + R_j, \tag{4}$$

where R_j represents all the terms not dependent on μ_j. The maximization yields the following expressions for the update function

$$A\mu_j^{\,2} + B\mu_j + C = 0 \tag{4a}$$

$$A = \sum_{i\in J_j}(M_{i,j}-N_{i,j})\frac{l_{i,j}^{\,2}}{12} \tag{4b}$$

$$B = -\sum_{i\in J_j}(M_{i,j}-N_{i,k})\frac{l_{i,j}}{2} \tag{4c}$$

$$C = \sum_{i\in J_j}(M_{i,j}-N_{i,j}) \tag{4d}$$

Solving this system of equations yields the values of set of parameters that *maximize the log-likelihood of the complete data set* closing the iteration loop. In equations (4) $i \in J_j$ designates all the projections to which pixel *j* contributes. The updated value of the set of

parameters is obtained by solving the quadratic equation (4a) and then used in the E-step. In that way the iterative loop is closed. The convergence criteria can be defined in two ways: either the change of the complete data set log-likelihood between two successive iterations is within the given tolerance, or the change of attenuation coefficients between two successive iterations is within the given tolerance. We use the latter criterion.

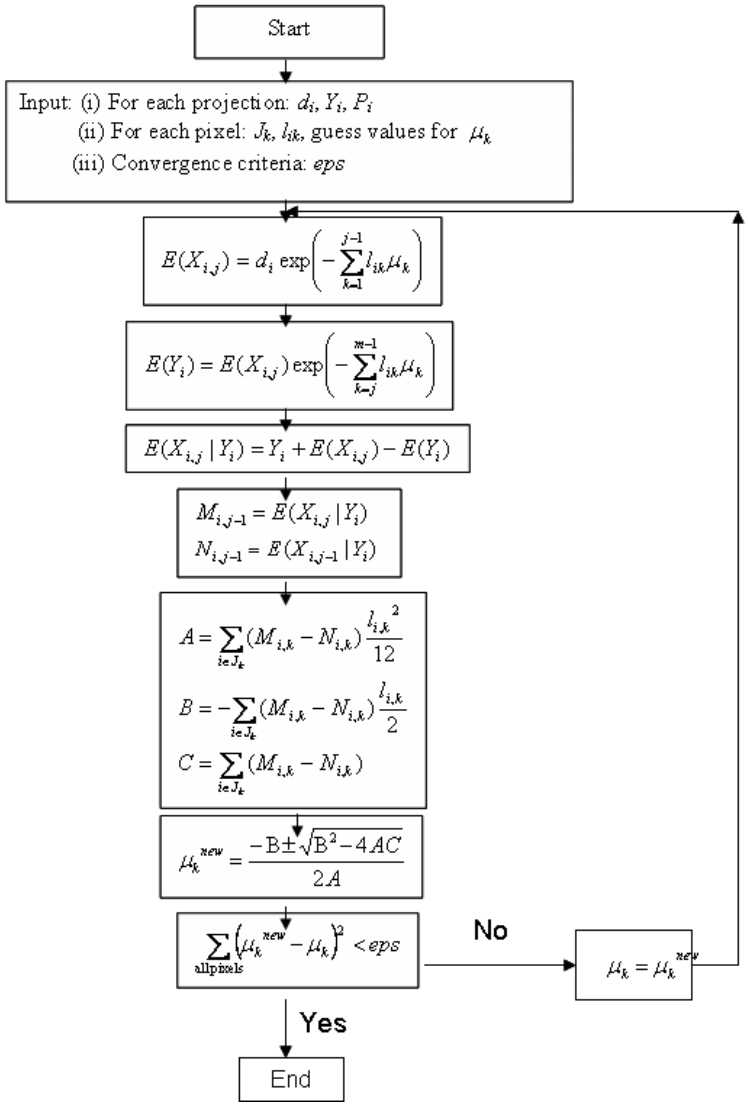

Figure C.5.-a. Flowchart of EM algorithm

Figure C.5-a is the flowchart of the EM algorithm. To understand the full procedure reader should also refer to Sections 4.1.3, 4.2 and 4.3. Input values are:

d_i - number of photons emitted from the gamma-ray source (see Section 4.1.3)

Y_i – measured photons counts with the actual system of interest between source and detectors for each of the projections.

P_i – the entire set of pixels that projection i transverses on its way from source to detector obtained by considering reconstruction domain size, pixel size, projection trajectory etc. See Section 4.3.3.

J_k – the entire set of projections to which pixel k contributes obtained by considering reconstruction domain size, pixel size, projection trajectory etc. See Section 4.3.3.

$l_{i,k}$ – length of the path of beam i through the pixel j. See Section 4.3.3.

μ_k – guess value for attenuation coefficient for each pixel in the domain (see Section 4.3.4)

eps – convergence criteria, i.e., the tolerance for the difference in values of attenuation coefficients between two successive iterations

The calculation starts with the E step. First the expectation of photons leaving each pixel ($E(X_{i,j})$) and expectation of photon counts in the detector ($E(Y_i)$) are calculated using equations (3b) and (3c), respectively. Then the expectation of complete set of data ($X_{i,j}$) conditional on the measured, incomplete set of data (Y_i) is calculated according to equation (3a). Next, the corresponding number of photons entering and leaving each pixel

is assigned for each of the projections. This completes the E step. In the M step, according to equations (4), the values of attenuation coefficient are updated. Then, if the tolerance threshold is reached the program is terminated, otherwise the next iteration proceeds.

4.1.3. Transmission ratio

In Sections 4.1.1 and 4.1.2 the principles and flowchart of the EM algorithm are given. However, so far, we did not address the problem of the number of photons emitted by the source (i.e., d_i in equations 3). In principle, this value could be calculated if the exact value of source activity was known. The source activity declines with time and to avoid introducing uncertainty in this way, a different procedure was devised. For each of the projections, photon counts are registered with *only air* in the path between source and the detectors. We denote these values as I_{i0}. Next, we place the object between source and the detectors and register the counts. These values, as earlier, are denoted as I_i and will be lower than I_{i0} values due to the attenuation exerted by the object. Hence, we can rewrite equations 3a through 3c as:

$$E(X_{i,j} \mid I_i) = I_i + E(X_{i,j}) - E(I_i) \tag{5a}$$

$$E(X_{i,j}) = I_{i0} \exp\left(-\sum_{k=1}^{j-1} l_{ik} \mu_k \right) \tag{5b}$$

$$E(I_i) = I_{i0} \exp\left(-\sum_{k=1}^{j-1} l_{ik} \mu_k \right) \cdot \exp\left(-\sum_{k=j}^{m-1} l_{ik} \mu_k \right) \tag{5c}$$

Dividing equations 5 with I_{i0} yields:

$$\frac{E(X_{i,j} \mid I_i)}{I_{i0}} = TR + \frac{E(X_{i,j})}{I_{i0}} - \frac{E(I_i)}{I_{i0}} \tag{6a}$$

$$\frac{E(X_{i,j})}{I_{i0}} = TR \cdot \exp\left(-\sum_{k=1}^{j-1} l_{ik} \mu_k \right) \tag{6b}$$

$$\frac{E(I_i)}{I_{i0}} = TR \cdot \exp\left(-\sum_{k=1}^{j-1} l_{ik} \mu_k \right) \cdot \exp\left(-\sum_{k=j}^{m-1} l_{ik} \mu_k \right) \tag{6c}$$

$TR = \frac{I_i}{I_{i0}}$ is the transmission ratio that can be calculated for each of the projections. Note the slight difference between LHS of equations (3a) and (6a). Due to this difference, equation (3d) becomes:

$$\begin{aligned} N_{i,j-1} &= \frac{E(X_{i,j-1} \mid Y_i)}{I_{i0}} \\ M_{i,j-1} &= \frac{E(X_{i,j} \mid Y_i)}{I_{i0}} \end{aligned} \tag{7}$$

So, the final expressions of the E step are the same as earlier; they are only normalized with the values of I_{i0}.

In the M step, we solve equation (4a) to estimate new values of set of parameters. Note that after introducing equation (7) instead of (3d), terms A, B and C will have additional

factor $\frac{1}{I_{i0}}$ which will cancel out in equation (4a). Hence, normalization will not affect the M step.

In Figure C.5-b, the revised EM algorithm is given and the changes we introduced are shown. This version of the algorithm is the one that is actually used for reconstruction and is discussed in details in Section 4.3.5.

4.2. Outline of the procedure to obtain cross sectional values of holdups

We focus on characterization of holdups in high pressure trickle bed reactor. The goal is to obtain gas, liquid and solid holdups across the 2D domain for a fixed axial position. To achieve this goal, the following steps have to be taken:

4.2.1. Scans

Perform scans for all of the following conditions:

4.2.1.1. Only air in the path between source and the detectors (i.e., perform the scan without placing the column in CT)
4.2.1.2. Column containing liquid only (static system, no flow)
4.2.1.3. Column containing gas and solids (static system, no flow)
4.2.1.4. Column containing liquid and solids (static system, no flow)
4.2.1.5. Actual two phase flow at desired operating conditions.

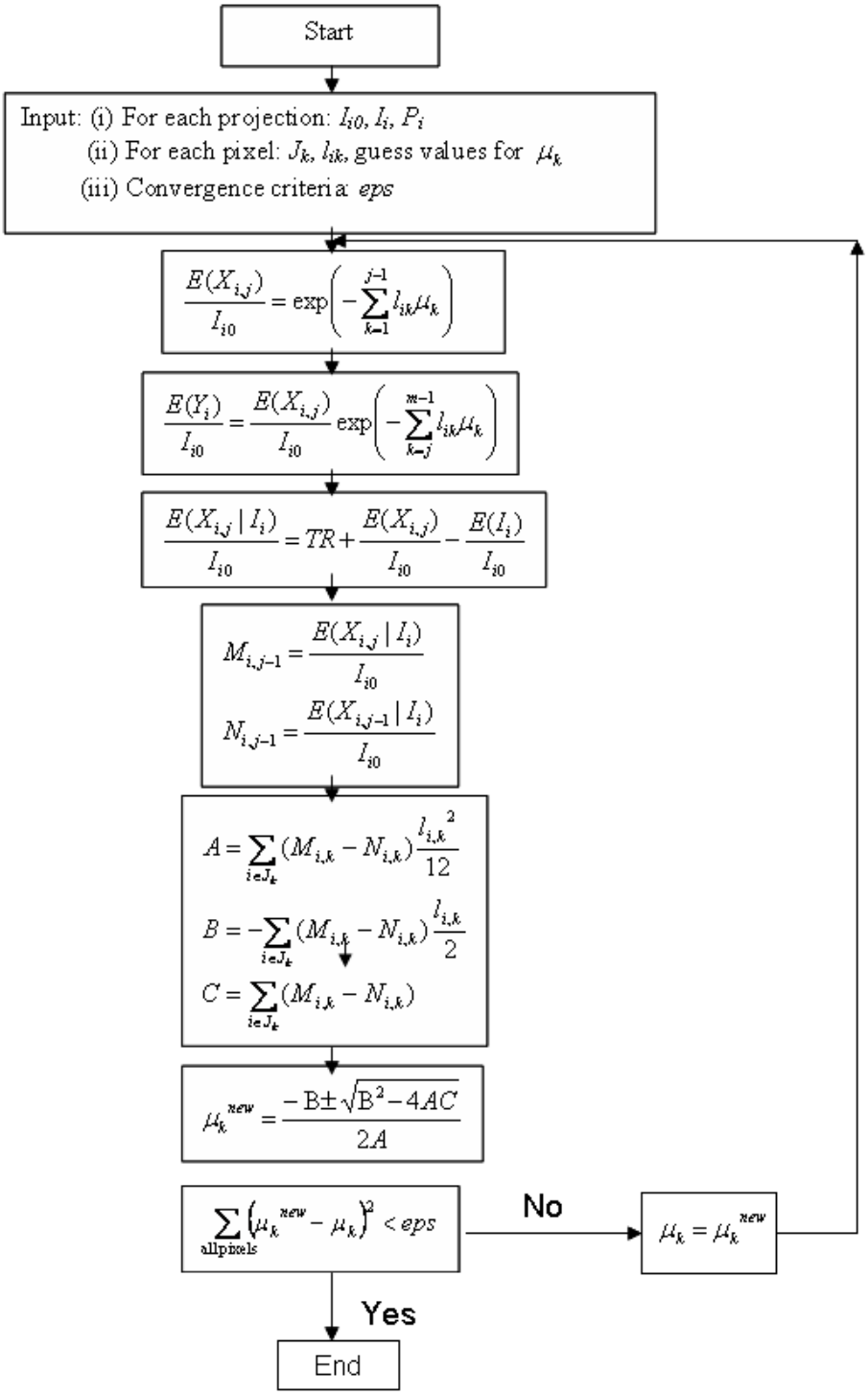

Figure C.5-b. Flowchart of the revised EM algorithm

Only performing *all* of the above scans yields sufficient data for holdups calculation. Note that information about the number of photons emitted by the source (see equation 3b) is not strictly known and is not measured. Instead, scan described in Section 4.2.1.1 is used to provide values of incident photon counts (see Section 4.1.3).

4.2.2. Reconstruction

Perform reconstruction for the conditions 4.2.1.2 through 4.2.1.5 above. The procedure of reconstruction is given in Section 4.3 and it will yield attenuation coefficients distribution for each of the cases.

4.2.3. Holdups calculation

Based on the results for attenuation coefficients calculate gas, solid and liquid holdups. The procedure is given in Section 4.4.

4.2.4. Averaging and plotting

If needed, plot contour and averaged data holdup profiles (Section 4.5).

4.3. Reconstruction – obtaining attenuation coefficients

The reconstruction of the attenuation coefficients image from the raw scanned data is obtained in a stepwise process. It involves:

1. Averaging the raw data (Section 4.3.1)
2. Calculating the transmission ratios (Section 4.3.2)

3. Geometry input data - Calculating the length of the chords for each projection (Section 4.3.3)
4. Assigning initial guess (Section 4.3.4)
5. Reconstruction (Section 4.3.5)
6. Calculating the phase holdups (Section 4.4)
7. Averaging and plotting data (Section 4.5)

In each step, a corresponding FORTRAN code is used.

4.3.1. Projection sample average

The first step is to obtain sample (Section 3.1.5) average for each projection. The FORTRAN program *avgg.f* is used.

Summary of user inputs:

- nsam = number of samples (default 114)
- nd = number of detectors (default 9)
- nv = number of views (default 100)
- np = number of projections (default 25)
- specify name of raw data file – this is input file
- specify name of averaged file – this is output file

Note that in our case default values of all parameters are used and hence there is no need to modify the code. Still, input values can be easily changed as follows.

How to change the input parameters:

User changes these parameters in the code itself. For example, to change the number of detectors from the default value (9) to 7, open the *avgg.f* file and change the line:

parameter(nsam=114,**nd=9**,nv=100,np=25)

into:

parameter(nsam=114,**nd=7**,nv=100,np=25)

To change the name of your input data file, change the line:

open(unit=15, file='**air.asc**',status='old')

into:

open(unit=15, file='**your_in_file.asc**',status='old')

where: *your_in_file.asc* is the name of your raw data file.

To change the name of your output file, change the line:

open(unit=26, file='**air.dat**', status='unknown')

into:

open(unit=26, file='**your_out_file**.dat', status='unknown')

where: *your_out_file.asc* is the name of your output data file.

4.3.2 Transmission Ratio

FORTRAN program *prj.f.* is used to calculate the transmission ratio for each of the projections (see Section 4.1.3 about the use of transmission ratio in the reconstruction process).

Summary of user inputs:

- nv = number of views (default 99)
- np = number of projections per view (default 25)

- nd = number of detectors (default 9)
- specify name of scan data file – this is input file
- specify name of air ONLY scan data file - this is input file
- specify name of *smoothed* output file (default *prjs_object.dat*) – this is output file
- specify name of *interpolated* output file (default *prji_object.dat*) – this is output file

It is unnecessary to use the non-default values of either nv, np or nd for imaging of high pressure TBR system. Still, if the non-default values are used they can be specified as per the procedure given in Section 4.3.1.

The output file (*prjs_object.dat*) consists of two columns (Roy, 2006): first one gives angular designation of the projections and the second one transmission ratio (see Section 4.1.3). Total number of rows corresponds to the total number of projections in the scan; e.g., for default scan parameter values (Section 3), total number of rows is 22500. As a part of the *prj.f,* a smoothing procedure using an IMSL subroutine is performed. The goal is to smooth the TR data to eliminate the effect of the source fluctuations (Kumar, 1994, Roy, 2006). The degree of smoothing can be varied by setting the parameter *dis* in the program; however, the value of 0.15 recommended in Kumar, 1994 was found appropriate for the high pressure TBR imaging.

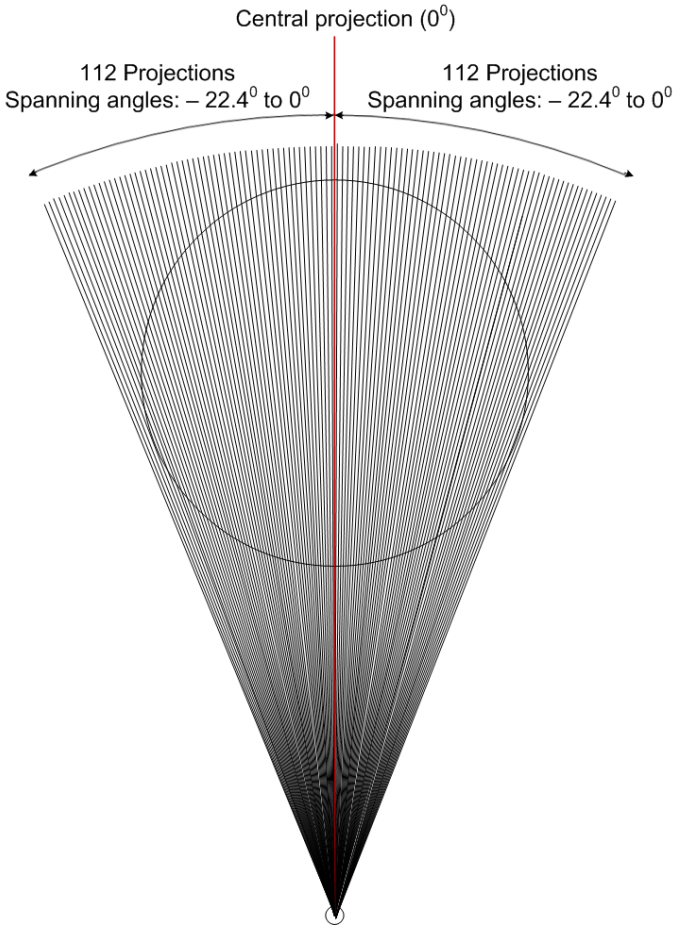

Figure C.6: Designation of projections via their angular position (view#1). Projections are spaced by 0.2^0. Drawn to scale for the imaging of high pressure TBR with the use of 9 detectors.

4.3.3 Projection geometry data

In Section 4.1.2 and Figure C.5-b, it was indicated that P_i, J_j and l_{ij} (set of pixels contributing to projection *i*, set of projections crossing pixel *j*, and length of projection *i* in pixel *j*, respectively) are needed to initiate EM iteration process. These sets are calculated using the *fanmat.f* code.

Summary of user inputs:

- M: The number of views (default 99).
- N: The number of pixels in the NxN reconstruction image (even number, default value N=80). Note that in case of high pressure TBR (DCOL = 16.3 cm, N=80) resulting pixel size is 2x2 mm, which is exactly the resolution limit or the detector collimator width (see Kumar, 1994, and Roy, 2006).
- ND: The number of detectors (default 9)
- NP: number of projections per view for one detector (default 25)
- NB: The number of projections in one view (ND x NP, default 225)
- DCOL: The diameter of the test section (the diameter of the column, default 16.3 cm)
- R: The distance between the source and the center of the test section (45.8 cm)
- FANANG: See Figure C.7, for default value of DCOL=16.3, FANANG $=20.50^0$)

It is recommended to use the above default values when imaging HP TBR. If non-default values of matrix size for the HP TBR system are to be used then new value has to be an even number that satisfies $N \le 80$. Further, suppose the column diameter is 4 *inch*, i.e., 10.16 *cm*. The following changes need to be introduced: (i) value for DCOL should be changed to 10.16; (ii) value for FANANG should be changed to $FANANG = 2 * \arcsin\left(\frac{DCOL/2[cm]}{45.8[cm]}\right) = 12.74^0$, (iii) $N \le \frac{DCOL[cm]}{0.2[cm]} \approx 50$.

The projection geometry output file is by default named *fanmat.dat.*

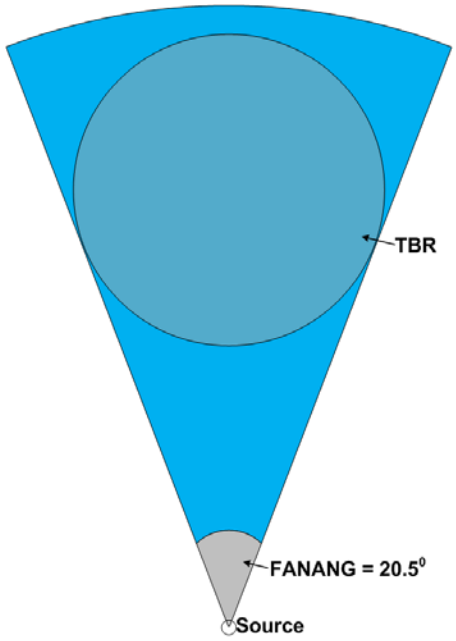

Figure C.7. FANANG parameter of the *fanmat.f* program. Adapted from Roy, 2006 and drawn to scale for the HP TBR.

4.3.4 Assigning Initial Guess Values

As discussed (Figure C.5-b), iterative EM algorithm requires the initial guess for the values of attenuation coefficients (μ, cm^{-1}). Recommended values are as follows:

$$\mu = 0.086\,\mathrm{cm}^{-1}, 0 \le r \le \frac{DCOL}{2}$$

$$\mu = 0, r > \frac{DCOL}{2}.$$

Initial guess is assigned using the FORTRAN code *amu.f*.

Summary of user inputs:

- npix = reconstruction matrix dimension (default 80)
- dcol = colum diameter in [cm] (default 16.3)
- output file name (default *amu80.dat*)

User changes these parameters in the code itself.

4.3.5 Reconstruction

The reconstruction (obtaining attenuation coefficients values on the domain) is performed using the FORTRAN code *emf.f*. The values returned are for the linear attenuation coefficient with units [1/cm].

Summary of user inputs:

- M: number of views (default 99)
- N: dimension of the reconstruction matrix (default 80)
- ND: number of detectors (default 9)
- NB: The number of projections in one view (default 225)
- IMAX: maximum number of iterations (default 500)
- Name of the file with projection ratios (default *prji_object.dat*), Section 4.3.2
- Name of the file with geometrical information (default *fanmat.dat*), Section 4.3.3
- Name of the file with guess values (default *amu80.dat*), Section 4.3.4

User changes these parameters in the code itself. These parameters need to be modified according to the actual scan performed.

The output file is (by default) *em.out* and contains a matrix of the numbers corresponding to the linear attenuation coefficient (units 1/cm) in each pixel.

4.4 Phase Holdups

As outlined in Section 4.2.1, to enable the calculation of phase holdups in a TBR, a number of reference scans has to be performed (see Chen et al., 2001, Roy, 2006):

1) Column containing only liquid phase. Employing Beer-Lambert's law we obtain the attenuation within the pixel *ij* as:

$$A_{L,ij} = \ln\left(\frac{I_{o,ij}}{I_{i,ij}}\right) = \rho_L \mu_L l_{ij} \tag{8}$$

Note that in this Section we will use *mass attenuation coefficient* (μ, cm^2/g).

2) Column containing only packing. In this case, the attenuation is:

$$A_{GS,ij} = \left\lfloor \rho_G \mu_G \left(1 - \varepsilon_{S,ij}\right) + \rho_s \mu_s \varepsilon_{s,ij} \right\rfloor l_{ij} \tag{9}$$

3) Column containing packed bed with liquid phase.

$$A_{LS,i_j} = \left\lfloor \rho_L \mu_L \left(1 - \varepsilon_{S,ij}\right) + \rho_S \mu_S \, \varepsilon_{S,ij} \right\rfloor l_{ij} \tag{10}$$

Equations (8) – (10) yield the following expressions for the phase holdups:

$$\varepsilon_{S,ij} = 1 - \frac{\left(A_{LS,ij} - A_{GS,ij}\right)}{A_{L,ij}} \tag{11}$$

$$\varepsilon_{G,ij} = \frac{\left(A_{LS,ij} - A_{GLS,ij}\right)}{A_{L,ij}} \tag{12}$$

$$\varepsilon_{L,ij} = 1 - \varepsilon_{G,ij} - \varepsilon_{S,ij} \tag{13}$$

Note that all the values in equations (11)-(13) are know as the output of the *em.f* code. The above equations to calculate the solid, gas and liquid holdup distribution have been implemented in the code *holdups.f.*

Summary of user inputs:

- npix = reconstruction matrix dimension (default 80)
- file with attenuation distribution values for gas-liquid-solid system, i.e., actual two phase flow (default *em_gls.out*)
- file with attenuation distribution values for liquid in column only (default *em_l.out*)
- file with attenuation distribution values for gas-solid system (default *em_gs.out*)
- file with attenuation distribution values for liquid-solid system (default *em_ls.out*)

The output, cross-sectional solid, gas and liquid holdup profiles, are stored in the output files *solid_holdup.out*, *gas_holdup.out* and *liquid_holdup.out* respectively. Once again, care should be taken in modifying the format of the output files according to the number of pixels being used.

References

Al-Dahhan, M. H. and Dudukovic, M. P. (1995). "Catalyst wetting efficiency in trickle-bed reactors at high pressure." Chemical Engineering Science 50(15): 2377-89.

Al-Dahhan, M. H. and Dudukovic, M. P. (1994). "Pressure drop and liquid holdup in high pressure trickle-bed reactors." Chemical Engineering Science 49(24B): 5681-98.

Al-Dahhan, M. H., Khadilkar, M. R., Wu, Y. and Dudukovic, M. P. (1998). "Prediction of Pressure Drop and Liquid Holdup in High-Pressure Trickle-Bed Reactors." Industrial & Engineering Chemistry Research 37(3): 793-798.

Al-Dahhan, M. H., Larachi, F., Dudukovic, M. P. and Laurent, A. (1997). "High-Pressure Trickle-Bed Reactors: A Review." Industrial & Engineering Chemistry Research 36(8): 3292-3314.

Al-Dahhan, M. H., Wu, Y. and Dudukovic, M. P. (1995). "Reproducible technique for packing laboratory-scale trickle-bed reactors with a mixture of catalyst and fines." Industrial & Engineering Chemistry Research 34(3): 741-747.

Alicilar, A., Bicer, A. and Murathan, A. (1994). "Relation between wetting efficiency and liquid holdup in packed columns." Chemical Engineering Communications 128: 95-107.

Alopaeus, V., Hynynen, K., Aittamaa, J. and Manninen, M. (2006). "Modeling of Gas-Liquid Packed-Bed Reactors with Momentum Equations and Local Interaction Closures." Industrial & Engineering Chemistry Research 45(24): 8189-8198.

Anadon, L. D., Lim, M. H. M., Sederman, A. J. and Gladden, L. F. (2005). "Hydrodynamics in two-phase flow within porous media." Magnetic resonance imaging 23(2): 291-294.

Anderson, T. B. and Jackson, R. (1967). "Fluid mechanical description of fluidized beds. Equations of motion." Industrial & Engineering Chemistry Fundamentals 6(4): 527-39.

Atta, A., Roy, S. and Nigam, K. D. P. (2007a). "Investigation of liquid maldistribution in trickle-bed reactors using porous media concept in CFD." Chemical Engineering Science 62(24): 7033-7044.

Atta, A., Roy, S. and Nigam, K. D. P. (2007b). "Prediction of pressure drop and liquid holdup in trickle bed reactor using relative permeability concept in CFD." Chemical Engineering Science 62(21): 5870-5879.

Attou, A., Boyer, C. and Ferschneider, G. (1999). "Modeling of the hydrodynamics of the cocurrent gas-liquid trickle flow through a trickle-bed reactor." Chemical Engineering Science 54(6): 785-802.

Attou, A. and Ferschneider, G. (1999). "A two-fluid model for flow regime transition in gas-liquid trickle-bed reactors." Chemical Engineering Science 54(21): 5031-5037.

Augier, F., Koudil, A., Royon-Lebeaud, A. and Muszynski, Y. (2008). "Numerical prediction of wetting and catalyst efficiencies inside trickle bed reactor." ISCRE 20, Kyoto, Japan.

Aydin, B. and Larachi, F. (2008). "Trickle bed hydrodynamics for (non-)Newtonian foaming liquids in non-ambient conditions." Chemical Engineering Journal 143(1-3): 236-243.

Babu, B. V., Shah, K. J. and Govardhana Rao, V. (2007). "Lateral mixing in trickle bed reactors." Chemical Engineering Science 62(24): 7053-7059.

Baldwin, C. A., Sederman, A. J., Mantle, M. D., Alexander, P. and Gladden, L. F. (1996). "Determination and characterization of the structure of a pore space from 3D volume images." Journal of Colloid and Interface Science 181(1): 79-92.

Barigou, M. (2004). "Particle tracking in opaque mixing systems: An overview of the capabilities of PET and PEPT." Chemical Engineering Research and Design 82(9 SPEC ISS): 1258-1267.

Barrett, H. H. (1990). "Objective assessment of image quality: effects of quantum noise and object variability." J. Opt. Soc. Am. A 7(7): 1266-1278.

Basavaraj, M. G., Gupta, G. S., Naveen, K., Rudolph, V. and Bali, R. (2005). "Local liquid holdups and hysteresis in a 2-D packed bed using X-ray radiography." AIChE Journal 51(8): 2178-2189.

Baussaron, L., Julcour-Lebigue, C., Wilhelm, A.-M., Delmas, H. and Boyer, C. (2007). "Wetting topology in trickle bed reactors." AIChE Journal 53(7): 1850-1860.

Bear, J. (1972). "Dynamics of fluids in porous media." Dover, New York.

Beaudry, E. G., Dudukovic, M. P. and Mills, P. L. (1987). "Trickle-Bed Reactors - Liquid Diffusional Effects in a Gas-Limited Reaction." AIChe Journal 33(9): 1435-1447.

Bell, B. (2005). "Simulation of liquid flow distribution in trickle-bed reactors." AIChE Annual Meeting, Cincinnati, OH, United States.

Benac, J. (2005). "Alternating minimization algorithms for X-ray computed tomography: multigrid acceleration and dual energy application." D.Sc. Thesis, Washington University- St.Louis.

Benenati, R. F. and Brosilow, C. B. (1962). "Void fraction distribution in beds of spheres." AIChE Journal 8: 359-61.

Benneet, M. A., West, R. M., Luke, S. P., Jia, X. and Williams, R. A. (1999). "Measurement and analysis of flows in a gas liquid column reactor." Chemical Engineering Science 54: 5003-5012.

Bertram, M., Wiegert, J., Schafer, D., Aach, T. and Rose, G. (2009). "Directional View Interpolation for Compensation of Sparse Angular Sampling in Cone-Beam CT." Medical Imaging, IEEE Transactions on 28(7): 1011-1022.

Bhusarapu, S., Al-Dahhan, M. H. and Dudukovic, M. P. (2006). "Solids flow mapping in a gas-solid riser: Mean holdup and velocity fields." Powder Technology 163(1-2): 98-123.

Bird, R. B., Stewart, W. E. and Lightfoot, E. N. (2001). "Transport Phenomena (2nd edition)." John Wiley & sons, New York

Boyer, C., Duquenne, A.-M. and Wild, G. (2002). "Measuring techniques in gas-liquid and gas-liquid-solid reactors." Chemical Engineering Science 57(16): 3185-3215.

Boyer, C. and Fanget, B. (2002). "Measurement of liquid flow distribution in trickle bed reactor of large diameter with a new gamma-ray tomographic system." Chemical Engineering Science 57(7): 1079-1089.

Boyer, C., Koudil, A., Chen, P. and Dudukovic, M. P. (2005). "Study of liquid spreading from a point source in a trickle bed via gamma-ray tomography and CFD simulation." Chemical Engineering Science 60(22): 6279-6288.

Boyer, C., Volpi, C. and Ferschneider, G. (2007). "Hydrodynamics of trickle bed reactors at high pressure: Two-phase flow model for pressure drop and liquid holdup, formulation and experimental validation." Chemical Engineering Science 62(24): 7026-7032.

BP (2004). Frontiers - BP (Beyond Petroleum) magazine of technology and innovation.

Carbonell, R. G. (2000). "Multiphase flow models in packed beds." Oil and Gas Science and Technology 55(4): 417-425.

Cartolano, A. R. (2002). AIChE Annual Meeting, Indianapolis, 4-8 November.

Chaouki, J., Larachi, F. and Dudukovic, M. P. (1997a). "Non-Invasive Monitoring of Multiphase Flows." Elsevier.

Chaouki, J., Larachi, F. and Dudukovic, M. P. (1997b). "Noninvasive Tomographic and Velocimetric Monitoring of Multiphase Flows." Industrial & Engineering Chemistry Research 36(11): 4476-4503.

Charpentier, J. C. and Favier, M. (1975). "Liquid holdup experimental data in trickle-bed reactors for foaming and nonfoaming hydrocarbons." AIChE Journal 21(6): 1213-18.

Charpentier, J. C., Prost, C. and Le Goff, P. (1968). "Trickling flow of liquid in a packed column." Chimie & Industrie, Genie Chimique 100(5): 653-655.

Chen, J., Gupta, P., Degaleesan, S., Al-Dahhan, M. H., Dudukovic, M. P. and Toseland, B. A. (1998). "Gas holdup distributions in large-diameter bubble columns measured by computed tomography." Flow Measurement and Instrumentation 9(2): 91-101.

Chen, J., Kemoun, A., Al-Dahhan, M. H., Dudukovic, M. P., Lee, D. J. and Fan, L.-S. (1999). "Comparative hydrodynamics study in a bubble column using computer-automated radioactive particle tracking (CARPT)/computed tomography (CT) and particle image velocimetry (PIV)." Chemical Engineering Science 54(13-14): 2199-2207.

Chen, J., Rados, N., Al-Dahhan, M. H., Dudukovic, M. P., Nguyen, D. and Parimi, K. (2001). "Particle motion in packed/ebullated beds by CT and CARPT." AIChE Journal 47(5): 994-1004.

Chen, Q., Kinzelbach, W. and Oswald, S. (2002). "Nuclear magnetic resonance imaging for studies of flow and transport in porous media." Journal of Environmental Quality 31(2): 477-486.

Chou, T. S., Worley, F. L., Jr. and Luss, D. (1977). "Transition to pulsed flow in mixed-phase cocurrent downflow through a fixed bed." Industrial & Engineering Chemistry, Process Design and Development 16(3): 424-427.

Choudhary, M., Propster, M. and Szekely, J. (1976). "On the importance of the inertial terms in the modeling of flow maldistribution in packed beds." AIChE J. 22(3): 600-603.

Christensen, G., McGovern, S. J. and Sundaresan, S. (1986). "Cocurrent downflow of air and water in a two-dimensional packed column." AIChE Journal 32(10): 1677-89.

ConocoPhillips (2008). Spirit-ConocoPhillips company magazine First Quarter.

Constantino, E. P. A. and Ozanyan, K. B. (2008). "Sinogram recovery for sparse angle tomography using a sinusoidal Hough transform." Measurement Science & Technology 19(9).

Crine, M. and Marchot, P. (1984). "Cocurrent downward gas-liquid flow in packed beds. Part 2. Stochastic model of liquid flow." International Chemical Engineering 24(1): 53-59.

Crine, M., Marchot, P. and L'Homme, G. (1980). "Liquid flow maldistributions in trickle-bed reactors." Chemical Engineering Communications 7(6): 377-388.

Crine, M., Marchot, P. and L'Homme, G. (1979). "Mathematical modeling of the liquid trickling flow through a packed bed using the percolation theory." Journal of Microwave Power 2: 994-1009.

Crine, M., Marchot, P. and L'Homme, G. (1992). "Statistical hydrodynamics in trickle flow columns." AIChE Journal 38(1): 136-47.

Csiszar, I. (1991). "Why least squares and maximum entropy? An axiomatic approach to inference for linear inverse problems." Ann. Stat. 19: 2033-66.

Darcy, H. (1856). "Les fontainer publiques de la ville de Dijon." Dalmont, Paris.

Darwood, M., W., Davies, M., D., G., P., J., K., J. and Stitt, E. H. (2003). "Development and Implemenation of Gamma-ray Tomography for Field Applications." 3rd World Congress on Industrial Process Tomography, Banff, Canada.

Dempster, A. P., Laird, N. M. and Rubin, D. B. (1977). "Maximum Likelihood from Incomplete Data via EM Algorithm." J. Roy Stat Soc, B 39: 1.

Drew, D. A. (1983). "Mathematical modeling of two-phase flow." Annual Review of Fluid Mechanics 15: 261-291.

Dudukovic, M. P. (2000). "Opaque multiphase reactors: experimentation, modeling and troubleshooting." Oil & Gas Science and Technology 55(2): 135-158.

Dudukovic, M. P., Larachi, F. and Mills, P. L. (2002). "Multiphase catalytic reactors: a perspective on current knowledge and future trends." Catalysis Reviews - Science and Engineering 44(1): 123-246.

Dudukovic, M. P., Larachi, F. and Mills, P. L. (1999). "Multiphase reactors - revisited." Chemical Engineering Science 54(13-14): 1975-1995.

Dullien, F. A. L. (1998). "Capillary effects and multiphase flow in porous media." Journal of Porous Media 1(1): 1-29.

Dullien, F. A. L. (1992). "Porous media: fluid transport and pore structure." Academic Press, San Diego.

El-Hisnawi, A. A., Dudukovic, M. P. and Mills, P. L. (1982). Trickle bed reactors: Dynamic tracer tests, reaction studies and modeling of reactor performance, Boston, Mass, USA, ACS, Washington, DC, USA.

Elkins, C. J. and Alley, M. T. (2007). "Magnetic resonance velocimetry: Applications of magnetic resonance imaging in the measurement of fluid motion." Experiments in Fluids 43(6): 823-858.

Ellman, M. J., Midoux, N., Laurent, A. and Charpentier, J. C. (1988). "A new, improved pressure drop correlation for trickle-bed reactors." Chemical Engineering Science 43(8): 2201-6.

Ellman, M. J., Midoux, N., Wild, G., Laurent, A. and Charpentier, J. C. (1990). "A new, improved liquid hold-up correlation for trickle-bed reactors." Chemical Engineering Science 45(7): 1677-84.

Ergun, S. (1952). "Fluid flow through packed columns." Chem. Eng. Progress 48: 89-94.

Ewing, R. E. (1991). "Simulation of multiphase flows in porous media." Transport in Porous Media 6(5-6): 479-499.

Forchheimer, P. (1914). Hydraulik, p. 116, Berlin.

Fourar, M., Lenormand, R. and Larachi, F. (2001). "Extending the F-function concept to two-phase flow in trickle beds." Chemical Engineering Science 56(21-22): 5987-5994.

Fox, R. O. (1987). "On the liquid flow distribution in trickle-bed reactors." Industrial & Engineering Chemistry Research 26(12): 2413-19.

Fukushima, S. and Kusaka, K. (1977). "Interfacial area and boundary of hydrodynamic flow region in packed column with cocurrent downward flow." Journal of Chemical Engineering of Japan 10(6): 461-7.

Gianetto, A. and Silveston, P. L. (1986). "Multiphase Chemical Reactors: Theory, Design, Scale-up." Hemisphere Publishing Co, New York, NY.

Gianetto, A. and Specchia, V. (1992). "Trickle-bed reactors: state of art and perspectives." Chemical Engineering Science 47(13-14): 3197-213.

Gierman, H. (1988). "Design of laboratory hydrotreating reactors: Scaling Down of Trickle-flow Reactors." Applied Catalysis 43(2): 277-286.

Gladden, L. F. (2006). "Magnetic resonance imaging of particulate and multiphase flows." Abstracts of Papers, 231st ACS National Meeting, Atlanta, GA, United States, March 26-30, 2006: IEC-236.

Gladden, L. F. and Alexander, P. (1996). "Applications of nuclear magnetic resonance imaging in process engineering." Measurement Science & Technology 7(3): 423-435.

Godfroy, L., Larachi, F., Kennedy, G., Grandjean, B. and Chaouki, J. (1997). "Online flow visualization in multiphase reactors using neural networks." Applied Radiation and Isotopes 48(2): 225-235.

Gotz, J., Zick, K., Heinen, C. and Konig, T. (2002). "Visualisation of flow processes in packed beds with NMR imaging: Determination of the local porosity, velocity vector and local dispersion coefficients." Chemical Engineering and Processing 41(7): 611-629.

Grosser, K., Carbonell, R. G. and Sundaresan, S. (1988). "Onset of pulsing in two-phase cocurrent downflow through a packed bed." AIChE Journal 34(11): 1850-1860.

Gunjal, P. R., Kashid, M. N., Ranade, V. V. and Chaudhari, R. V. (2005a). "Hydrodynamics of Trickle-Bed Reactors: Experiments and CFD Modeling." Industrial & Engineering Chemistry Research 44(16): 6278-6294.

Gunjal, P. R. and Ranade, V. V. (2007). "Modeling of laboratory and commercial scale hydro-processing reactors using CFD." Chemical Engineering Science 62(18-20 SPEC ISS): 5512-5526.

Gunjal, P. R., Ranade, V. V. and Chaudhari, R. V. (2005b). "Computational study of a single-phase flow in packed beds of spheres." AIChE Journal 51(2): 365-378.

Gupta, R. D. and Kundu, D. (2006). "On the comparison of Fisher information of the Weibull and GE distributions." Journal of Statistical Planning and Inference 136(9): 3130-3144.

Hanika, J. (1999). "Safe operation and control of trickle-bed reactor." Chemical Engineering Science 54(20): 4653-4659.

Harter, I., Boyer, C., Raynal, L., Ferschneider, G. and Gauthier, T. (2001). "Flow Distribution Studies Applied to Deep Hydro-Desulfurization." Industrial & Engineering Chemistry Research 40(23): 5262-5267.

Hassanizadeh, S. M. and Gray, W. G. (1993). "Thermodynamic basis of capillary pressure in porous media." Water Resources Research 29(10): 3389.

Hero, A. O., Usman, M., Sauve, A. C. and Fessler, J. A. (1997). "Recursive algorithms for computing the Cramer-Rao bound." Signal Processing, IEEE Transactions on 45(3): 803-807.

Herskowitz, M. and Smith, J. M. (1978). "Liquid distribution in trickle-bed reactors. Part I. Flow measurements." AIChE Journal 24(3): 439-50.

Herskowitz, M. and Smith, J. M. (1983). "Trickle bed reactors: A review." AIChE Journal 29(1): 1-18.

Highfill, W. and Al-Dahhan, M. (2001). "Liquid-solid mass transfer coefficient in high pressure trickle bed reactors." Chemical Engineering Research and Design 79(A6): 631-640.

Hoek, P. J., Wesselingh, J. A. and Zuiderweg, F. J. (1986). "Small scale and large scale liquid maldistiribution in packed columns." Chemical Engineering Research & Design 64(6): 431-449.

Holub, R. A., Dudukovic, M. P. and Ramachandran, P. A. (1992a). "A phenomenol. model for pressure drop, liquid holdup, and flow regime transition in gas-liquid trickle flow." Chemical Engineering Science 47(9-11): 2343-8.

Holub, R. A., Dudukovic, M. P. and Ramachandran, P. A. (1992b). "Pressure drop, liquid holdup, and flow regime transition in trickle flow." AIChE Journal 39(2): 302-21.

Iliuta, I., Aydin, B. and Larachi, F. (2005). "Onset of pulsing in trickle beds with non-Newtonian liquids at elevated temperature and pressure -- Modeling and experimental verification." Chemical Engineering Science 61(2): 526-537.

Iliuta, I., Grandjean, B. P. A. and Larachi, F. (2002). "New mechanistic film model for pressure drop and liquid holdup in trickle flow reactors." Chemical Engineering Science 57(16): 3359-3371.

Iliuta, I. and Larachi, F. (2005). "Modelling the hydrodynamics of gas-liquid packed beds via slit models: A review." International Journal of Chemical Reactor Engineering 3.

Iliuta, I. and Larachi, F. (2003). "Two-phase flow in porous media under spatially uniform magnetic-field gradients: Novel way to process intensification." Canadian Journal of Chemical Engineering 81(3-4): 776-783.

Iliuta, I., Ortiz-Arroyo, A., Larachi, F., Grandjean, B. P. A. and Wild, G. (1999). "Hydrodynamics and mass transfer in trickle-bed reactors: an overview." Chemical Engineering Science 54(21): 5329-5337.

Ishii, M. (1975). "Thermo-fluid dynamic theory of two phase flow." Eyrolles, Paris.

Ismail, I., Gamio, J. C., Bukhari, S. F. A. and Yang, W. Q. (2005). "Tomography for multi-phase flow measurement in the oil industry." Flow Measurement and Instrumentation 16(2-3): 145-155.

Jaffe, S. B. (1976). "Hot spot simulation in commercial hydrogenation processes." Industrial & Engineering Chemistry, Process Design and Development 15(3): 410-416.

Jiang, Y., Al-Dahhan, M. H. and Dudukovic, M. P. (2001). "Statistical characterization of macroscale multiphase flow textures in trickle beds." Chemical Engineering Science 56(4): 1647-1656.

Jiang, Y., Khadilkar, M. R., Al-Dahhan, M. H. and Dudukovic, M. P. (2002a). "CFD of multiphase flow in packed-bed reactors: I. k-fluid modeling issues." AIChE Journal 48(4): 701-715.

Jiang, Y., Khadilkar, M. R., Al-Dahhan, M. H. and Dudukovic, M. P. (2002b). "CFD of multiphase flow in packed-bed reactors: II. Results and applications." AIChE Journal 48(4): 716-730.

Jiang, Y., Khadilkar, M. R., Al-Dahhan, M. H. and Dudukovic, M. P. (2000). "Single phase flow modeling in packed beds: discrete cell approach revisited." Chemical Engineering Science 55(10): 1829-1844.

Kan, K.-M. and Greenfield, P. F. (1978). "Multiple hydrodynamic states in cocurrent two-phase downflow through packed beds." Industrial & Engineering Chemistry Process Design and Development 17(4): 482-5.

Kennedy, C. R. and Jaffe, S. B. (1986). "Analysis of tracer experiments from commercial scale trickle bed reactors." Chemical Engineering Science 41(4): 845-853.

Khadilkar, M. R., Al-Dahhan, M. H. and Dudukovic, M. P. (2005). "Multicomponent Flow-Transport-Reaction Modeling of Trickle Bed Reactors: Application to Unsteady State Liquid Flow Modulation." Industrial & Engineering Chemistry Research 44(16): 6354-6370.

Khopkar, A. R., Rammohan, A. R., Ranade, V. V. and Dudukovic, M. P. (2005). "Gas-liquid flow generated by a Rushton turbine in stirred vessel: CARPT/CT measurements and CFD simulations." Chemical Engineering Science 60(8-9): 2215-2229.

Kozeny, J. (1927). S.-Ber. Wiener Akad., Abt. IIa 136: 271.

Kramer, G. J. (1998). "Static liquid hold-up and capillary rise in packed beds." Chemical Engineering Science 53(16): 2985-2992.

Kuipers, J. A. M. and Van Swaaij, W. P. M. (1997). "Application of Computational Fluid Dynamics to Chemical Reaction Engineering." Reviews in Chemical Engineering 13(3): 1-118.

Kumar, S. B. (1994). "Computer Tomographic Measurement of Void Fraction and Modeling of the Flow in Bubble Columns." Ph.D. Thesis, Florida Atlantic University, Boca Raton, FL.

Kumar, S. B. and Dudukovic, M. P. (1997). "Computer assisted gamma and X-ray tomography: applications to multiphase flow systems." Non-Invasive Monitoring of Multiphase Flows: 47-103.

Kumar, S. B., Dudukovic, M. P. and Toseland, B. A. (1997a). "Measurement techniques for local and global fluid dynamic quantities in two and three phase systems." Non-Invasive Monitoring of Multiphase Flows: 1-45.

Kumar, S. B., Moslemian, D. and Dudukovic, M. P. (1997b). "Gas-holdup measurements in bubble columns using computed tomography." AIChE Journal 43(6): 1414-1425.

Kundu, A., Narasimhan, C. S. L., Verma, R. P. and Nigam, K. D. P. (2002). "Modeling hydrodynamics of trickle-bed reactors at high pressure." AIChE Journal 48(11): 2459-2474.

Kundu, A., Nigam, K. D. P., Duquenne, A. M. and Delmas, H. (2003a). "Recent developments on hydroprocessing reactors." Reviews in Chemical Engineering 19(6): 531-605.

Kundu, A., Nigam, K. D. P. and Verma, R. P. (2003b). "Catalyst wetting characteristics in trickle-bed reactors." AIChE Journal 49(9): 2253-2263.

Kundu, A., Saroha, A. K. and Nigam, K. D. P. (2001). "Liquid distribution studies in trickle-bed reactors." Chemical Engineering Science 56(21-22): 5963-5967.

Kuzeljevic, Z. V., Merwe, W. v. d., Al-Dahhan, M. H., Dudukovic, M. P. and Nicol, W. (2008). "Effect of Operating Pressure on the Extent of Hysteresis in a Trickle Bed Reactor." Ind. Eng. Chem. Res. 47(20): 7593-7599.

Lage, J. L. (1998). "The fundamental theory flow through permeable media from Darcy to turbulence." Transport phenomena in porous media, D. B. Ingham and I. Pop, eds., Pergamon, New York.

Lakota, A., Levec, J. and Carbonell, R. G. (2002). "Hydrodynamics of trickling flow in packed beds: relative permeability concept." AIChE Journal 48(4): 731-738.

Lange, K. and Carson, R. (1984). "EM reconstruction algorithms for emission and transmission tomography." Journal of computer assisted tomography 8(2): 306-16.

Lange, R., Schubert, M. and Bauer, T. (2005). "Liquid holdup in trickle-bed reactors at very low liquid reynolds numbers." Industrial and Engineering Chemistry Research 44(16): 6504-6508.

Larachi, F. and Chaouki, J. (2000). "Non-invasive 3-D radioactive particle tracking in heterogeneous flows: principle & applications." Recents Progres en Genie des Procedes 14(75): 347-353.

Larachi, F., Grandjean, B., Iliuta, I., Bensetiti, Z., Andre, A., Wild, G. and Chen, M. (1999). "Excel Worksheet Simulatiors for Packed Beds." http://www.gch.ulaval.ca/bgrandjean/pbrsimul/pbrsimul.html.

Larachi, F. and Grandjean, B. P. A. (2003). "Special Issue on Application of Neural Networks to Multiphase Reactors. [In: Chem. Eng. Process., 2003; 42(8-9)]."

Larachi, F., Iliuta, I., Al-Dahhan, M. A. and Dudukovic, M. P. (2000). "Discriminating Trickle-Flow Hydrodynamic Models: Some Recommendations." Industrial & Engineering Chemistry Research 39(2): 554-556.

Larachi, F., Laurent, A., Midoux, N. and Wild, G. (1991). "Experimental study of a trickle-bed reactor operating at high pressure: two-phase pressure drop and liquid saturation." Chemical Engineering Science 46(5-6): 1233-46.

Larachi, F., Laurent, A., Wild, G. and Midoux, N. (1992). "Pressure effects on gas-liquid interfacial areas in cocurrent trickle-flow reactors." Chemical Engineering Science 47(9-11): 2325-30.

Lazzaroni, C. L., Keselman, H. R. and Figoli, N. S. (1989). "Trickle bed reactors: Multiplicity of hydrodynamic states. Relation between the pressure drop and the liquid holdup." Industrial & Engineering Chemistry Research 28(1): 119-121.

Lehmann, E. L. and Casella, G. (1998). "Theory of point estimation." Second Edition, Springer, New York.

Levec, J., Grosser, K. and Carbonell, R. G. (1988). "The hysteretic behavior of pressure drop and liquid holdup in trickle beds." AIChE Journal 34(6): 1027-30.

Levec, J., Saez, E. A. and Carbonell, R. G. (1985). "Holdup and pressure drop in trickle-bed reactors." Kemija u Industriji 34(1): 21-4.

Leverett, M. C. (1941). "Capillary Behavior in Porous Solid." Trans. AIME 142: 159.

Llamas, J.-D., Lesage, F. and Wild, G. (2008a). "Influence of Gas Flow Rate on Liquid Distribution in Trickle-Beds Using Perforated Plates as Liquid Distributors." Ind. Eng. Chem. Res.

Llamas, J.-D., Perat, C., Lesage, F., Weber, M., D'Ortona, U. and Wild, G. (2008b). "Wire mesh tomography applied to trickle beds: A new way to study liquid maldistribution." Chemical Engineering and Processing: Process Intensification 47(9-10): 1765-1770.

Lopes, R. J. G. and Quinta-Ferreira, R. M. (2008a). "Evaluation of multiphase CFD models in gas-liquid packed-bed reactors for pollution abatement: Euler-Euler versus volume of fluid." ISCRE 20, Kyoto, Japan.

Lopes, R. J. G. and Quinta-Ferreira, R. M. (2008b). "Three-dimensional numerical simulation of pressure drop and liquid holdup for high-pressure trickle-bed reactor." Chemical Engineering Journal 145(1): 112-120.

Lopes, R. J. G. and Quinta-Ferreira, R. M. (2007). "Trickle-bed CFD studies in the catalytic wet oxidation of phenolic acids." Chemical Engineering Science 62(24): 7045-7052.

Loudon, D., van der Merwe, W. and Nicol, W. (2006). "Multiple hydrodynamic states in trickle flow: Quantifying the extent of pressure drop, liquid holdup and gas-liquid mass transfer variation." Chemical Engineering Science 61(22): 7551-7562.

Lutran, P. G., Ng, K. M. and Delikat, E. P. (1991). "Liquid distribution in trickle beds. An experimental study using computer-assisted tomography." Industrial & Engineering Chemistry Research 30(6): 1270-1280.

Maiti, R., Khanna, R. and Nigam, K. D. P. (2006). "Hysteresis in Trickle-Bed Reactors: A Review." Industrial & Engineering Chemistry Research 45(15): 5185-5198.

Maiti, R., Khanna, R. and Nigam, K. D. P. (2005). "Trickle-Bed Reactors: Porosity-Induced Hysteresis." Industrial & Engineering Chemistry Research 44(16): 6406-6413.

Maiti, R. N. and Nigam, K. D. P. (2007). "Gas-Liquid Distributors for Trickle-Bed Reactors: A Review." Industrial & Engineering Chemistry Research 46(19): 6164-6182.

Maiti, R. N., Sen, P. K. and Nigam, K. D. P. (2004). "Trickle-bed reactors: liquid distribution and flow texture." Reviews in Chemical Engineering 20(1-2): 57-109.

Mann, R., Dickin, F. J., Wang, M., Dyakowski, T., Williams, R. A., Edwards, R. B., Forrest, A. E. and Forrest, P. J. (1997). "Application of electrical resistance tomography to interrogate mixing processes at plant scale." Chemical Engineering Science 52: 2087-2097.

Mantle, M. D., Sedermann, A. J. and Gladden, L. F. (2001). "Single-and two-phase flow in fixed-bed reactors: MRI flow visualisation and lattice-Boltzmann simulations." Chemical Engineering Science 56(2): 523-529.

Marcandelli, C., Lamine, A. S., Bernard, J. R. and Wild, G. (2000). "Liquid distribution in trickle-bed reactor." Oil & Gas Science and Technology 55(4): 407-415.

Marchot, P., Toye, D., Crine, M., Pelsser, A. M. and L'Homme, G. (1999). "Investigation of liquid maldistribution in packed columns by x-ray tomography." Chemical Engineering Research and Design 77(A6): 511-518.

McDonald, I. F., El-Sayed, M. S., Dullien, F. A. L. and Mow, K. (1979). "Flow through porous media - The Ergun equation revisited." Industrial & Engineering Chemistry, Fundamentals 18(3): 199-208.

McLachlan, G. J. and Krishnan, T. (2008). "The EM algorithm and Extensions." Second Edition, Wiley&Sons, Hoboken, NJ.

Melli, T. R., de Santos, J. M., Kolb, W. B. and Scriven, L. E. (1990). "Cocurrent downflow in networks of passages. Microscale roots of macroscale flow regimes." Industrial & Engineering Chemistry Research 29(12): 2367-2379.

Mills, P. L., Beaudry, E. G. and Dudukovic, M. P. (1984). "Comparison and prediction of reactor performance for packed beds with two phase flow: down flow, upflow and countercurrent flow." Institution of Chemical Engineers Symposium Series 87: 527.

Mills, P. L. and Dudukovic, M. P. (1979). "A Dual-Series Solution for the Effectiveness Factor of Partially Wetted Catalysts in Trickle-Bed Reactors." Ind. Eng. Chem. Fundam. 18(2): 139-149.

Mills, P. L., Erk, H. F., Evans, J. and Dudukovic, M. P. (1981). "Models for evaluation of catalyst effectiveness factors in trickle-bed reactors." Chemical Engineering Science 36(5): 947-50.

Mirzaei, M. and Das, D. B. (2007). "Dynamic effects in capillary pressure-saturations relationships for two-phase flow in 3D porous media: Implications of micro-heterogeneities." Chemical Engineering Science 62(7): 1927-1947.

Moller, L. B., Halken, C., Hansen, J. A. and Bartholdy, J. (1996). "Liquid and gas distribution in trickle-bed reactors." Industrial & Engineering Chemistry Research 35(3): 926-930.

Moslemian, D., Devanathan, N. and Dudukovic, M. P. (1992). "Radioactive particle tracking technique for investigation of phase recirculation and turbulence in multiphase systems." Review of Scientific Instruments 63(10, Pt. 1): 4361-72.

Mueller, G. E. (1991). "Prediction of radial porosity distributions in randomly packed fixed beds of uniformly sized spheres in cylindrical containers." Chemical Engineering Science 46(2): 706-8.

Murphy, S. and York, T. A. (2006). "Confidence in Tomographic Imaging." PROCTOM 2006, Warsaw, Poland, Sept 14-15 2006.

Muskat, M. and Meres, M. (1936). Physics 7: 346.

Nemec, D. and Levec, J. (2005). "Flow through packed bed reactors: 2. Two-phase concurrent downflow." Chemical Engineering Science 60(24): 6958-6970.

Nigam, K. D. P. and Larachi, F. (2005). "Process intensification in trickle-bed reactors." Chemical Engineering Science 60(22): 5880-5894.

O'Sullivan, J., M and Benac, J. (2007). "Alternating minimization algorithms for transmission tomography." IEEE Trans. Med. Imaging 26: 283-97.

Patel, A. K., Patwardhan, A. W. and Thorat, B. N. (2007). " Comparison of ML-EM algorithm and ART for reconstruction of gas hold-up profile in a bubble column." Chemical Engineering Journal 130(2-3): 135-145.

Propp, R. M., Colella, P., Crutchfield, W. Y. and Day, M. S. (2000). "A Numerical Model for Trickle Bed Reactors." Journal of Computational Physics 165(2): 311-333.

Radilla, G., Fourar, M. and Larachi, F. (2005). "Technical note correlating gas-liquid co-current flow hydrodynamics in packed beds using the F-function concept." Journal of Chemical Technology and Biotechnology 80(1): 107-112.

Ramachandran, P. A., Dudukovic, M. P. and Mills, P. L. (1987). "Recent advances in the analysis and design of trickle-bed reactors." Sadhana 10(1-2): 269-98.

Rao, V. G., Ananth, M. S. and Varma, Y. B. G. (1983). "Hydrodynamics of two-phase cocurrent downflow through packed beds. Part I. Macroscopic model." AIChE Journal 29(3): 467-73.

Ravindra, P. V., Rao, D. P. and Rao, M. S. (1997). "Liquid Flow Texture in Trickle-Bed Reactors: An Experimental Study." Industrial & Engineering Chemistry Research 36(12): 5133-5145.

Raynal, L. and Harter, I. (2001). "Studies of gas-liquid flow through reactors internals using VOF simulations." Chemical Engineering Science 56(21-22): 6385-6391.

Reinecke, N., Petritsch, G., Schmitz, D. and Mewes, D. (1998). "Tomographic measurement techniques. Visualization of multiphase flows." Chemical Engineering & Technology 21(1): 7-18.

Ring, Z. E. and Missen, R. W. (1991). "Trickle-bed reactors: tracer study of liquid holdup and wetting efficiency at high temperature and pressure." Canadian Journal of Chemical Engineering 69(4): 1016-20.

Roblee, L. H. S., Jr., Baird, R. M. and Tierney, J. W. (1958). "Radial porosity variations in packed beds." AIChE Journal 4: 460-4.

Roy, S. (2006). Phase distribution and performance studies of gas-liquid monolith reactor. D.Sc. Thesis, Washington University, Saint Louis**:** 203 pp.

Roy, S., Kemoun, A., Al-Dahhan, M. H., Dudukovic, M. P., Skourlis, T. B. and Dautzenberg, F. M. (2004). "Countercurrent flow distribution in structured packing via computed tomography." Chemical Engineering and Processing 44(1): 59-69.

Saez, A. E. and Carbonell, R. G. (1985). "Hydrodynamic parameters for gas-liquid cocurrent flow in packed beds." AIChE Journal 31(1): 52-62.

Saroha, A. K. and Nigam, K. D. P. (1996). "Trickle Bed Reactors." Reviews in Chemical Engineering 12: 207-347.

Saroha, A. K., Nigam, K. D. P., Saxena, A. K. and Dixit, L. (1998a). "RTD studies in trickle bed reactors packed with porous particles." Canadian Journal of Chemical Engineering 76(4): 738-742.

Saroha, A. K., Nigam, K. D. P., Saxena, A. K. and Kapoor, V. K. (1998b). "Liquid distribution in trickle-bed reactors." AIChE Journal 44(9): 2044-2052.

Scheidegger, A. E. (1957). "The physics of flow through porous media." The Macmillan company, New York.

Schubert, M., Hessel, G., Zippe, C., Lange, R. and Hampel, U. (2008). "Liquid flow texture analysis in trickle bed reactors using high-resolution gamma ray tomography." Chemical Engineering Journal 140(1-3): 332-340.

Shollenberger, K. A., Torczynski, J. R., R., A. D., O'Hern, T. J. and Jackson, N. B. (1997). "Gamma densitometry tomography of gas hold up spatial distribution in industrial scale bubble columns." Chemical Engineering Science 52: 2037.

Sicardi, S., Baldi, G., Specchia, V., Mazzarino, I. and Gianetto, A. (1981). "Packing wetting in trickle bed reactors: influence of the gas flow rate." Chemical Engineering Science 36(1): 226-8.

Sie, S. T. and Krishna, R. (1998). "Process development and scale up: III. Scale-up and scale-down of trickle bed processes." Reviews in Chemical Engineering 14(3): 203-252.

Snyder, D., L., Schulz, T., J. and O'Sullivan, J., M (1992). "Deblurring subject to nonnegativity constraints." IEEE Trans. Signal Processing 40: 1143-1150.

Souadnia, A. and Latifi, M. A. (2001). "Analysis of two-phase flow distribution in trickle-bed reactors." Chemical Engineering Science 56(21-22): 5977-5985.

Stanek, V. and Szekely, J. (1974). "Three dimensional flow of fluids through nonuniform packed beds." AIChE Journal 20(5): 974-980.

Stapf, S. and Han, S. (2005). "NMR imaging in chemical engineering." Willey-VCH Verlag GmbH&Co. KGaA, Weinheim.

Stephenson, J. L. and Stewart, W. E. (1986). "Optical measurements of porosity and fluid motion in packed beds." Chemical Engineering Science 41(8): 2161-70.

Stitt, E. H. and James, K. (2003). "Process Tomography and Particle Tracking: Research and Commercial Diagnostics Tool." 3rd World Congress on Industrial Process Tomography, Banff, Canada.

Sundaresan, S. (1994). "Liquid Distribution in Trickle Bed Reactors." Energy & Fuels 8(3): 531-5.

Sundaresan, S. (2000). "Modeling the hydrodynamics of multiphase flow reactors: current status and challenges." AIChE Journal 46(6): 1102-1105.

Sweeney, D. E. (1967). "A correlation for pressure drop in two phase concurrent flow in packed beds." AIChE J. 13: 663.

Talmor, E. (1977). "Two-phase downflow through catalyst beds." AIChE Journal 23(6): 868-78.

Tan, C. S. and Smith, J. M. (1982). "A dynamic method for liquid particle mass transfer in trickle beds." AIChE J. 28: 190.

Tayebi, D., Svendsen, H. F., Jakobsen, H. A. and Grislingas, A. (2001). "Measurement techniques and data interpretations for validating CFD multi phase reactor models." Chemical Engineering Communications 186: 57-159.

Tibirna, C., Edouard, D., Fortin, A. and Larachi, F. (2006). "Usability of ECT for quantitative and qualitative characterization of trickle-bed flow dynamics subject to filtration conditions." Chemical Engineering and Processing 45(7): 538-545.

Toye, D. and Marchot, P. (2005). "Imaging of liquid distribution in reactive distillation packings with a new high-energy x-ray tomograph." Measurement Science & Technology 16(11): 2213-2220.

Toye, D., Marchot, P., Crine, M. and L'Homme, G. (1999). "Modelling of the liquid distribution in a trickle flow packed column based upon X-ray tomography images." Chemical Engineering Communications 175: 131-142.

Trivizadakis, M. E., Giakoumakis, D. and Karabelas, A. J. (2006). "A study of particle shape and size effects on hydrodynamic parameters of trickle beds." Chemical Engineering Science 61(17): 5534-5543.

Tukac, V. and Hanika, J. (1992). "Influence of catalyst particles orientation on the pressure drop and the liquid dispersion in the trickle bed reactor." Chemical Engineering Science 47(9-11): 2227-32.

van der Merwe, W. and Nicol, W. (2005). "Characterization of Multiple Flow Morphologies within the Trickle Flow Regime." Industrial & Engineering Chemistry Research 44(25): 9446-9450.

van der Merwe, W., Nicol, W. and de Beer, F. (2007a). "Three-dimensional analysis of trickle flow hydrodynamics: Computed tomography image acquisition and processing." Chemical Engineering Science 62(24): 7233-7244.

van der Merwe, W., Nicol, W. and de Beer, F. (2007b). "Trickle flow distribution and stability by X-ray radiography." Chemical Engineering Journal (Amsterdam, Netherlands) 132(1-3): 47-59.

van Herk, D., Kreutzer, M. T., Makkee, M. and Moulijn, J. A. (2005). "Scaling down trickle bed reactors." Catalysis Today 106(1-4): 227-232.

van Houwelingen, A. J., Sandrock, C. and Nicol, W. (2006). "Particle wetting distribution in trickle-bed reactors." AIChE Journal 52(10): 3532-3542.

van Klinken, J. and van Dongen, R. H. (1980). "Catalyst dilution for improved performance of laboratory trickle flow reactors." Chemical Engineering Science 35(1/2): 59-66.

van Trees, H. L. (1968). "Detection, estimation and modulation theory." John Wiley & sons, New York.

Varma, R., Bhusarapu, S., O'Sullivan, J. A. and Al-Dahhan, M. H. (2008). "A comparison of alternating minimization and expectation maximization algorithms for single source gamma ray tomography." Measurement Science & Technology 19(1).

Wammes, W. J. A., Middelkamp, J., Huisman, W. J., DeBaas, C. M. and Westerterp, K. R. (1991). "Hydrodynamics in a cocurrent gas-liquid trickle bed at elevated pressures." AIChE Journal 37(12): 1849-62.

Wang, R., Mao, Z.-S. and Chen, J. (1995). "Experimental and theoretical studies of pressure drop hysteresis in trickle bed reactors." Chemical Engineering Science 50(14): 2321-8.

Wijffels, J. B., Verloop, J. and Zuiderweg, F. J. (1974). "Wetting of catalyst particles under trickle flow conditions." Advances in Chemistry Series(13): 151-163.

Wilke, C. R. and Chang, C. (1955). "Correlation of diffusion coefficients in dilute solutions." AIChE J. 1(2): 264-270.

Wu, Y., Khadilkar, M. R., Al-Dahhan, M. H. and Dudukovic, M. P. (1996). "Comparison of upflow and downflow two-phase flow packed-bed reactors with and without fines: experimental observations." Industrial & Engineering Chemistry Research 35(2): 397-405.

Yester, M. W. and Barnes, G. T. (1977). "Geometrical limitations of computed tomography scanner resolution." Appl. Opt. Instr. in Medicine 127: 296-303.

Young, T. (1805). "Cohesion of fluids." Philosophical Transactions: 65.

Zhukova, T. B., Pisarenko, V. N. and Kafarov, V. V. (1990). "Modeling and design of industrial reactors with a stationary bed of catalyst and two-phase gas-liquid flow. A review." International Chemical Engineering 30(1): 57-102.

Zimmerman, S. P., Chu, C. F. and Ng, K. M. (1987). "Axial and radial dispersion in trickle-bed reactors with trickling gas-liquid down-flow." Chemical Engineering Communications 50(1-6): 213-40.

Zimmerman, S. P. and Ng, K. M. (1986). "Liquid distribution in trickling flow trickle bed reactors." Chemical Engineering Science 41(4): 861-866.